



Heterostructure design and epitaxial growth of AlGaIn-based light emitting diodes emitting in the UVC wavelength range

vorgelegt von
Master of Science in Physik

Norman Susilo

an der Fakultät II - Mathematik und Naturwissenschaften der Technischen
Universität Berlin zur Erlangung des akademischen Grades

Doktor der Naturwissenschaften

- Dr. rer. nat. -

genehmigte Dissertation

Promotionsausschuss:

Vorsitzender	Prof. Dr. Matthias Bickermann
Gutachter	Prof. Dr. Michael Kneissl
Gutachter	Prof. Dr. Udo W. Pohl
Gutachter	Dr. Hans-Juergen Lugauer

Tag der wissenschaftlichen Aussprache: 04. August 2020

Berlin 2020

Heterostructure design and epitaxial growth of AlGaN-based light emitting diodes emitting in the UVC wavelength range

AlGaN-based ultraviolet-C (UVC) light emitting diodes (LEDs) can be applied to a wide range of applications. However, the efficiency of UVC-LEDs is still relatively modest, which provides the focus of this thesis: The development of efficient UVC-LEDs with emission wavelengths near 265 nm. This thesis presents a systematic study of the influence of the heterostructure design and the layer properties on the electro-optical performance of UVC-LEDs.

The AlGaN-based UVC-LEDs are grown by MOVPE on AlN/sapphire templates. In particular, the applicability of sputtered and high temperature annealed (HTA) low cost AlN/sapphire templates for the growth of the UVC-LED heterostructures is investigated. Similar crystal quality and optical emission power of the UVC-LEDs are demonstrated compared to UVC-LEDs on epitaxial lateral overgrowth (ELO) AlN/sapphire templates, offering the potential to reduce the chip costs. A further improvement in emission power is achieved by combining the HTA approach with the ELO process. The growth of pseudomorphically strained AlGaN heterostructures on the AlN buffer can cause the formation of dislocation loops and their presence reduces the emission power. Based on the results of this study, the density of these dislocation loops increases with the compressive strain and layer thickness. The dislocation loop generation is suppressed by implementing a two-step heterostructure approach for the n -side. Hereby a second AlGaN:Si contact layer with low Al mole fraction is used, which enables a significantly reduced operating voltage while maintaining the emission power. Furthermore, internal polarization fields can influence the device performance. A new approach is presented and examined using capacitance-voltage measurements for the accurate determination of the polarization field. Both the magnitude and the direction of the determined polarizations fields are in agreement with the values as predicted by the theory, which allows for more reliable device simulations. The light extraction efficiency is one of the key factors limiting the LED efficiency. The applicability of semi-transparent p -sides is explored. By combining transparent p -AlGaN layers with a thin GaN p -contact layer, LEDs with an increased light extraction efficiency could be realized. The work of this thesis leads to the realization of highly efficient UVC-LEDs with emission powers of 47 mW at 350 mA, peak external quantum efficiencies of 3.6% and peak wall-plug efficiencies of 2.7%.



Heterostruktur-Design und epitaktisches Wachstum von AlGa_N-basierten lichtemittierenden Dioden, die im UVC-Wellenlängenbereich emittieren

AlGa_N-basierte ultraviolett-C (UVC) Leuchtdioden (LEDs) können für ein breites Spektrum von Anwendungen eingesetzt werden. Allerdings ist die Effizienz von UVC-LEDs noch relativ gering, was den Schwerpunkt dieser Arbeit bildet: Die Entwicklung von effizienten UVC-LEDs mit Emissionswellenlängen nahe 265 nm. In dieser Arbeit wird eine systematische Untersuchung des Einflusses des Heterostrukturdesigns und der Schichteigenschaften auf die elektro-optische Leistung von UVC-LEDs vorgestellt.

Die AlGa_N-basierten UVC-LEDs werden mittels MOVPE auf AlN/Saphir-Basisschichten gewachsen. Insbesondere wird die Anwendbarkeit von gesputterten und hochtemperaturgetemperten (HTA) kostengünstigen AlN/Saphir-Basisschichten für das Wachstum der UVC-LED-Heterostrukturen untersucht. Es wird eine ähnliche Kristallqualität und optische Emissionsleistung im Vergleich zu UVC-LEDs auf epitaktisch lateral überwachsenen (ELO) AlN/Saphir-Basisschichten demonstriert, was das Potential zur Reduzierung der Chipkosten bietet. Eine weitere Verbesserung der Emissionsleistung wird durch die Kombination des HTA-Ansatzes mit dem ELO-Prozess erreicht. Das Wachstum von pseudomorphisch gewachsenen AlGa_N-Heterostrukturen auf der AlN-Pufferschicht kann die Bildung von Versetzungsschleifen verursachen, deren Vorhandensein die Emissionsleistung reduziert. Basierend auf den Ergebnissen dieser Studie nimmt die Dichte dieser Versetzungsschleifen mit der kompressiven Verzerrung und der Schichtdicke zu. Die Erzeugung der Versetzungsschleifen wird durch die Implementierung eines zweistufigen Heterostrukturansatzes für die *n*-Seite unterdrückt. Hierfür wird eine zweite AlGa_N:Si-Kontaktschicht mit niedrigem Al-Molanteil verwendet, die eine deutlich reduzierte Betriebsspannung bei gleichbleibender Emissionsleistung ermöglicht. Darüber hinaus können interne Polarisationsfelder die Bauelementleistung beeinflussen. Ein neuer Ansatz wird vorgestellt und untersucht, bei dem Kapazitäts-Spannungsmessungen zur genauen Bestimmung des Polarisationsfeldes verwendet werden. Sowohl die Stärke als auch die Richtung der ermittelten Polarisationsfelder stimmen mit den von der Theorie vorhergesagten Werten überein, wodurch zuverlässigere Bauelementsimulationen möglich sind. Die Lichtextraktionseffizienz ist einer der Schlüsselfaktoren für die Limitierung der LED-Effizienz. Die Anwendbarkeit von halbtransparenten *p*-Seiten wird untersucht. Durch die Kombination von transparenten *p*-AlGa_N Schichten mit einer dünnen *p*-Kontaktschicht aus GaN konnten LEDs mit einer erhöhten Lichtextraktionseffizienz realisiert werden. Die Untersuchungen dieser Arbeit führen zur Realisierung hocheffizienter UVC-LEDs mit Emissionsleistungen von 47 mW bei 350 mA, maximalen externen Quanteneffizienzen von 3,6% und Konversionseffizienzen von 2,7%.



List of publications

Parts of this work were published in the following articles:

Peer-reviewed articles

- **N. Susilo**, S. Hagedorn, D. Jaeger, H. Miyake, U. Zeimer, C. Reich, B. Neuschulz, L. Sulmoni, M. Guttman, F. Mehnke, C. Kuhn, T. Wernicke, M. Weyers, M. Kneissl, *AlGa_N-based deep UV LEDs grown on sputtered and high temperature annealed AlN/sapphire*, Applied Physics Letters **112**, 041110 (2018).
- **N. Susilo**, G. G. Roumeliotis, M. Rychetsky, M. Narodovitch, B. Witzigmann, M. Guttman, J. Enslin, T. Niermann, T. Wernicke, M. Lehmann, D. N. Papadimitriou, M. Kneissl, *Accurate determination of polarization fields in (0001) c-plane InAlN/GaN heterostructures with Capacitance-Voltage-Measurements*, Journal of Physics D: Applied Physics **51**, 485103 (2018).
- **N. Susilo**, M. Schilling, M. Narodovitch, H. Yao, X. Li, B. Witzigmann, J. Enslin, M. Guttman, G. G. Roumeliotis, M. Rychetsky, I. Koslow, T. Wernicke, T. Niermann, M. Lehmann, M. Kneissl, *Precise determination of polarization fields in c-plane GaN/Al_xGa_{1-x}N/GaN heterostructures with capacitance-voltage-measurements*, Japanese Journal of Applied Physics **58**, SCCB08 (2019).
- **N. Susilo**, J. Enslin, L. Sulmoni, M. Guttman, U. Zeimer, T. Wernicke, M. Weyers, M. Kneissl *Effect of the GaN:Mg Contact Layer on the Light Output and Current Voltage Characteristic of UVB LEDs*, Physica status solidi (a) **215**, 1700643 (2018).
- **N. Susilo**, E. Ziffer, S. Hagedorn, L. Cancellara, C. Netzel, N. Lobo Ploch, S. Wu, J. Rass, S. Walde, L. Sulmoni, M. Guttman, T. Wernicke, M. Albrecht, M. Weyers, M. Kneissl, *Improved performance of UVC-LEDs by combination of high temperature annealing and epitaxially laterally overgrown AlN/sapphire*, Photonics Research **8**, 04000589 (2020).

Magazine articles and awards

- **N. Susilo**, R. Stevenson et al., *UV LEDs: Slashing costs with sputtering*, Compound Semiconductor Magazine **24**, 60 (2018).
- **N. Susilo** et al., *Reducing the Dislocation Density within the AlN and AlGaN:Si Buffer Layers of Deep UVC-LEDs*, Best Oral Presentation Award, 18th Conference on Defects-Recognition, Imaging and Physics in Semiconductors 2019.
- **N. Susilo** et al., *Accurate determination of polarization fields in group III-Nitride heterostructures by capacitance-voltage measurements*, First Prize, International Nano-Optoelectronics Workshop 2019.
- **N. Susilo** et al., *AlGaN-based deep UV LEDs grown on sputtered and high temperature annealed AlN/sapphire*, Top cited Articles in Photonics and Optoelectronics research published in Applied Physics Letters.

International conferences

- **Invited talk:** N. Susilo et al., *AlGaN-based UV Emitters*, International Symposium Semiconductor Nanophotonics, Berlin, Germany.
- **Invited talk:** N. Susilo et al., *Growth and design of UVC laser heterostructures*, 1st International Workshop on AlGaN based UV-Laserdiodes 2019, JDZB, Berlin, Germany.
- N. Susilo et al., *Influence of the GaN:Mg contact layer on the electro-optical properties of UVB LEDs*, 17th European Workshop on Metalorganic Vapour Phase Epitaxy, Grenoble, France.
- N. Susilo et al., *Accurate determination of polarization fields in group III-nitride heterostructures by capacitance-voltage measurements*, 11th International Nano-Optoelectronics Workshop 2017, China.
- N. Susilo et al., *AlGaN-based UV-C LEDs emitting near 270 nm on low defect density AlN/sapphire templates*, International Conference on UV LED Technologies and Applications, Berlin, Germany.
- N. Susilo et al., *Polarization fields in c-plane GaN/AlGaN/GaN quantum wells determined by capacitance-voltage-measurements*, International Workshop on Nitride Semiconductors 2018, Kanazawa, Japan.

-
- N. Susilo et al., *AlGaN-based deep UV LEDs grown on sputtered and high temperature annealed AlN/sapphire*, International Workshop on Nitride Semiconductors 2018, Kanazawa, Japan.
 - N. Susilo et al., *Reducing the Dislocation Density within the AlN and AlGaN:Si Buffer Layers of Deep UVC-LEDs*, 18th Conference on Defects-Recognition, Imaging and Physics in Semiconductors 2019, Berlin, Germany.
 - N. Susilo et al., *AlGaN-based deep UV LEDs grown on high temperature annealed epitaxially laterally overgrown AlN/sapphire*, 13th International Conference on Nitride Semiconductors 2019, Seattle, USA.

Beyond this thesis, the following articles have been published:

Peer-reviewed articles

- S. Hagedorn, S. Walde, **N. Susilo**, C. Netzel, N. Tillner, R. Unger, P. Manley, E. Ziffer, T. Wernicke, C. Becker, H-J Lugauer, M. Kneissl, M. Weyers, *Improving AlN Crystal Quality and Strain Management on Nanopatterned Sapphire Substrates by High-Temperature Annealing for UVC Light-Emitting Diodes*, Physica Status Solidi A **217**, 1900796 (2020).
- S. Hagedorn, S. Walde, A. Knauer, **N. Susilo**, D. Pacak, L. Cancellara, C. Netzel, A. Mogilatenko, C. Hartmann, T. Wernicke, M. Kneissl, M. Weyers, *Status and prospects of AlN templates on sapphire for UV LEDs*, Physica Status Solidi (a), doi:10.1002/pssa.201901022 (2020).
- F. Römer, B. Witzigmann, M. Guttmann, **N. Susilo**, T. Wernicke, M. Kneissl, *Inhomogeneous spectral broadening in deep ultraviolet light emitting diodes*, Physics and Simulation of Optoelectronic Devices XXVII **10912**, 109120D (2019).
- C. Kuhn, L. Sulmoni, M. Guttmann, J. Glaab, **N. Susilo**, T. Wernicke, M. Weyers, M. Kneissl, *MOVPE-grown AlGaIn-based tunnel heterojunctions enabling fully transparent UVC LEDs*, Photonics Research **5**, B7 (2019).
- S. Walde, S. Hagedorn, P-M. Coulon, A. Mogilatenko, C. Netzel, J. Weinrich, **N. Susilo**, E. Ziffer, L. Matiwe, C. Hartmann, G. Kusch, A. Alasmari, G. Naresh-Kumar, C. Trager-Cowan, T. Wernicke, T. Straubinger, M. Bickermann, R. W Martin, P.A. Shields, M. Kneissl, M. Weyers, *AlN overgrowth of nano-pillar-patterned sapphire with different offcut angle by metalorganic vapor phase epitaxy*, Journal of Crystal Growth **531**, 125343 (2020).



Contents

1	Introduction to AlGa_N-based UVC-LEDs	1
1.1	Efficiency model of UVC-LEDs	4
1.2	Heterostructure design and MOVPE growth of UVC-LEDs . . .	5
1.3	Polarization fields in the MQW active region	8
2	UVC-LEDs on low defect AlN/sapphire templates	13
2.1	Preparation of UVC-LEDs on HTA AlN/sapphire templates . .	15
2.2	UVC-LEDs on sputtered HTA AlN/sapphire	18
2.2.1	Crystal quality of the sputtered HTA AlN/sapphire . . .	18
2.2.2	Dislocation density and RRE of AlGa _N MQWs	21
2.2.3	Emission power and EQE of UVC-LEDs	26
2.2.4	Summary and conclusion	28
2.3	UVC-LEDs on HTA ELO AlN/sapphire	29
2.3.1	Improved dislocation density and REE of AlGa _N MQWs	30
2.3.2	Enhanced efficiency of UVC-LEDs	36
2.3.3	Reduced operation-induced degradation	40
2.4	Summary and conclusion	42
3	Strain-induced defect generation in pseudomorphic AlGa_N:Si	43
3.1	Morphology, transparency and strain	45
3.2	Reduced device efficiency and defect generation	48
3.3	Heterostructure approach to suppress the defect generation . . .	50
3.4	Summary and conclusion	54
4	Determination of the polarization fields in the active region	55
4.1	Introduction to the CVM-based analytical approach	56
4.1.1	Derivation of the equations	56
4.1.2	Accuracy analysis	60
4.1.3	Advanced capacitance-voltage-profiling	61
4.2	CVM-based Poisson-carrier transport simulation approach . . .	63
4.3	Polarization fields predicted by DFT calculations	64
4.4	Sample structure of the pin-diodes	65

4.5	Spontaneous polarization field determination in InAlN/GaN . . .	67
4.6	Polarization field determination in AlGaN/GaN	71
4.7	Predicted polarization fields in AlGaN-based UVC-LEDs	76
4.8	Influence of the QCSE on the emission characteristics	77
4.9	Summary and conclusion	81
5	Enhanced light extraction using a semi-transparent p-side	83
5.1	Inhomogeneous growth and transparency of the GaN:Mg layer . .	84
5.2	Improved efficiency of the semi-transparent UVC-LEDs	88
5.3	Summary and conclusion	94
6	Summary and perspectives	97
7	Bibliography	101
	List of Figures	123
	List of Abbreviations	124
	List of Samples	127
	Acknowledgments	130

1

Introduction to AlGaIn-based UVC-LEDs

AlGaIn-based ultraviolet (UV) light emitting diodes (LEDs) with emission in the UVC wavelength range ($\lambda \leq 280$ nm) have attracted strong interest in the last years [1]. Significant progress has been made in terms of output power and reliability [2–6]. The reason for the high demand for UVC-LEDs is the wide range of applications for devices with UVC emission in combination with their unique properties, which make them superior to conventional UVC emitters such as mercury discharge lamps [7]. One of the main advantages of AlGaIn-based UVC-LEDs is that the emission wavelength can be adjusted to individual applications. Furthermore, UVC-LEDs offer the potential of long lifetimes, fast turn-on, robustness, low thermal heating as well as being environmentally friendly and compact in size [7]. Based on these advantages, UVC-LEDs can support many applications such as biochemical agent detection [8], disinfection and sterilization [9,10] as well as water purification [11–14]. Since the appearance of SARS-CoV-2 in December 2019 [15], people’s attention to disinfectant products has increased drastically. Meanwhile, over 5.7 million people have been infected by the ongoing pandemic of the coronavirus disease 2019 (COVID-19) [16]. It has been shown that UVC light can effectively inactivate other coronaviruses, which are close relatives of the SARS-CoV-2 virus [17], specifically the SARS-CoV-1 [18–20] and the MERS-CoV [21] virus. In particular, photons with an emission wavelength close to 265 nm can efficiently dimerize DNA and RNA molecules, which inhibits their ability to reproduce and inactivates them [3]. Accordingly, UVC-LEDs with an emission wavelength near 265 nm might be a practical solution to prevent the transmission of the SARS-CoV-2 virus by reducing contamination.

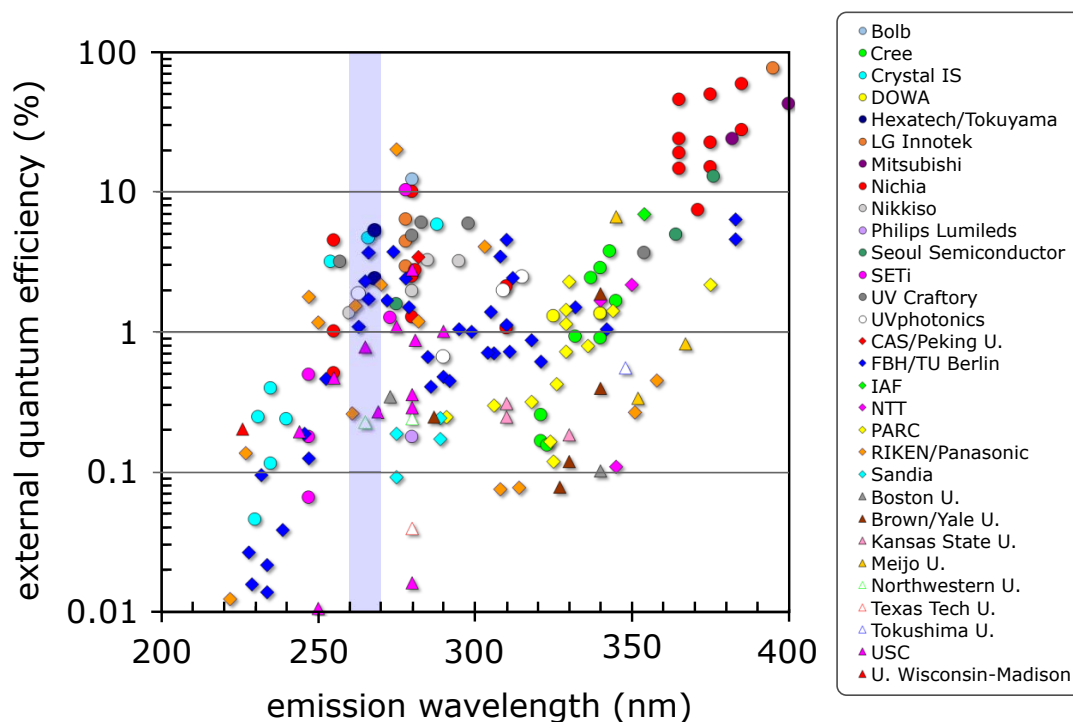


Figure 1.1: Reported values of the external quantum efficiencies of UV-LEDs [24]. The spectral wavelength range investigated in this work is marked in blue.

However, the external quantum efficiencies, one of the most important performance characteristics of UVC-LEDs (see section 1.1 for further details), are still modest and hinder the widespread use of these devices [1]. Figure 1.1 shows an overview of the EQE of state-of-the-art UV-LEDs. The EQE strongly reduces with decreasing emission wavelength for $\lambda \leq 365$ nm, corresponding to the change from InGaIn- to AlGaIn-based LED technologies [3]. In 2017 a peak EQE of 20% at a wavelength of 275 nm was achieved by a cooperation between Riken and Panasonic [22]. This value is the highest reported EQE in the entirely UVC and UVB spectral range. Based on the aforementioned findings that especially UV-light at 265 nm is highly efficient for the dimerization of DNA and RNA molecules, this thesis focuses on the spectral wavelength range between 260 nm and 270 nm (marked blue in Fig. 1.1). The highest reported EQE of 6.3% in this spectral emission wavelength range was presented by Tokuyama in cooperation with Hexatech ($\lambda = 265$ nm) [23]. Nevertheless, from a practical point of view, the optical emission power per chip is more crucial than the EQE for most applications. Therefore, this thesis focuses not only on the EQE but also on the optical emission power and additional performance parameters, which are described in the following section.

The structure of this thesis follows the main components of a UVC-LED heterostructure, i.e. the AlN base layer technology, the Si-doped AlGa_N *n*-side, the AlGa_N multi quantum well active region and the Mg-doped AlGa_N *p*-side. The focus of this thesis is the development of efficient UVC-LEDs emitting near 265 nm. In addition, a more fundamental study of the internal polarization fields occurring in UVC-LEDs is presented.

In chapter 2, the influence of the template technology for the realization of highly efficient UVC-LEDs is presented and discussed. In particular, the structural and electro-optical properties of AlGa_N-based UVC-LEDs on AlN/sapphire templates are investigated, for which different dislocation density reduction techniques have been used. Spectroscopic techniques such as cathodoluminescence, photoluminescence and electroluminescence as well as ray-tracing simulations are applied to gain insight into the influence of the template technology on the light extraction efficiency, internal quantum efficiency and external quantum efficiency.

In chapter 3, the heterostructure design of the *n*-side is analyzed and discussed. The compressively strained growth of the AlGa_N heterostructure on the AlN buffer can also lead to the generation of dislocations. The formation of these dislocations is studied and it is shown how this process can be successfully controlled by implementing a stacked *n*-AlGa_N heterostructure design with different Al mole fractions.

In chapter 4, the internal polarization fields, which can affect the internal quantum efficiency in addition to the dislocation density within the multi quantum well active region, are investigated. A precise knowledge of the polarization fields is crucial for the simulation of the electrical and optical characteristics of UVC-LEDs, which can show one way to design highly efficient heterostructures for these devices. A comprehensive and fundamental study of the spontaneous and piezoelectric polarization occurring in the active region is presented. In particular, a new approach is developed, applied and quantified using capacitance-voltage measurements to accurately determine the internal polarization fields. The approach is based on the change in the width of the depletion region caused by the polarization sheet charges. A special *pin*-diode heterostructure and an advanced capacitance-voltage profiling method are developed to improve the accuracy of the polarization field determination.

In chapter 5, the design of the p -doped AlGaIn layers is investigated. In order to increase the light extraction efficiency, the influence of a semi-transparent p -side on the performance characteristics of UVC-LEDs is studied. Accordingly, a p -side heterostructure is designed which includes transparent p -layers and an absorbing GaIn:Mg contact layer in combination with a UV-reflective p -electrode contact to enable improved light extraction and the formation of p -electrode contacts with low contact resistance.

1.1 Efficiency model of UVC-LEDs

The key parameters for the evaluation of the performance of UVC-LEDs are the external quantum efficiency η_{EQE} (EQE), the wall-plug efficiency η_{WPE} (WPE) and the optical emission power P_{out} . The EQE is a product of the carrier injection efficiency (CIE), the radiative recombination efficiency (RRE) and the light extraction efficiency (LEE).

- The carrier injection efficiency η_{CIE} describes the ratio of charge carriers recombining within the active region to the total number of injected charge carriers.
- The radiative recombination efficiency η_{RRE} is the ratio between the UVC photons generated by radiative recombination and the total number of recombination processes within the AlGaIn quantum wells.
- The light extraction efficiency η_{LEE} describes the ratio of the UVC photons escaping from the semiconductor chip to the total number of UVC photons generated in the AlGaIn quantum wells.

Furthermore, the product of CIE and RRE is often referred to as the internal quantum efficiency η_{IQE} (IQE). The EQE can be calculated from the optical emission power P_{out} , the drive current I and the emission wavelength λ (see Eq. 1.1 [3]), where e is the elementary charge, h the Planck constant and c the speed of light). The WPE also takes into account the operating voltage V and can be determined by the ratio of the optical emission power P_{out} to the electrical input power $P_{\text{el}} = I \times V$ (see Eq. 1.2 [3]). By using Eq. 1.1 as well as the electrical efficiency η_{el} a relation between the WPE and the EQE can be expressed. It should be noted that variations of the UVC-LED structure can strongly influence all these efficiencies, which provides the basis for this thesis.

$$\eta_{\text{EQE}} = \eta_{\text{CIE}} \times \eta_{\text{RRE}} \times \eta_{\text{LEE}} = \eta_{\text{IQE}} \times \eta_{\text{LEE}} = \frac{e\lambda}{hc} \times \frac{P_{\text{out}}}{I} \quad (1.1)$$

$$\eta_{\text{WPE}} = \frac{P_{\text{out}}}{P_{\text{el}}} = \frac{P_{\text{out}}}{I \times V} = \eta_{\text{EQE}} \times \frac{hc}{\lambda \times e \times V} = \eta_{\text{EQE}} \times \eta_{\text{el}} \quad (1.2)$$

1.2 Heterostructure design and MOVPE growth of UVC-LEDs

For the realization of highly efficient AlGaIn-based LEDs with emission in the UVC spectral range, the considerations listed below should be taken into account, which will be discussed in detail later in the respective chapters. In a simplified picture, UVC-LEDs are based on an AlGaIn multi quantum well (MQW) active region embedded in *n*- and *p*-doped AlGaIn layers grown on a template (see Fig. 1.2). All these components must fulfill certain requirements for emission in the UVC spectral range, which are briefly described below.

- The template is used as a carrier for the heteroepitaxial grown AlGaIn layers and must offer a crystalline surface allowing the growth of layers with a low dislocation density. In addition, the template should be transparent for the emission wavelength, since AlGaIn-based UVC-LEDs usually emit through the template due to the high absorption of the *p*-layers and *p*-electrodes [1] (see chapter 2 for further details).
- The AlGaIn:Si *n*-side must exhibit a high vertical as well as lateral *n*-type conductivity, since the *n*-contacts are usually deposited on an etched layer [1]. Furthermore the AlGaIn:Si *n*-side must be transparent for the emission wavelength at 265 nm and should ideally maintain the threading dislocation density (TDD) determined by the template. Finally, the *n*-side should enable the formation of *n*-electrode contacts with low contact resistance (see chapter 3 for further details).
- The AlGaIn-based MQW active region is the light-emitting part of the UVC-LED. The confinement of charge carriers is obtained by quantum wells which are separated by barriers with a higher bandgap energy. The charge carriers are injected from the *n*- and *p*-side and recombine radiatively

or non-radiatively in the AlGaIn quantum wells. In order to realize efficient UVC-LEDs, the radiative recombination rate needs to be maximized. However, strong polarization fields (see following section 1.3) as well as non-radiative recombination centers, such as point defects and threading dislocations occurring in the active region, lead to a reduced radiative recombination rate (see chapter 4 for further details).

- The AlGaIn:Mg p -side should provide a high vertical p -type conductivity in order to supply the AlGaIn-based MQW active region with sufficient holes. Furthermore, the electron blocking heterostructure as part of the p -side is needed to confine the electrons in the MQW active region and suppress electron leakage towards the p -side. In addition, UV-transparent p -side layers in combination with highly UV-reflective p -electrode contacts can be used to enhance the emission power. Similar to the n -side the p -side should enable the formation of p -electrode contacts with low contact resistance. However, high conductivities and low contact resistances are difficult to achieve for UV-transparent p -side layers due to low hole mobilities and high Mg activation energies [25–27] (see chapter 5 for further details).

The named boundary conditions result in the following basic heterostructure design for AlGaIn-based UVC-LEDs: The AlN/sapphire template is followed by an AlN-AlGaIn transition layer, an AlGaIn buffer layer, an AlGaIn:Si n -side current spreading layer, an AlGaIn-based MQW active region, an AlGaIn(:Mg) electron blocking heterostructure and a GaN:Mg p -side (see Fig. 1.2). The exact layer structure, compositions and thicknesses, as well as discussions of the challenges for the individual layers and their influence on the device efficiency are specified in the corresponding chapters. It should be noted that the optimization of the UVC-LED heterostructure is a continuous process. Accordingly, the heterostructure may vary from chapter to chapter based on the experiments described and the findings from the literature.

The AlGaIn-based layers and UVC-LED heterostructures were grown by metal-organic vapor phase epitaxy (MOVPE) in a Close Coupled Showerhead (CCS) system. For the epitaxial growth standard precursors, i.e. trimethylaluminum (TMAl), trimethylgallium (TMGa), triethylgallium (TEGa) and ammonia (NH₃) were used. Silane (SiH₄) and biscyclopentadienyl-magnesium (Cp₂Mg) were used as n -type and p -type dopant sources, respectively. The precursors are transported to the reactor using hydrogen (H₂) or nitrogen (N₂) as inert carrier gas. The

UVC-LED heterostructure

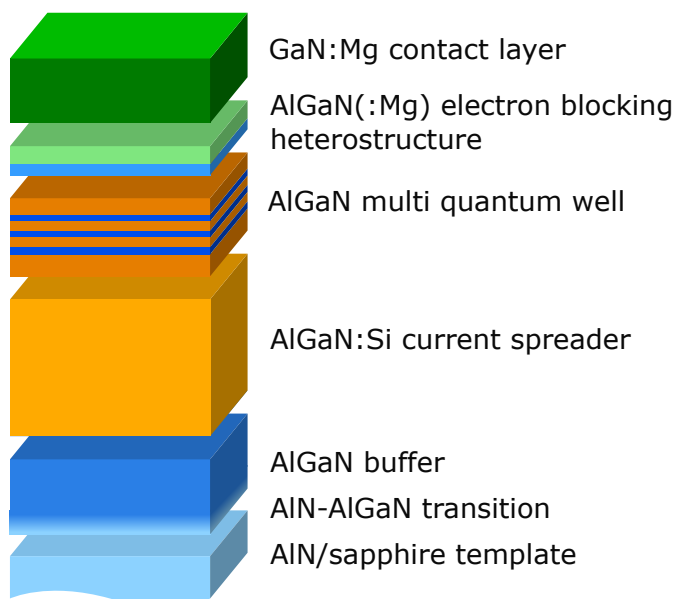


Figure 1.2: Schematic of the AlGaIn-based UVC-LED heterostructures. The exact layer structure, compositions and thicknesses are specified in the corresponding chapters.

CCS system allows a gas inlet near the substrate surface with an adjustable gap between 5 mm and 26 mm, minimizing vapor-phase pre-reactions [28]. The resistively heated susceptor is made of graphite with a silicon carbide coating and has a capacity of up to three substrates with 2-inch diameter. The layers were grown at temperatures between 900 °C and 1100 °C and reactor pressures between 200 mbar and 600 mbar. Due to the high NH_3 pyrolysis temperature [29, 30], a high group-V to group-III partial pressure ratio between 20 and 5000 was used. A detailed description of the growth and surface processes is given by U. W. Pohl [31]. In-situ measurements were performed through the openings in the reactor lid with a LayTec EpiTT and EpiCurve system, which allows for measurements of the surface reflectivity at 406 nm, 633 nm and 951 nm, the emissivity corrected pyrometric susceptor temperature and the wafer curvature [32–34]. The growth rates as well as the layer thicknesses were determined in-situ by fitting the reflectivity transients [35], while the Al mole fractions were analyzed ex-situ by high-resolution X-ray diffraction (HRXRD) [36]. The structural and electro-optical properties were analyzed using several spectroscopic techniques such as cathodoluminescence (CL) spectroscopy, photoluminescence (PL) spectroscopy and electroluminescence (EL) spectroscopy as well as microscopy techniques such as atomic force microscopy (AFM), scanning electron microscopy (SEM) and transmission electron microscopy (TEM).

1.3 Polarization fields in the MQW active region

In wurtzite crystals macroscopic electric polarization fields are generated perpendicular to the basal plane along the c -axis [37]. The difference of the microscopic polarization at heterointerfaces leads to polarization sheet charges [38]. In a double heterostructure the polarization charges act like a parallel plate capacitor [40]. The generated polarization fields lead to a bending of the energy bands within the AlGaN quantum well, resulting in a lower emission energy and a reduction of the wave function overlap [41], which is known as the quantum confined Stark effect (QCSE) [42]. Figure 1.3 shows a Schrödinger-Poisson-Drift-Diffusion simulation [39], at a current density of 40 A/cm^2 , of the conduction and valence band edges of a UVC-LED depicting the band bending due to the QCSE. In addition, the ground state electron wave functions (red) and hole wave functions (blue) within the AlGaN-based MQW active region is shown. In the presence of the QCSE, the hole and the electron wave functions separate spatially leading to a reduced overlap and a lower recombination rate [43] which can reduce the device efficiency. Nevertheless, nearly all commercially available III-nitride-based devices are grown in the c -direction, regardless of the QCSE [44]. In order to correctly describe the carrier transport and recombination in III-nitride semiconductor devices, an accurate determination of the magnitude and direction of the polarization fields is crucial. Unfortunately, the internal field strength

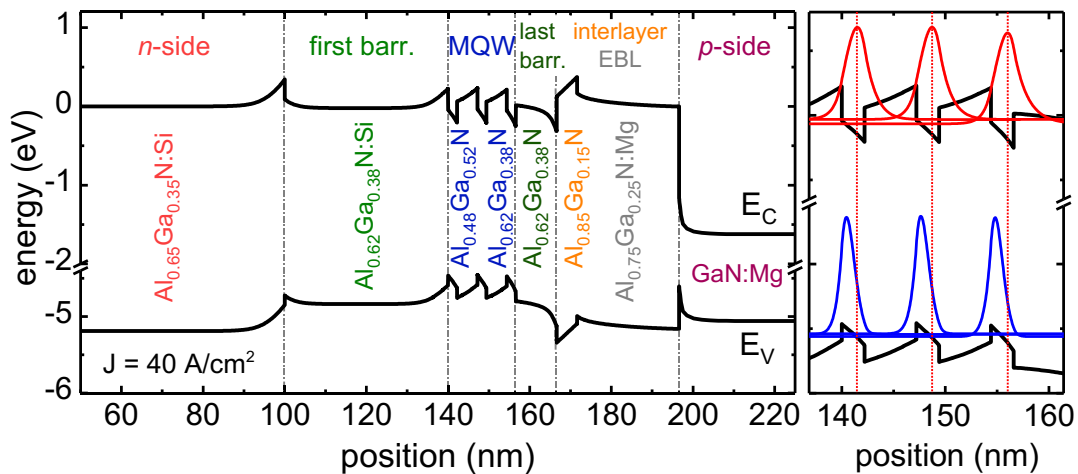


Figure 1.3: Calculated conduction and valence band edge profiles (black) of a UVC-LED. Depicted is the band bending due to the QCSE and the spatial separation of the ground state of the electron (red) and of the hole wave functions (blue) within the AlGaN-based MQW active region. The one-dimensional Schrödinger-Poisson-Drift-Diffusion simulation was performed with SiLENSe [39]. Simulation performed by M. Guttman, TUB.

in III-nitride-based optical devices is still controversially discussed [45]. There are different theoretical models in the literature for calculating the internal polarization fields in III-nitride-based heterostructures [44, 46]. However, the magnitude and the sign of the single parameters, are controversial [45] (see section 4.3 for further details). In chapter 4, a new experimental approach is presented, examined and discussed, which allows for the accurate determination of the magnitude and the direction of polarization fields.

In the following, the theoretical background of the spontaneous and piezoelectric polarization is briefly described. A detailed discussion is given by Ambacher et al. [46].

Spontaneous polarization

The spontaneous polarization is an intrinsic material property of wurtzite crystals. The bond configuration in the wurtzite structure is tetrahedral, with the metal atom having significantly lower electronegativities than the nitrogen atom. The values for Al and Ga are in the range between 1.5 and 1.6 and 3.0 for N [47]. Due to this partially ionic nature of the bonds a polarization vector can be defined. However, after summation of all single bonds the total polarization would be zero for a perfect sp^3 -hybridisation. In this case the lattice constant c and the lattice constant a is given by

$$a = \frac{8}{3}b \quad c = \sqrt{\frac{8}{3}}b \quad \frac{c}{a} \approx 1.633 \quad (1.3)$$

where b is the bond length [46]. In case of AlN and GaN the c/a -ratio deviates from the ideal value. Figure 1.4 shows that the c/a -ratio for wurtzite AlGa_xN crystals is always below the value of an ideal hexagonal crystal and decreases with increasing Al mole fraction. Consequently, the metal-nitrogen bond length along the c -axis is 0.7%-0.9% longer than the three bonds in the direction of the basal plane (Fig. 1.4). This deviation results in a charge displacement along the c -axis and the total polarization in c -direction does not vanish after summation of all single bonds. In an AlGa_xN quantum well the differences in the spontaneous polarizations of well and barrier lead to electrostatic fields, which are calculated by

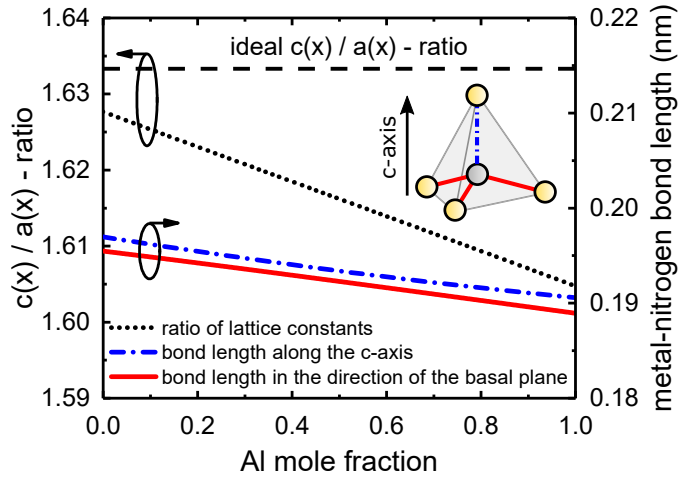


Figure 1.4: c/a -ratio of AlGa_N at room temperature [48] and the bond length of the metal–nitrogen bond along the c -axis and in the direction of the basal plane as a function of the Al mole fraction [46].

$$\vec{E}^{sp} = \frac{P_{barr}^{sp} - P_{QW}^{sp}}{\epsilon_0 \cdot (\epsilon_r - 1)} \vec{e}_c = \frac{\Delta P^{sp}}{\epsilon_0 \cdot (\epsilon_r - 1)} \vec{e}_c. \quad (1.4)$$

Here, \vec{E}^{sp} is the electrostatic spontaneous polarization field, ΔP^{sp} is the difference of the spontaneous polarization coefficients, ϵ_0 the vacuum permittivity, ϵ_r the relative permittivity and \vec{e}_c is the unit vector along c -axis. It is notable here that a positive sign of Eq. 1.4 means that the electrostatic field is oriented in the c -direction. Typical values for the spontaneous polarization field of an AlN/AlGa_N interface are in the range of MV/cm (see chapter 4). However, the values reported in the literature for the spontaneous polarization coefficients yields a wide scatter of parameters and even the direction of the spontaneous polarization field is controversial [45]. The spontaneous polarization field for alloys is usually obtained by linear interpolation.

Piezoelectric polarization

In addition to the spontaneous polarization fields, piezoelectric polarization fields arise in AlGa_N due to mechanical strain. The larger lattice constant of GaN compared to AlN leads to a compressive strain in a pseudomorphically grown AlGa_N quantum well. Due to the compressive strain the tetrahedral bond length and bond angle deviate from the unstrained case and the charge separation increases (see Fig. 1.5). Consequently, in order to calculate the piezoelectric polarization field the elastic strain tensor ϵ must be known. The piezoelectric polarization in Voigt's notation for hexagonal crystal structures is given by

$$\vec{P}^{pz} = \begin{pmatrix} 0 & 0 & 0 & 0 & e_{15} & 0 \\ 0 & 0 & 0 & e_{15} & 0 & 0 \\ e_{31} & e_{31} & e_{33} & 0 & 0 & 0 \end{pmatrix} \begin{pmatrix} \epsilon_1 \\ \epsilon_2 \\ \epsilon_3 \\ \epsilon_4 \\ \epsilon_5 \\ \epsilon_6 \end{pmatrix} = \begin{pmatrix} e_{15}\epsilon_5 \\ e_{15}\epsilon_4 \\ e_{31}(\epsilon_1 + \epsilon_2) + e_{33}\epsilon_3 \end{pmatrix}, \quad (1.5)$$

where \mathbf{e} is the piezoelectric tensor, with $e_{15} = e_{24} \neq 0$, $e_{31} = e_{32} \neq 0$, $e_{33} \neq 0$ and $e_{kl} = 0$ otherwise [46]. For layers grown in the c -direction a common simplification is to assume $\epsilon_4 = \epsilon_5 = 0$ due to negligible shear strains and $\epsilon_1 = \epsilon_2$ due to biaxial strain [46]. Furthermore, the strain along the c -axis ϵ_3 can be expressed by the strain in the direction of the basal plane

$$\epsilon_3 = -2 \frac{C_{13}}{C_{33}} \epsilon_1, \quad (1.6)$$

where C_{13} and C_{33} are the elastic constants [46]. Thus, Eq. 1.5 has only one non-vanishing component P^{pz} , which is directed along the growth direction and is given by

$$P^{pz} = 2\epsilon_1 \left(e_{31} - e_{33} \frac{C_{13}}{C_{33}} \right) \quad \epsilon_1 = \frac{a - a_0}{a_0} \quad (1.7)$$

$$\vec{E}^{pz} = \frac{P^{pz}}{\epsilon_0 \cdot (\epsilon_r - 1)} \vec{e}_c. \quad (1.8)$$

Here, \vec{E}^{pz} is the electrostatic piezoelectric polarization field. The strain in the basal plane ϵ_1 is the relative change of the lattice constant a with respect to the constant of the relaxed crystals a_0 . Note that the piezoelectric polarization P^{pz} in the c -direction is linearly dependent on the relative change of the lattice constant a . Furthermore, the piezoelectric polarization P^{pz} is positive for layers under biaxial compressive strain. Accordingly, the piezoelectric polarization in an AlGaIn quantum well under biaxial compressive strain is oriented along the [0001]-axis. Similar to the spontaneous polarization, sheet charges are generated in order to compensate the change of the polarization. In contrast to the spontaneous polarization, the piezoelectric polarization is in principle relatively easy to calculate [45]. Nevertheless, the reported values for the piezoelectric

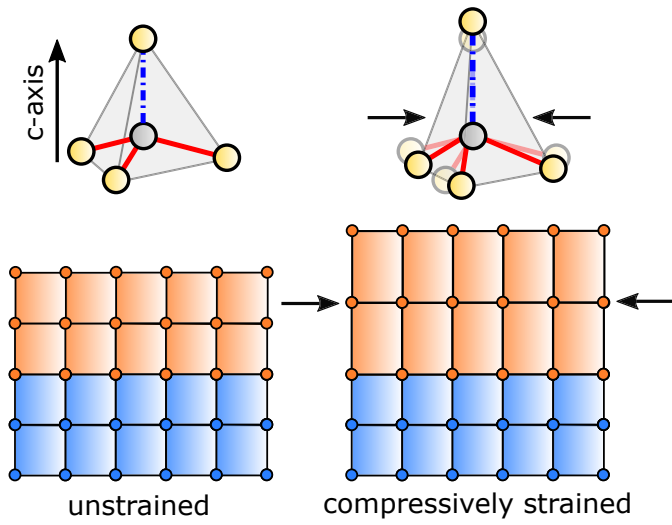


Figure 1.5: Compressive strained growth which leads to a deformation of the tetrahedron and a change of the bond length and bond angle.

tensor elements e_{31} and e_{33} , exhibit a considerable spread [44]. As an example, the use of so-called improper and proper piezoelectric tensor elements [49, 50], is often discussed controversially, even though it can give rise to significant changes in the total polarization field [45].

2

UVC-LEDs on low defect AlN/sapphire templates

For the realization of high-power AlGaIn-based LEDs with emission in the UVC wavelength range, a suitable substrate must be implemented. The substrate should enable the growth of AlGaIn layers with high Al mole fraction and be transparent to the quantum well emission in order to allow light extraction through the backside of the substrate (bottom emission). For the growth of AlGaIn, several substrates, such as Si, SiC, monocrystalline AlN and GaN, or sapphire can be considered [51]. However, Si ($E_g = 1.13$ eV [52]), SiC ($E_g = 2.9$ eV [53]) and GaN ($E_g = 3.51$ eV [54]) substrates are not suitable for the growth of UVC-LEDs with bottom emission configuration due to the too small bandgap and the resulting fundamental absorption of UVC light. Monocrystalline AlN as a substrate is the natural choice for AlGaIn-based LEDs [55]. However, it is currently hardly commercially available and still suffers from limited size (≤ 2 inch) and high costs [55]. In addition, below-bandgap optical absorptions caused by point defects in the blue and UV spectral wavelength range are usually observed, which are detrimental to the UVC transparency [56–58]. Consequently, most AlGaIn-based UVC-LEDs are grown on (0001) *c*-plane sapphire substrates [2], which is fully transparent for the UVC light due to its large bandgap ($E_g = 8.8$ eV [59]). Furthermore, sapphire substrates are available in various sizes and are relatively inexpensive [1]. For these reasons, the AlGaIn-based heterostructures presented in this thesis were grown on AlN/sapphire templates. Unfortunately, due to the large lattice mismatch between the sapphire substrate and the epitaxial AlGaIn layers (14% between sapphire and AlN [3]) in combination with the low surface mobility of the Al species on the growth surface, the TDD for non-optimized AlGaIn layers on sapphire substrates is usually in

the range of 10^{10} cm^{-2} [60,61]. Such high TDDs impede the production of high efficiency UVC-LEDs, which require dislocation densities below 10^9 cm^{-2} [1,62].

Typically, the TDD of AlN layers on sapphire is reduced by mutual annihilation of dislocations during the growth of thick layers [63]. Nevertheless, the large lattice mismatch limits the critical layer thickness after which crack formation occurs to around 1-2 μm [63]. To overcome crack formation in thick AlN layers various techniques have been developed. Many approaches involve a variety of complex growth steps to achieve strain management, e.g. by lateral overgrowth of N polar AlN domains with Al polar AlN [64] and by roughening through a high group V to group III (V/III) partial pressure ratio [65]. The resulting TDDs of the AlN layers are usually in the order of $1 \times 10^9 \text{ cm}^{-2}$, which is suitable but not sufficient for high efficient UVC-LEDs [1]. In addition, due to the mismatch of the thermal expansion coefficients between AlN and sapphire, such thick AlN layers exhibit strong wafer bows of more than 600 km^{-1} at room temperature [66]. This can lead to problems while the micro-fabrication process of LED wafers, such as inhomogeneous exposure of photoresist during photolithography and inhomogeneous lasing scribing depth during chip dicing. It has been demonstrated that both the critical layer thickness for crack formation and the TDD can be reduced by using epitaxially laterally overgrown (ELO) AlN/sapphire templates [67]. However, the fabrication of ELO AlN/sapphire templates includes complex photolithography and dry etching steps as well as a second AlN overgrowth by MOVPE [68]. In recent years, several publications have shown the beneficial influence of high temperature annealing (HTA) on the crystal quality of AlN [69]. Miyake et al. [69] found that HTA leads to a restructuring of AlN between the buffer layer grains. They achieved a TDD of $4.7 \times 10^8 \text{ cm}^{-2}$ for 2.3- μm -thick MOVPE-grown AlN layers using a 300-nm MOVPE-grown AlN buffer layer on sapphire, previously annealed in carbon oxide saturated N_2 -CO atmosphere at temperatures higher than $1500 \text{ }^\circ\text{C}$. Annealing in pure N_2 atmosphere is also possible by placing the AlN/sapphire templates face-to-face for surface stabilization during HTA, which also has been successfully applied to sputtered AlN layers [70].

In the following chapter, the applicability of HTA-based AlN/sapphire templates for the realization of AlGaIn-based heterostructures and UVC-LEDs is investigated and discussed. For this purpose, UVC-LEDs on both sputtered- and MOVPE-based HTA AlN/sapphire templates are investigated and compared to UVC-LEDs on ELO AlN/sapphire templates.

2.1 Preparation of UVC-LEDs on HTA AlN/sapphire templates

The heterostructures and UVC-LEDs presented in this thesis were grown exclusively on AlN/sapphire templates using (0001) *c*-plane sapphire. In the following, the fabrication processes of the different templates investigated in this chapter are briefly described.

Sputtered HTA AlN/sapphire¹ templates were prepared with a ClusterlineTM 200 from Evatec in order to deposit AlN layers with thicknesses of 150 nm and 350 nm. The substrates were heated homogeneously to 700 °C by infrared-radiation. The films were reactively sputtered from an Al target with a purity of 99.9995% in an argon-nitrogen ambient with a gas flow ratio of Ar:N₂ = 20:60. The power density of the physical vapour deposition was 3.5 W/cm², leading to a deposition rate of 0.4 nm/s. Subsequently, the sputtered AlN layers were high temperature annealed in N₂ ambient at 1700 °C as described by Miyake et al. [70]. The surface of the AlN layer was covered face-to-face with another sample to suppress the thermal decomposition of the AlN layers as illustrated in Fig. 2.1. Finally, the sputtered HTA AlN/sapphire templates were overgrown with 400-nm AlN by MOVPE (Fig. 2.2(a)).

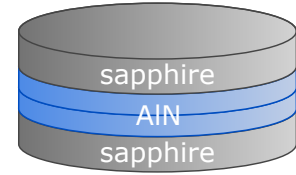


Figure 2.1: Face-to-face configuration during HTA to suppress thermal decomposition of the AlN layers.

MOVPE HTA AlN/sapphire² templates were fabricated with an 11 × 2 inch Aix2400G3-HT planetary reactor using TMAI, NH₃ and H₂ as carrier gases. Thermal in-situ cleaning of the sapphire substrates was carried out by annealing at 1150 °C in H₂ atmosphere. Dislocation and tensile strain management was achieved by roughening and subsequent smoothing of the AlN layer during growth [65, 71, 72]. First, a 50-nm nucleation layer was deposited on the sapphire at a temperature of 980 °C and a V/III ratio of 4000 [61]. After nucleation, AlN layers were grown at temperatures above 1140 °C and a V/III ratio of 540 resulting in a roughening of the surface. Subsequently, smooth layers were achieved by reducing the V/III ratio to 30. After epitaxial growth, face-to-face HTA was performed in N₂ ambient at 1000 mbar and 1700 °C for 3 h (Fig. 2.2(b)).

¹The sputtering was performed by D. Jaeger, Evatec AG, the HTA by H. Miyake, Mie University and the MOVPE growth of AlN by S. Hagedorn, FBH.

²The MOVPE growth of AlN on sapphire and the HTA was performed by S. Hagedorn, FBH.

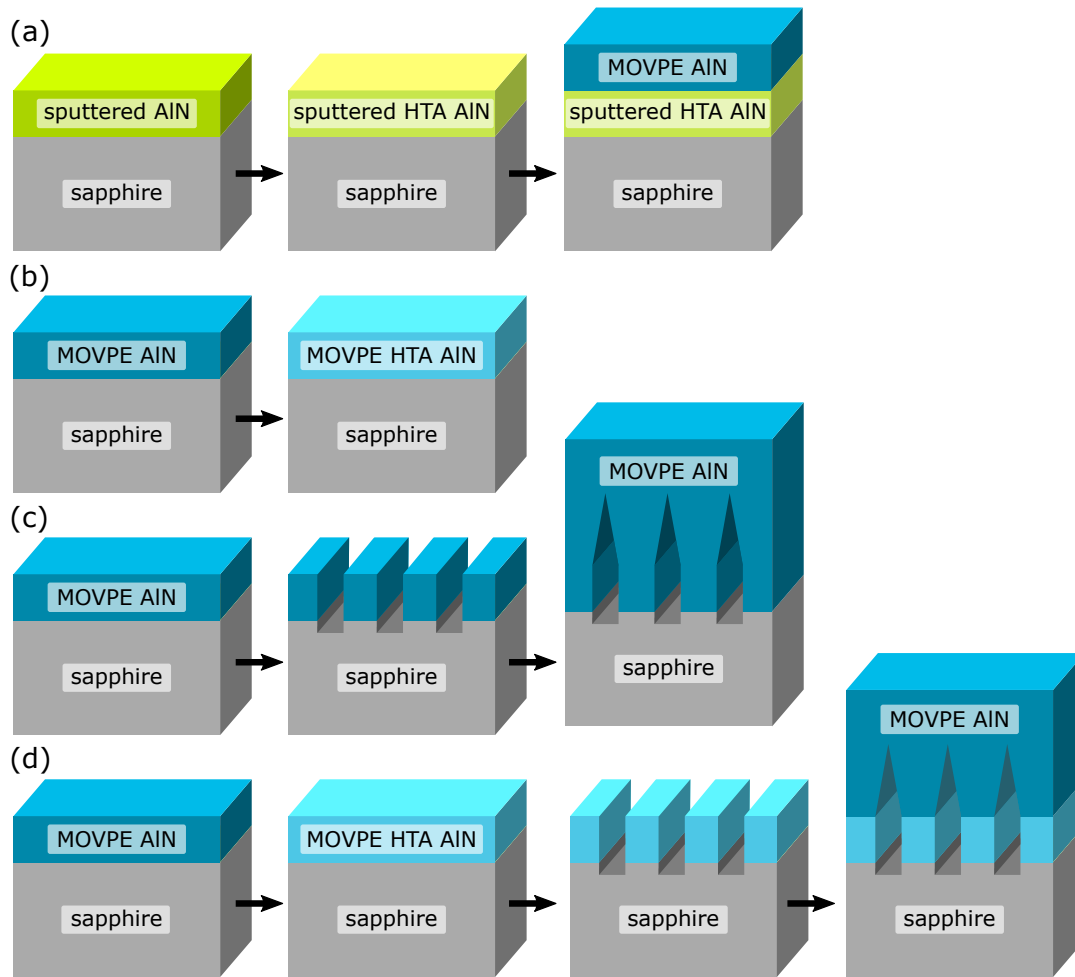


Figure 2.2: Schematic of the template fabrication process of (a) sputtered and HTA AlN/sapphire, (b) MOVPE and HTA AlN/sapphire, (c) MOVPE ELO AlN/sapphire and (d) MOVPE HTA ELO AlN/sapphire.

MOVPE ELO AlN/sapphire³ templates were produced similarly to the MOVPE HTA AlN/sapphire templates. However, after epitaxial growth of 500-nm AlN, a SiN mask was deposited on the templates and patterned into stripes by photolithography and reactive ion etching. Stripes of 1.5- μm width and a period of 3 μm were etched into the AlN by anisotropic plasma etching [73]. After removal of the SiN mask by wet etching [68], these layers were overgrown with 5.5- μm AlN, whereby coalescence was achieved after 3.0 μm (Fig. 2.2(c)). It is worth noting here that due to the much larger size of the *p*-metal contact compared to the width and period of the ELO voids, the UVC-LED devices include both the reduced TDD region above the ELO trenches and the higher TDD region above the ELO ridges.

³The ELO process was performed by S. Hagedorn, FBH.

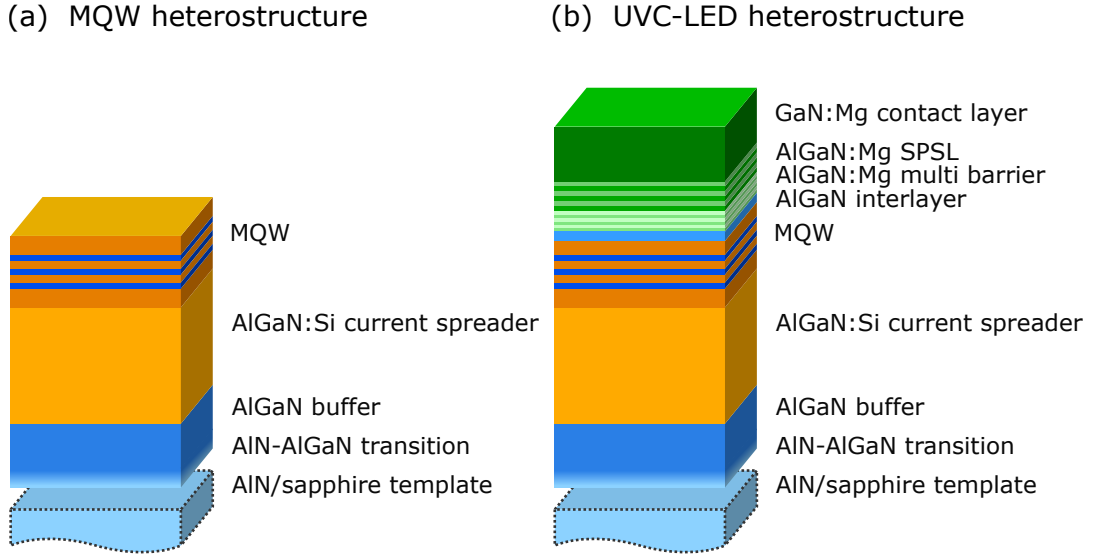


Figure 2.3: Schematic of the (a) MQW heterostructure and (b) UVC-LED heterostructure grown on the sputtered and HTA AlN/sapphire templates and the ELO AlN/sapphire templates.

MOVPE ELO HTA AlN/sapphire templates were fabricated similarly to the ELO AlN/sapphire template. However, the first 500-nm AlN film was face-to-face annealed at 1700 °C in N₂ ambient before patterning to reduce the TDD in the AlN seed layer on the etched stripes (Fig. 2.2(d)).

Subsequently, AlGaN-based UVC-LED heterostructures with an emission wavelength near 265 nm were grown on the AlN/sapphire templates by MOVPE in a CCS system (see section 1.2 for further details). The heterostructures are shown schematically in Fig. 2.3. First, a 600-nm-thick homoepitaxial AlN buffer layer was deposited on top of the AlN/sapphire templates to provide a clean and smooth AlN surface for AlGaN growth, followed by a 25-nm-thick transition layer from AlN to Al_{0.76}Ga_{0.24}N, a 100-nm-thick Al_{0.76}Ga_{0.24}N buffer and a 1.2-μm-thick Al_{0.76}Ga_{0.24}N:Si current spreading layer. The active region consists of a threefold Al_{0.62}Ga_{0.38}N/Al_{0.48}Ga_{0.52}N MQW, followed by a 5-nm-thick Al_{0.85}Ga_{0.15}N interlayer, a 25-nm-thick Al_{0.80}Ga_{0.20}N:Mg/Al_{0.70}Ga_{0.30}N:Mg multi barrier, a 60-nm-thick Al_{0.27}Ga_{0.73}N:Mg/Al_{0.17}Ga_{0.83}N:Mg short-period superlattice (SPSL) and a 160-nm-thick GaN:Mg contact layer. In addition, AlGaN-based MQW samples were grown to enable investigations using CL and PL spectroscopy. In order to avoid absorption in the *p*-side, the heterostructure of the MQW samples is nominally identical to the one of the UVC-LEDs, except for the omission of *p*-layers (Fig. 2.3(a)). Note that in section 2.3, slightly different heterostructures (Fig. 2.11) were used owing to lower operating voltages

and thus higher WPE for flip-chip LEDs (see section 2.3 and section 3). After epitaxial growth, the UVC-LED heterostructures were processed by standard micro-fabrication techniques using palladium-based *p*-contacts and vanadium-based *n*-contacts [7]⁴.

2.2 UVC-LEDs on sputtered HTA AlN/sapphire

In this section, the performance characteristics of UVC-LEDs grown on sputtered HTA AlN/sapphire (SP-HTA AlN) templates are investigated. An additional UVC-LED on MOVPE ELO AlN/sapphire (ELO AlN) was used for comparison. The AlGaN-based heterostructures were grown simultaneously on the 150-nm- and 350-nm-thick SP-HTA AlN template as well as on the ELO AlN template.

2.2.1 Crystal quality of the sputtered HTA AlN/sapphire

The surface morphology of the AlN/sapphire template is crucial for the growth of the AlGaN-based heterostructure. A surface with large roughness, featuring high macro steps can be detrimental to the AlGaN growth of the active region as an increased Ga incorporation takes place at the step edges, leading to variations in the Al mole fraction [74] and finally to parasitic luminescence in the emission spectrum [75]. Figure 2.4 shows the surface morphology measured by AFM of the 150-nm sputtered AlN/sapphire template before HTA, after HTA and after the overgrowth with 400-nm AlN by MOVPE. Before annealing, small columnar structures cover the whole surface (Fig. 2.4(a)). A high root-mean-square (RMS) surface roughness of 2.3 nm in a measurement area of 4 μm^2 is recorded. Nevertheless, the homogeneity of the columnar structures indicates how uniform the deposition of AlN by sputtering is [70]. After annealing, the columnar structures coalesce into a stepped surface morphology, resulting in a relatively smooth surface with an RMS surface roughness of 0.5 nm in a measuring range of 4 μm^2 (Fig. 2.4(b)). In order to further smooth the surfaces, a 400-nm homoepitaxial AlN layer with a low V/III ratio was deposited by MOVPE. After MOVPE overgrowth, surfaces with bilayer steps with a step height of $c/2$ were achieved as shown in the AFM topograms in Fig. 2.4(c) for

⁴The micro-fabrication process was performed by L. Sulmoni, TUB.

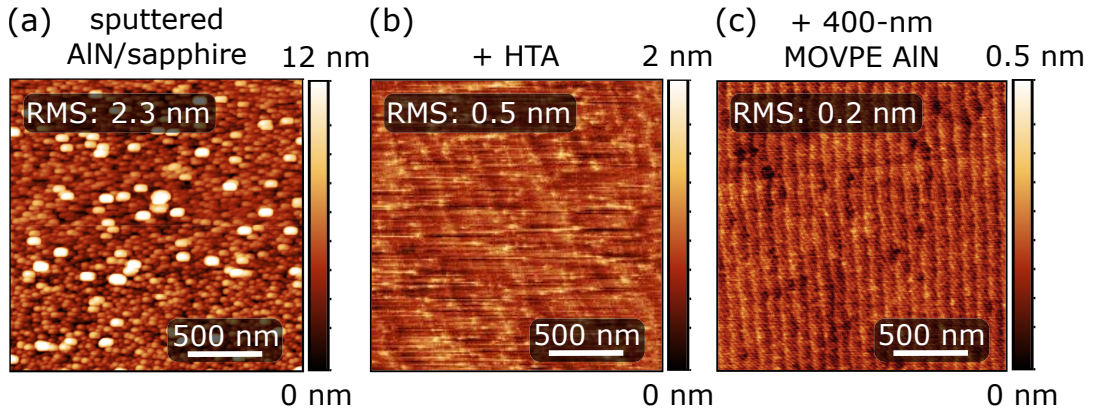


Figure 2.4: AFM topograms of sputtered AlN/sapphire templates, before HTA, after HTA and after overgrowth with 400-nm AlN by MOVPE. Measurements performed by S. Hagedorn, FBH.

the 150-nm-thick SP-HTA AlN template. The surfaces show an RMS surface roughness of 0.2 nm in a measurement area of $4 \mu\text{m}^2$, which is typical for step flow growth. This value is similar to the ELO AlN surface and is suitable for the growth of highly efficient UVC-LED heterostructures [66].

To gain insight into the crystal quality, the sputtered 150-nm- and 350-nm-thick AlN layers were analyzed by HRXRD before HTA, after HTA and after the overgrowth with 400-nm MOVPE AlN [76]. Figure 2.5 shows the rocking curve full width at half maximum (RC-FWHM) of the symmetric (0002) and of the asymmetric $(10\bar{1}2)$ AlN-reflection for the AlN/sapphire templates. The $(10\bar{1}2)$ AlN-reflection was measured with $\omega = \theta$ and a χ offset was used to obtain skew symmetry [36]. It should be noted that due to the high penetration depth in both diffraction geometries the broadening of the X-ray reflections is affected by the total sample depth [36]. The (0002) RC-FWHM values of the sputtered layers before annealing are similar to the ELO template, i.e. between 110 arcsec and 140 arcsec. This means that the sputtered AlN grains are aligned to each other before the HTA without a large tilt in the c -direction. Nevertheless, the tilt component of the sputtered AlN is reduced after HTA (schematically shown in Fig. 2.6(a)), as indicated by a smaller (0002) RC-FWHM in Fig. 2.5(a). The $(10\bar{1}2)$ RC-FWHM of the sputtered AlN layers prior to HTA is more than 2400 arcsec (Fig. 2.5(b)). Consequently, the sputtered AlN grains show a much higher twist component of the lattice planes compared to ELO, which has a $(10\bar{1}2)$ RC-FWHM value of 320 arcsec. By annealing the sputtered AlN layers and overgrowing with 400-nm AlN by MOVPE, the $(10\bar{1}2)$ RC-FWHM is significantly reduced to 440 arcsec for the 150-nm sputtered AlN and 240 arcsec

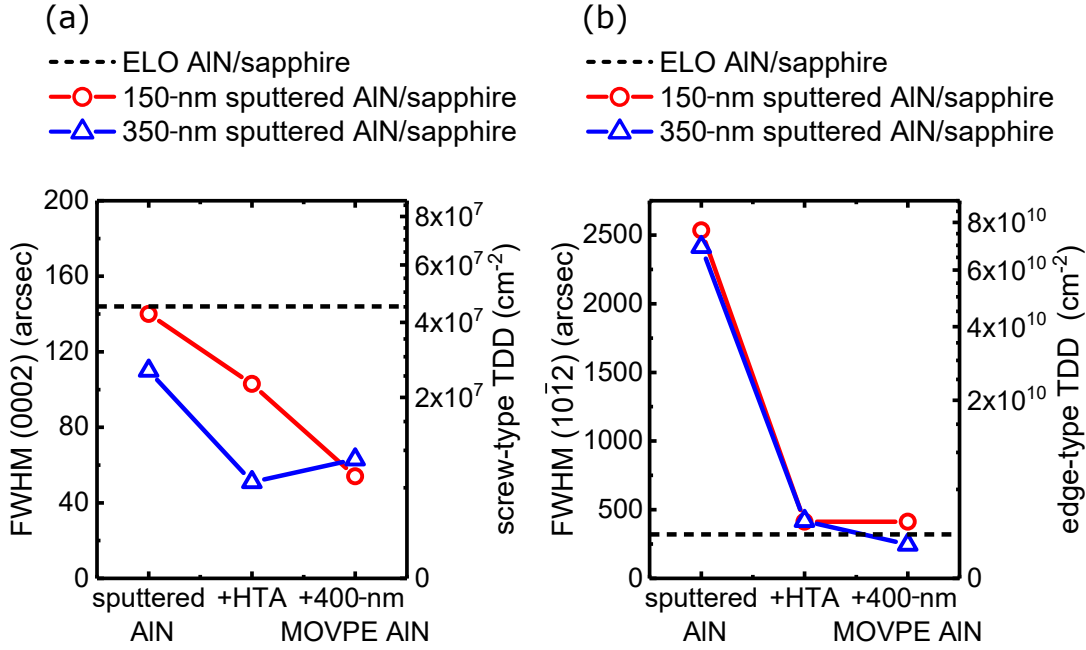


Figure 2.5: HRXRD RC-FWHM of the (a) symmetric (0002) and (b) asymmetric (10 $\bar{1}2$) reflection as well as the estimated screw- and edge-type dislocation density of ELO AlN and of sputtered AlN templates before HTA, after HTA and after overgrowth with 400-nm MOVPE AlN. Measurements performed by S. Hagedorn, FBH.

for the 350-nm sputtered AlN. This value is similar to the one of the ELO AlN template and indicates an improved crystal quality for the sputtered AlN layers by HTA. The decrease in the twist component (schematically shown in Fig. 2.6(b)) in sputtered layers by HTA is in good agreement with the results of Miyake et al. [70].

The TDDs determined from the measured RC-FWHM (calculations according to the references [76] and [77]) are $1.1 \times 10^9 \text{ cm}^{-2}$ for the ELO AlN, $2.0 \times 10^9 \text{ cm}^{-2}$ for the MOVPE-overgrown 150-nm SP-HTA AlN and $7.2 \times 10^8 \text{ cm}^{-2}$ for the MOVPE-overgrown 350-nm SP-HTA AlN. It is worth noting here that due to the large X-ray spot size the estimated TDDs of the ELO templates include both the reduced TDD region above the ELO trenches and the higher TDD region above the ELO ridges. Due to the lower RC-FWHM of the (0002) reflection, the screw-type dislocation density of the 150-nm SP-HTA AlN ($6.3 \times 10^6 \text{ cm}^{-2}$) and 350-nm SP-HTA AlN ($8.6 \times 10^6 \text{ cm}^{-2}$) is lower compared to the ELO AlN ($4.4 \times 10^7 \text{ cm}^{-2}$). It should also be noted that the (10 $\bar{1}2$) RC-FWHMs were similar after annealing for both thicknesses of the SP-HTA AlN templates, but only the (10 $\bar{1}2$) RC-FWHM value of the 350-nm sputtered AlN/sapphire template was reduced after the MOVPE overgrowth. The 350-nm SP-HTA AlN before MOVPE overgrowth was slightly rougher than the 150-nm SP-HTA AlN, which

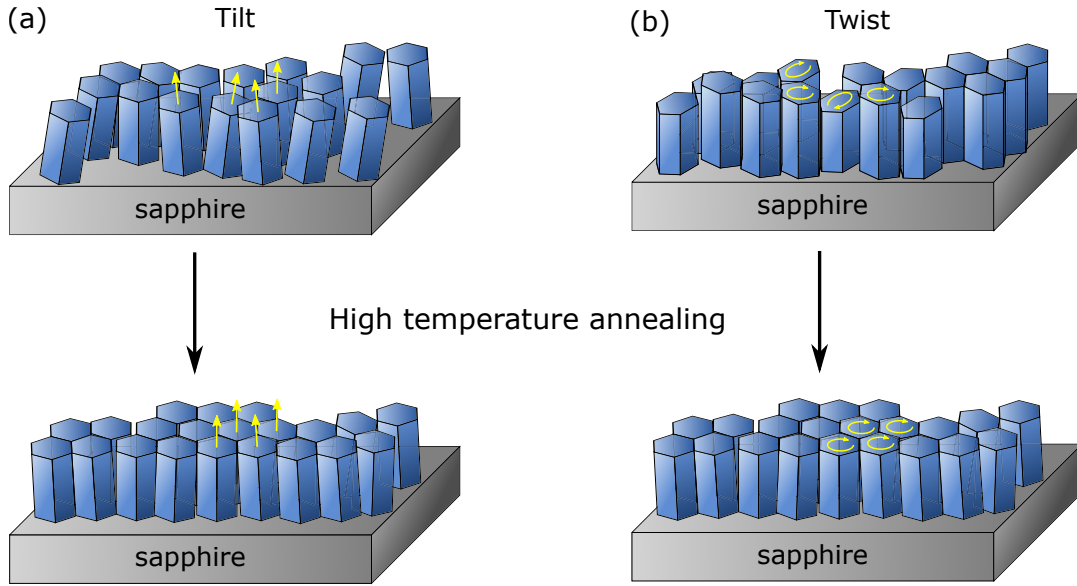


Figure 2.6: Illustration of the sputtered AlN layers before and after HTA.

could lead to enhanced annihilation of dislocations due to dislocation bending. However, this behavior was not observed for the (0002) RC-FWHMs and requires further investigation.

The curvatures of the templates were measured with a Laytec Epi-Curve-TT curvature sensor, which directs two parallel laser beams onto the sample surface and detects the distance between the two reflected beams. The ELO AlN template show a convex curvature of -160 km^{-1} . As expected, the 150-nm and 350-nm SP-HTA AlN templates show a lower convex curvature of -80 km^{-1} after overgrowth with 400-nm AlN by MOVPE. The lower convex curvature of the SP-HTA AlN templates is mainly caused by the smaller layer thickness compared to the ELO AlN template, which is beneficial for the microfabrication process as previously discussed.

2.2.2 Dislocation density and RRE of AlGaIn MQWs

In order to qualify the SP-HTA AlN templates as device substrates, the structural properties and luminescence characteristics of the overgrown AlGaIn-based MQWs emitting at 265 nm are investigated. Figure 2.7 shows the surface morphology of the MQW samples on the different AlN/sapphire templates recorded by AFM. In contrast to the 2D step-flow growth of the AlN/sapphire templates, the surfaces of the MQW heterostructures are spiral-growth dominated (see inset in Fig. 2.7(a)). This surface morphology is consistent with other

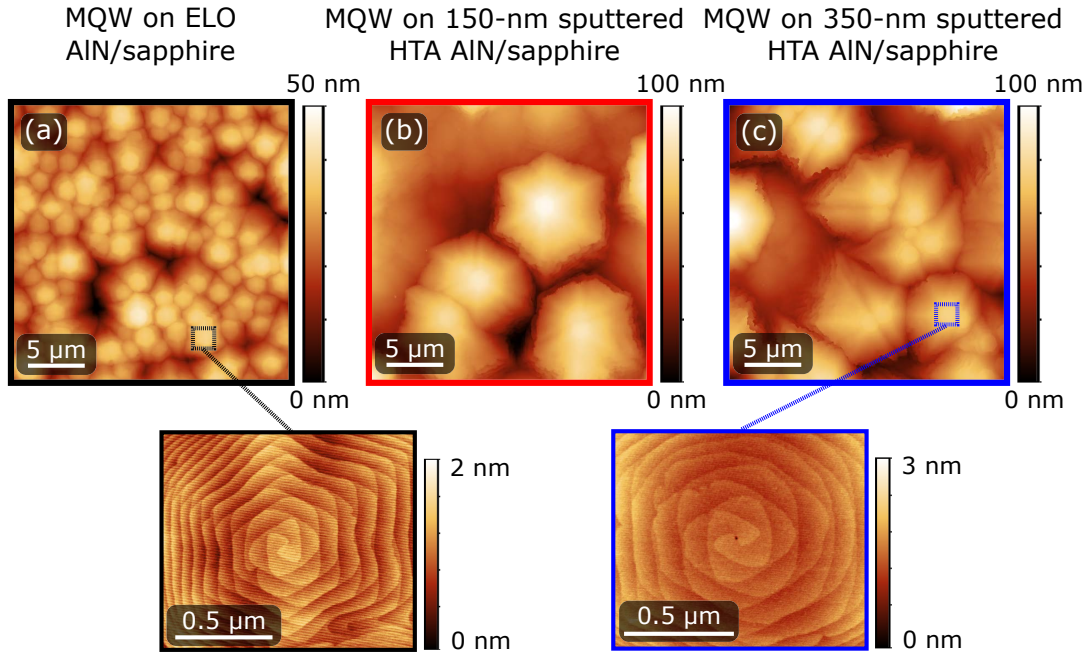


Figure 2.7: Surface morphology of the MQW heterostructure measured with AFM on (a) ELO AlN (b) 150-nm-thick SP-HTA AlN and (c) 350-nm-thick SP-HTA AlN.

publications [78–80] and indicates a dislocation with a screw component in the hillock cores that causes spiral growth [81]. The hillock densities were estimated from the AFM topograms to be $2 \times 10^7 \text{ cm}^{-2}$ for the MQW sample on the ELO AlN template and below $3 \times 10^6 \text{ cm}^{-2}$ for the MQW samples on the SP-HTA AlN templates. The difference in hillock density results from the differences in dislocation densities with a screw component between the ELO AlN template and the SP-HTA templates consistent with the lower RC-FWHM of the (0002) reflection of the SP-HTA templates. It should be noted that due to the lower hillock density of the MQW samples on the SP-HTA templates, the diameter and height of the hillocks also increases as the slope of the hillocks remains constant. The diameter and height of the hillocks increases from $\sim 3 \mu\text{m}$ and $\sim 12 \text{ nm}$ to $\sim 13 \mu\text{m}$ and $\sim 60 \text{ nm}$ for the MQW heterostructures grown on the ELO AlN template and on SP-HTA AlN templates, respectively.

In order to investigate the luminescence characteristics, panchromatic CL measurements of the AlGaIn-based MQWs grown on the AlN/sapphire templates were performed. Figure 2.8 shows the CL intensity maps with two different magnifications and the corresponding SEM images at the same position on the sample. Shojiki et al. [78] reported only a low dark spot contrast at 300 K as well as 20 K in MQW samples grown on SP-HTA AlN, which was attributed to a large number of point defects. However, if the density of the point defects

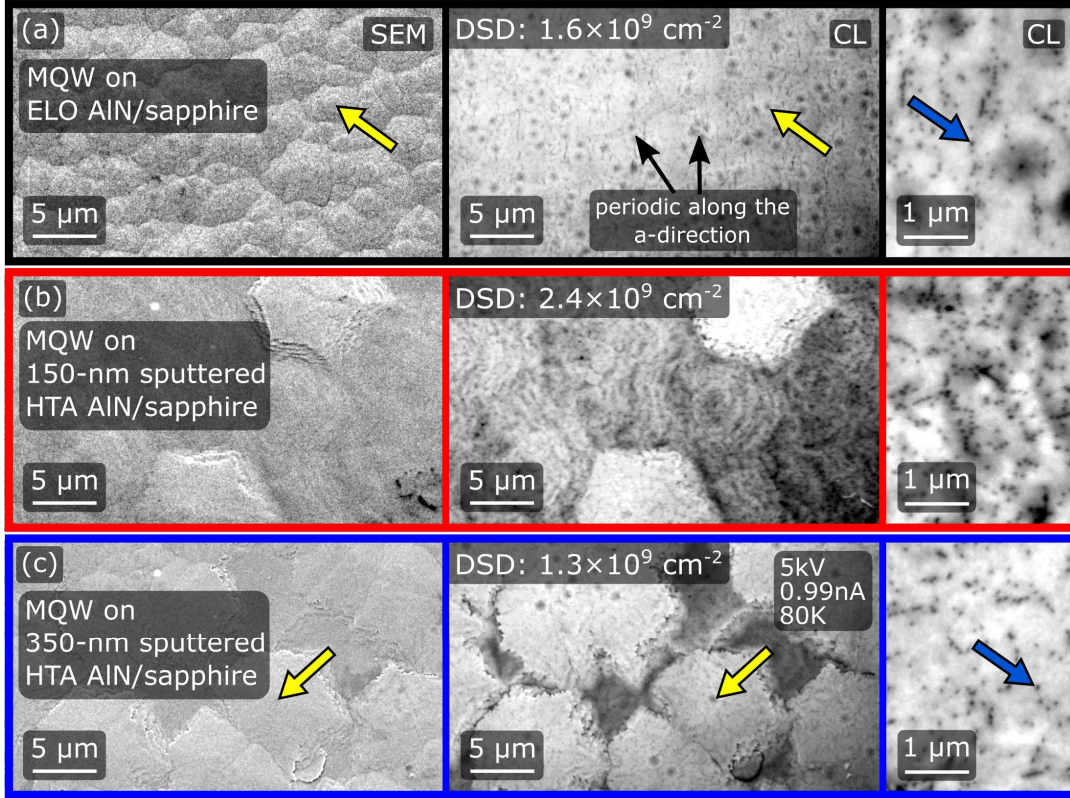


Figure 2.8: SEM images (left) and panchromatic CL intensity maps (center and right) of the MQW heterostructure on (a) ELO AlN (b) 150-nm SP-HTA AlN and (c) 350-nm SP-HTA AlN. The images were recorded at a temperature of 80 K. Measurements performed by U. Zeimer, FBH.

is sufficiently low, the excited carriers diffuse into the surrounding threading dislocations that appear as dark spots in CL intensity maps. Consequently, the dark spot contrast resulting from the threading dislocations increases with decreasing point defect density. To enable a higher dark spot contrast, the panchromatic CL intensity maps were recorded at 80 K to increase the diffusion length due to the thermal inactivation of point defects. In all MQW samples, a clear dark spot contrast is observed, originating from threading dislocations. Accordingly, it can be assumed that the threading dislocations are the dominant non-radiative recombination centers at 80 K for all MQW samples under investigation [78]. Two types of dark spots can be observed in these images: Large dark spots centered on hillock cores (marked with yellow arrows in Fig. 2.8) and small dark spots in the background (marked with blue arrows in Fig. 2.8). The number of small dark spots is higher (10^9 cm^{-2}) than the large ones and is most likely attributed to edge-type dislocations [79]. Due to the voids formed in the ELO process, the dark spots in the ELO AlN template are periodic along the a -direction. Furthermore, by comparing the CL and SEM images, a

clear correlation of the large dark spots and the hillock cores can be seen, as indicated with yellow arrows in Fig. 2.8. A similar correlation was published by Kusch et al. [79] for $\text{Al}_{0.8}\text{Ga}_{0.2}\text{N}:\text{Si}$ layers. They observed a threading dislocation with a screw component located at the core of each hillock, which is consistent with the observed growth spirals in Fig. 2.7. In contrast to the edge-type dislocations, they found an increased incorporation of point defects, such as oxygen, around the screw-type dislocations, which could introduce deep level states in the bandgap and reduce the CL intensity in the vicinity of the screw-type dislocations. Furthermore, the different morphology of the hillock cores could lead to a variation in the growth of the AlGa_N-based MQW active region, leading to a local change in the CL intensity. Note that even though the density of the large dark spots of the MQW sample grown on the ELO AlN ($3 \times 10^7 \text{ cm}^{-2}$) is higher than the one of the MQW sample grown on the SP-HTA AlN templates ($\leq 3 \times 10^6 \text{ cm}^{-2}$), this value is small compared to the total dark spot density, i.e. $1.6 \times 10^9 \text{ cm}^{-2}$, $2.4 \times 10^9 \text{ cm}^{-2}$ and $1.3 \times 10^9 \text{ cm}^{-2}$ on ELO AlN, on 150-nm SP-HTA AlN and on 350-nm SP-HTA AlN, respectively. The total dark spot density of the ELO AlN template includes both the reduced TDD region above the ELO trenches (dark spot density: $1.1 \times 10^9 \text{ cm}^{-2}$) and the higher TDD region above the ELO ridges (dark spot density: $2.1 \times 10^9 \text{ cm}^{-2}$). The trend of the total TDD as well as the higher screw-type dislocation density on the ELO AlN template are in agreement with the HRXRD investigations. Nevertheless, the TDD estimated by HRXRD is slightly lower compared to the dark spot density, indicating that XRD might underestimate the dislocation density, since the dark spot density corresponds in principle to a lower limit if each dark spot is related to at least one dislocation. Note that TEM studies on similar samples (see section 2.3.1 for further details) show no evidence of additional threading dislocations introduced during the growth of the AlGa_N heterostructure.

To further investigate the non-radiative recombination, temperature and excitation power dependent PL spectroscopy (5 K - 300 K, 0.3 kW/cm^2 - 1170 kW/cm^2) using an ArF*-excimer laser (193 nm excitation wavelength) was performed. Figure 2.9(a) shows the PL spectra of the MQW heterostructures at 5 K grown on 150-nm-thick SP-HTA AlN in red, 350-nm-thick SP-HTA AlN in blue and ELO AlN in black. The differences in the PL intensity in Fig. 2.9(a) are most likely attributed to small alignment errors. The MQW samples show PL peaks at around 4.70 eV and at 4.97 eV. The emission energies are in good agreement with

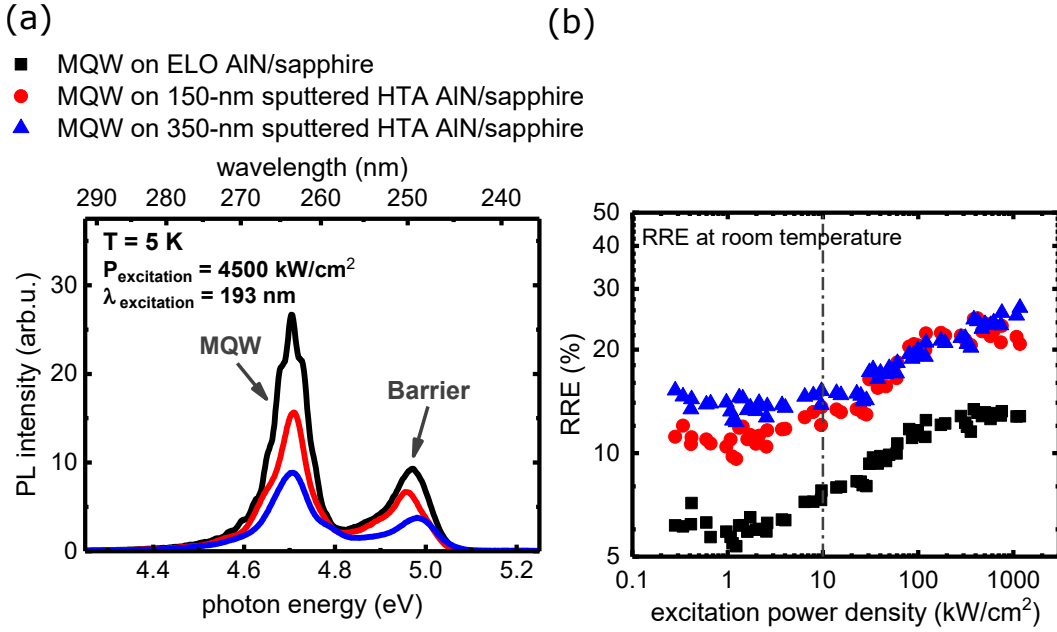


Figure 2.9: (a) PL spectra of the MQW heterostructure at 5 K on ELO AlN (black), 150-nm SP-HTA AlN (red) and 350-nm SP-HTA AlN (blue). (b) Estimated RRE as a function of the excitation power density. Measurements performed by C. Reich, TUB.

the estimated bandgap energies of $\text{Al}_{0.48}\text{Ga}_{0.52}\text{N}$ for the MQWs and $\text{Al}_{0.62}\text{Ga}_{0.38}\text{N}$ for the barriers. The PL RRE in Fig. 2.9(b) is roughly estimated from the temperature dependence and from the excitation power dependence of the integrated PL intensity assuming no Shockley-Read-Hall recombination at 5 K [66]. For excitation power densities below 30 kW/cm^2 , the MQW heterostructures on the 350-nm SP-HTA AlN template shows a slightly higher RRE than the MQW sample on 150-nm SP-HTA AlN, which can be attributed to the lower TDD. However, the difference in the RRE might be in the range of measurement accuracy, as discussed below. The estimated RRE of the MQW heterostructures at an excitation power of 10 kW/cm^2 is 8%, 12% and 15% on ELO AlN, 150-nm-thick SP-HTA AlN and 350-nm-thick SP-HTA AlN, respectively. The lower RRE of the MQW sample on the ELO AlN template is unexpected since the TDD estimated from the RC-FWHM and panchromatic CL is similar to the one on the 350-nm-thick SP-HTA AlN template. A possible explanation for the lower RRE of the MQW heterostructure grown on the ELO AlN template might be the higher density of screw-type dislocations appearing as large dark spots in the panchromatic CL intensity maps (see yellow arrows in Fig. 2.8). Although the screw-type dislocation density is low compared to the edge-type dislocation density, the larger size of the dark spot could affect the RRE.

It should be mentioned that the combination of temperature and excitation

power density dependent PL measurements, while assuming 100% RRE at low temperatures, is frequently cited in the literature for the estimation of the RRE [78, 82–84]. Nevertheless, for a correct estimation, many factors need to be taken into account such as excitons [85], Auger recombination [86] and saturation of non-radiative recombination centers [85]. Furthermore, in non-resonant PL investigations (as in the case discussed in this chapter), it is assumed that a carrier transfer into the MQW from the surrounding (e.g. the barriers) affects the RRE estimation [78, 86] as reported in the InGaN-based systems [87, 88]. Accordingly, the determination of the RRE by the PL evaluation is associated with large uncertainties. However, it is assumed that the accuracy could be sufficient to estimate a trend and make qualitative conclusions.

2.2.3 Emission power and EQE of UVC-LEDs

As discussed in the previous section, an accurate determination of the RRE by non-resonant PL is difficult to achieve and the results should only be considered qualitatively. However, the findings suggest at least a similar crystal quality and RRE between the MQWs grown on SP-HTA AlN and ELO AlN.

To investigate the electro-optical properties, UVC-LEDs were grown and processed on SP-HTA AlN templates and on ELO AlN templates in the same growth and process run. The light output power and EL spectra of the UVC-LEDs were measured on-wafer through the backside of the sapphire substrate by a calibrated large-area silicon photodiode and a compact UV-VIS StellarNeT EPP 2000 spectrometer, respectively. Figure 2.10 shows (a) the EL spectra at 20 mA as well as (b) the current-voltage and output power characteristics in continuous wave (cw) operation for the UVC-LEDs grown on ELO AlN, 150-nm SP-HTA AlN and 350-nm SP-HTA AlN. The EL spectra exhibit a single peak emission at a wavelength of 268 nm at 20 mA without indication of parasitic luminescence within the measured range up to 900 nm and within three orders of magnitude dynamic range. At an operating current of 20 mA, an output power of 0.72 mW, 0.65 mW and 0.70 mW at an operating voltage of 7.6 V, 7.1 V and 6.9 V is obtained for UVC-LEDs grown on ELO AlN, 150-nm SP-HTA AlN and 350-nm SP-HTA AlN, respectively. The slightly higher operating voltage for the ELO AlN template is likely ascribed to the process accuracy and reproducibility. The output powers at 20 mA correspond to EQEs of 0.78%, 0.70% and 0.75%, respectively. Note that this trend is valid within the whole measured range, as shown in Fig. 2.10(b). Even though, as it was shown in the previous section, the

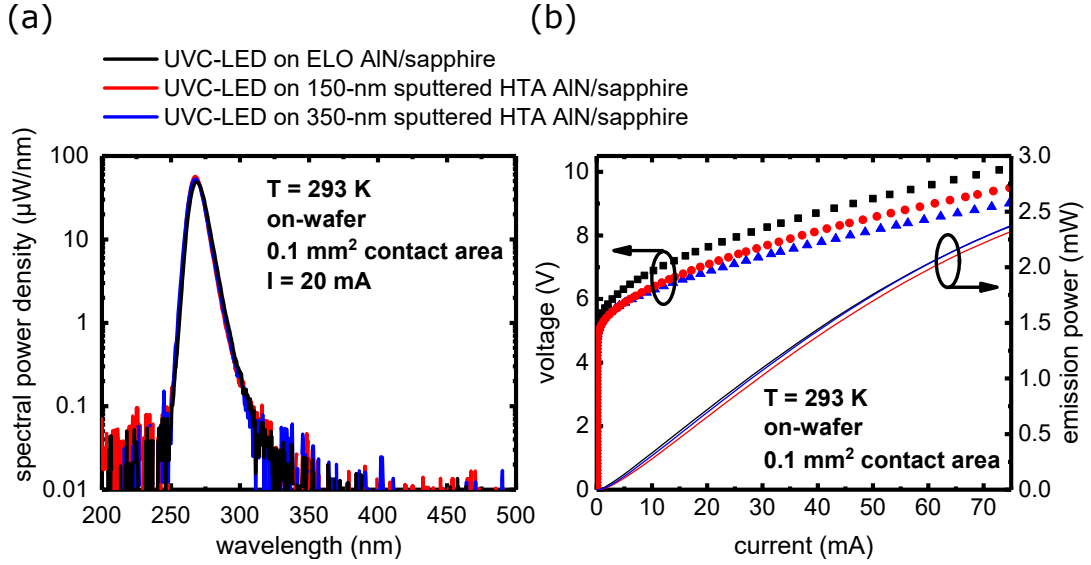


Figure 2.10: (a) Representative emission spectra at 20 mA and (b) LIV curves of UVC-LEDs grown on ELO AlN, 150-nm SP-HTA AlN and 350-nm SP-HTA AlN.

150-nm SP-HTA AlN has a higher ($10\bar{1}2$) RC-FWHM of the AlN reflection and a higher dark spot density of the MQW sample, the output powers are similar and consistent with the PL investigations.

Since ELO AlN templates includes a patterned sapphire, an increase in the LEE is expected due to the reduced light losses by total reflection at the AlN-sapphire interface followed by absorption in the AlGaN quantum wells, in the p -side and in the contacts [89–91]. In order to ensure a proper comparison, Monte Carlo ray-tracing simulations were performed. The roughness of the sapphire substrates was measured by AFM and implemented in the simulation. The degree of optical polarization $P = (TE - TM)/(TE + TM)$ (ratio between transversal magnetic TM and transversal electric TE polarization) of the EL emission [92] was determined by in-plane emission from cleaved facets (perpendicular to the ELO voids) to 0.76 (UVC-LED on ELO AlN template) and to 0.86 (UVC-LED on SP-HTA AlN template)⁵. Nevertheless, it is expected that the degree of polarization of the UVC-LEDs on the ELO AlN templates is underestimated due to light scattering at the ELO voids [91]. Thus, the ray-tracing simulations assume a 10% higher degree of polarization of the UVC-LEDs on the ELO AlN templates. The higher degree of polarization of the UVC-LED on the SP-HTA AlN templates is likely attributed to the higher compressive strain. The higher compressive strain of the UVC-LED on the SP-HTA AlN templates was

⁵Ray-tracing simulations and measurements of the optical polarization were performed by M. Guttman, TUB.

measured by HRXRD and is in accordance with references [70, 71, 93]. Various publications have reported how compressive strain in the growth plane enhances TE-polarized light and increases the degree of polarization [92, 94, 95]. The on-wafer LEE of the UVC-LEDs were estimated to 3.4% from the epitaxial side of the planar HTA template and to 3.9% from the epitaxial side of the ELO template. Consequently, the simulations show an enhancement of 15% in the LEE due to the striped patterned ELO voids at the AlN-sapphire interface.

Although the LEE of the UVC-LED on the ELO AlN template is higher compared to the UVC-LED on the planar SP-HTA AlN templates, the output power and EQE are similar as shown in Fig. 2.10. These results indicate a higher (or at least similar) RRE of the UVC-LEDs on the SP-HTA AlN templates, which is consistent with the PL investigations. However, note that the calculated IQEs of 20% (ELO AlN, 150-nm SP-HTA AlN) and 22% (350-nm SP-HTA AlN) derived from the EL-EQEs and the simulated LEEs do not agree with the RRE estimated by PL. The smaller RRE might be sufficiently explained by the high uncertainty of the non-resonant PL evaluation, as already discussed.

2.2.4 Summary and conclusion

In this section, the applicability of relatively thin (≤ 750 nm) low-cost sputtered and HTA-based AlN/sapphire templates as an alternative to thick (~ 6 μm) and relatively expensive ELO AlN/sapphire templates was investigated. The structural and electro-optical properties of AlGaN-based MQW heterostructures and UVC-LEDs on 150-nm and 350-nm SP-HTA AlN/sapphire templates were discussed and compared with the growth on ELO AlN templates. After HTA of the 350-nm sputtered AlN, the RC-FWHM of the (0002) and (10 $\bar{1}$ 2) reflections of the HRXRD rocking curves decreased drastically to 65 arcsec and 240 arcsec, respectively. CL measurements reveal dark spot densities of $1.6 \times 10^9 \text{ cm}^{-2}$, $2.4 \times 10^9 \text{ cm}^{-2}$ and $1.3 \times 10^9 \text{ cm}^{-2}$ in MQW samples grown on ELO AlN, 150-nm SP-HTA AlN, 350-nm SP-HTA AlN, respectively. The UVC-LEDs on ELO AlN and the SP-HTA AlN exhibit similar output powers of 0.7 mW (measured on-wafer at 20 mA). However, ray-tracing simulations were performed to ensure a fair comparison of the EQE between ELO and SP-HTA AlN templates. The simulations showed a 15% increase in the LEE due to the striped patterned ELO voids, which could indicate a higher RRE of the SP-HTA AlN templates. The results show how SP-HTA AlN templates allow for the fabrication of efficient UVC-LEDs without any optical output power losses compared to ELO templates.

This approach can reduce fabrication complexity and the cost for UVC-LEDs.

2.3 UVC-LEDs on HTA ELO AlN/sapphire

In the previous section, the beneficial effect of HTA on the crystal quality of AlN layers as well as on the MQW heterostructure and on the performance of UVC-LEDs was presented by comparing the results with AlGaIn-based heterostructures grown on ELO AlN templates. In this section, the combined beneficial effects of HTA and of a patterned AlN-sapphire interface on the crystal quality and on performance characteristics of AlGaIn-based MQW heterostructures and UVC-LEDs emitting at 265 nm will be investigated.

The HTA ELO AlN templates were fabricated similar to the ELO template (see section 2.1). In this case, the first 500-nm AlN film was face-to-face annealed at 1700 °C in N₂ ambient before patterning. In order to distinguish between effects of HTA and of a patterned AlN-sapphire interface, a HTA planar AlN/sapphire and an ELO AlN/sapphire templates were prepared. All templates in this section were produced using MOVPE growth only. Subsequently, MQW heterostructures and UVC-LEDs were grown simultaneously on the different AlN/sapphire templates. The heterostructures are shown schematically in Fig. 2.11. The slightly different heterostructures, compared to the

(a) MQW heterostructure

(b) UVC-LED heterostructure

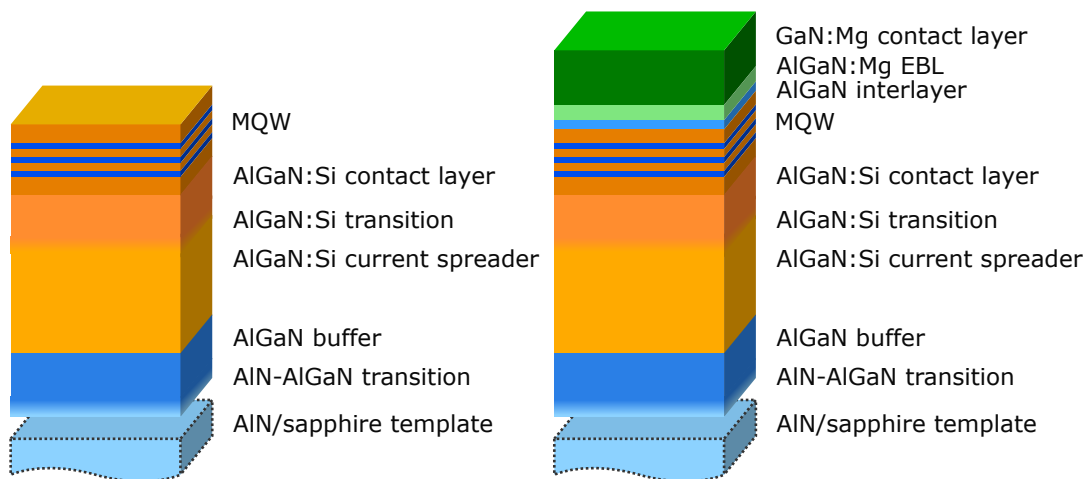


Figure 2.11: Schematic of the (a) MQW heterostructure and (b) UVC-LED heterostructure grown on the ELO AlN/sapphire, MOVPE HTA planar AlN/sapphire and HTA ELO AlN/sapphire templates.

last section, were used mainly to reduce the operating voltages and enable higher WPEs for the flip-chip UVC-LEDs (see section 3). The UVC-LED heterostructure consists of a 600-nm-thick homoepitaxial AlN buffer layer, a 25-nm-thick transition layer, a 100-nm-thick $\text{Al}_{0.76}\text{Ga}_{0.24}\text{N}$ buffer, a 900-nm-thick $\text{Al}_{0.76}\text{Ga}_{0.24}\text{N}:\text{Si}$ current spreader, a 100-nm-thick AlGaN:Si transition layer and a 200-nm-thick $\text{Al}_{0.65}\text{Ga}_{0.35}\text{N}:\text{Si}$ contact layer. The active region contains a three-fold $\text{Al}_{0.62}\text{Ga}_{0.38}\text{N}/\text{Al}_{0.48}\text{Ga}_{0.52}\text{N}$ MQW followed by a 10-nm-thick $\text{Al}_{0.85}\text{Ga}_{0.15}\text{N}$ interlayer, a 25-nm-thick $\text{Al}_{0.75}\text{Ga}_{0.25}\text{N}:\text{Mg}$ electron blocking layer (EBL), and a 200-nm-thick GaN:Mg contact layer. The MQW heterostructure is identical except for the omission of the p -layers (Fig. 2.11(a)).

Before the AlGaN growth, the TDDs were estimated by the RC-FWHM to be $1.5 \times 10^9 \text{ cm}^{-2}$ (screw-type dislocation: $5.0 \times 10^7 \text{ cm}^{-2}$) for the ELO AlN, $0.8 \times 10^9 \text{ cm}^{-2}$ (screw-type dislocation: $0.9 \times 10^7 \text{ cm}^{-2}$) for the HTA planar AlN and $0.8 \times 10^9 \text{ cm}^{-2}$ (screw-type dislocation: $4.5 \times 10^7 \text{ cm}^{-2}$) for the HTA ELO AlN. As mentioned before, the estimated TDDs of the ELO templates include both the reduced TDD region above the ELO trenches and the region above the ELO ridges. It should be noted that a significant reduction in the estimated TDD of the HTA AlN template is not observed despite of the ELO process. However, the RC-FWHMs indicate an improved crystal quality of the ELO AlN template after thermal annealing of the AlN seed layer.

2.3.1 Improved dislocation density and REE of AlGaN MQWs

In order to investigate the crystal quality and emission behavior of an active region on HTA ELO AlN, MQW heterostructures emitting around 265 nm were grown simultaneously on the different AlN/sapphire templates by MOVPE. Figure 2.12 shows the surface morphology of the MQW samples recorded by AFM on (a) ELO AlN, (b) HTA planar AlN and (c) HTA ELO AlN. Similar to section 2.2.2, the AFM topograms reveal a surface morphology dominated by hillocks, typical for AlGaN growth on AlN/sapphire templates. However, compared to the MQW heterostructures grown on the SP-HTA AlN templates, the hillock density on the MOVPE-grown HTA AlN template is higher, indicating a higher screw-type dislocation density. Similarly, in the CL topograms (Fig. 2.13), two types of dark spots can be observed: Large dark spots (marked with yellow arrows in Fig. 2.13), centered on hillock cores and small dark spots (marked

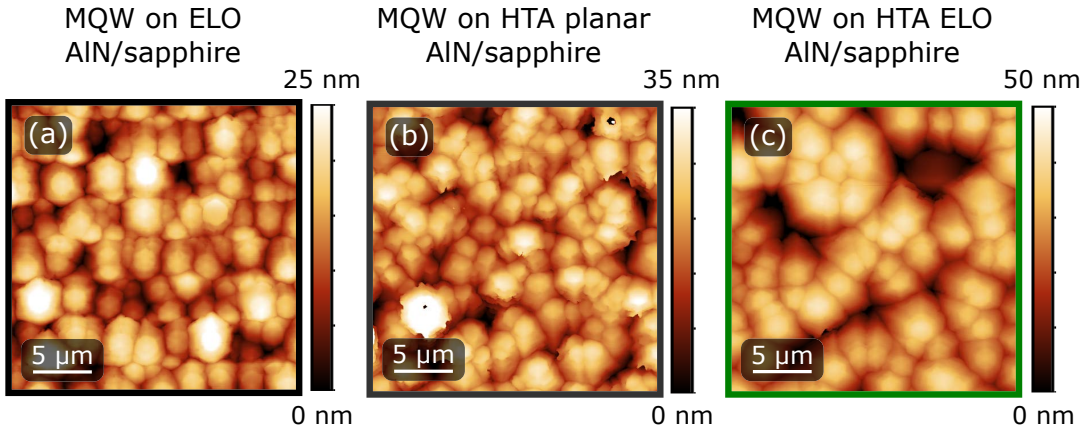


Figure 2.12: Surface morphology of the MQW heterostructure measured with AFM on (a) ELO AlN (b) HTA planar AlN and (c) HTA ELO AlN. Measurements performed together with E. Ziffer, TUB.

with blue arrows in Fig. 2.13), in the background. As discussed previously, the large dark spots are mainly associated with screw-type dislocations and the small dark spots with edge-type dislocations. The MQW samples exhibit a total dark spot density of $1.4 \times 10^9 \text{ cm}^{-2}$ (ELO), $1.1 \times 10^9 \text{ cm}^{-2}$ (HTA planar) and $0.9 \times 10^9 \text{ cm}^{-2}$ (HTA ELO), whose $2.5 \times 10^7 \text{ cm}^{-2}$ (ELO), $1.8 \times 10^7 \text{ cm}^{-2}$ (HTA planar) and $1.2 \times 10^9 \text{ cm}^{-2}$ (HTA ELO) correspond to the density of the large dark spots. These values show the same trend as the TDDs estimated by HRXRD. However, in the case of the HTA AlN template, the screw-type dislocation density estimated by HRXRD is lower, indicating that XRD may underestimate the screw-type dislocation density as in principle the hillock density (or the large dark spot density) corresponds to a lower limit if each hillock core is linked to at least one dislocation. The dark spots are uniformly distributed for all samples, except for the MQW heterostructure on the ELO AlN template, which exhibits regions of higher ($1.8 \times 10^9 \text{ cm}^{-2}$) and lower ($1.0 \times 10^9 \text{ cm}^{-2}$) density of the dark spots, caused by a variation of the TDD induced by the patterned ELO process. This effect cannot be clearly identified on the HTA ELO, most likely because of the already low TDD of the HTA layer before overgrowth, which reduces the dark spot density contrast between the regions above the ELO trenches and ridges. Note that the density of the large dark spots as well the hillock density of the HTA-based templates grown by MOVPE is higher compared to the SP-HTA AlN templates. An observation that requires further investigation.

In order to characterize the TDD in more detail, the MQW heterostructures were prepared for cross-sectional TEM using standard thinning techniques. Figure 2.14 shows the cross-sectional TEM images recorded under two different

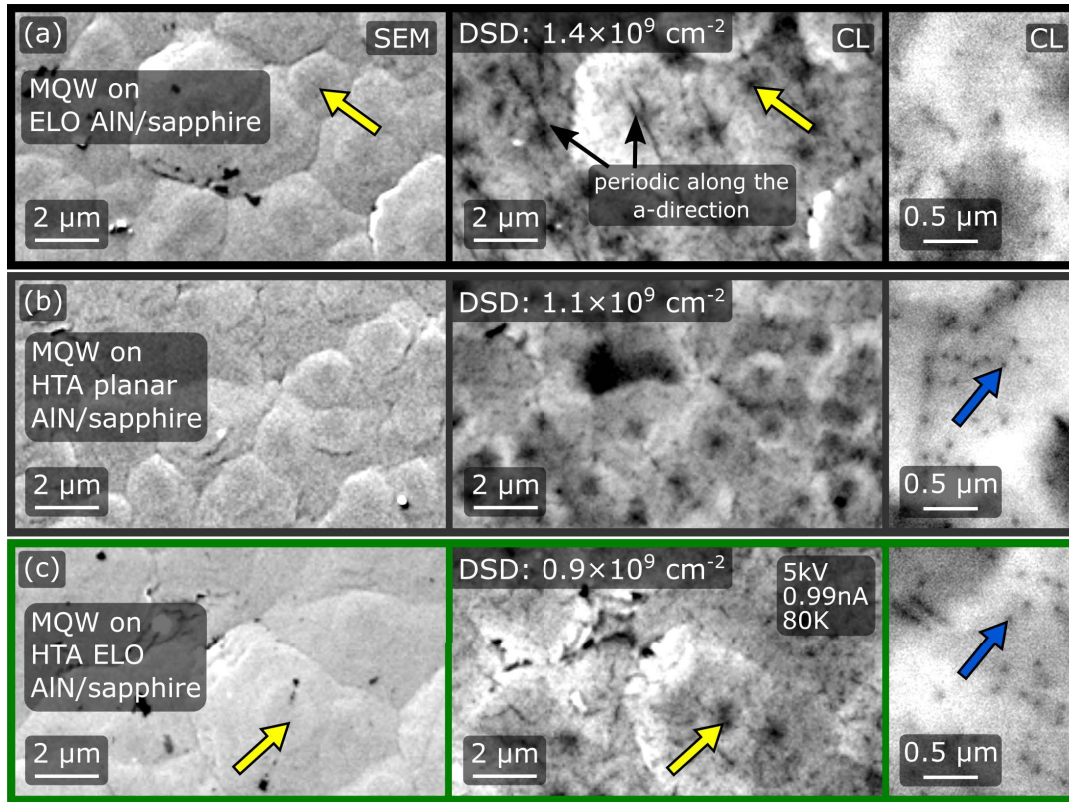


Figure 2.13: SEM images (left) and panchromatic CL intensity maps (center and right) of the MQW heterostructure on (a) ELO AlN (b) HTA planar AlN and (c) HTA ELO AlN. The images were recorded at a temperature of 80 K. Measurements performed by C. Netzel, TUB.

and orthogonal two-beam diffraction conditions with $\vec{g} = \langle 0002 \rangle$ and $\vec{g} = \langle 11\bar{2}0 \rangle$. Because of the different contrast of the same threading dislocation type in the two diffraction conditions (proportional to $\vec{g} \cdot \vec{b}$, where \vec{b} is the Burgers vector of the associated dislocation), threading dislocations with a c -component in their Burgers vector (usually screw-type with $b = \langle 0001 \rangle$, or with mixed screw/edge character) are visible with $\vec{g} = \langle 0002 \rangle$, and threading dislocations with an a -component in their Burgers vector (usually edge-type with $b = 1/3 \langle 1\bar{2}10 \rangle$ or mixed) are observable with $\vec{g} = \langle 11\bar{2}0 \rangle$. The ELO growth with and without HTA treatment is similar and form almost identical ELO voids, i.e. a similar LEE is expected. In the first 500-nm MOVPE-grown AlN of the MQW sample on ELO AlN (Fig. 2.14(a)(b)), a defect rich layer is observed with most of the threading dislocations occurring near the AlN-sapphire interface (see enlargement in Fig. 2.14(a)). The large number of dislocations in this region is difficult to resolve individually, thus preventing a reliable estimation of the TDD. Nevertheless, the TDD is strongly reduced above the ELO voids and a further TDD reduction is achieved by dislocation annihilation when the AlN

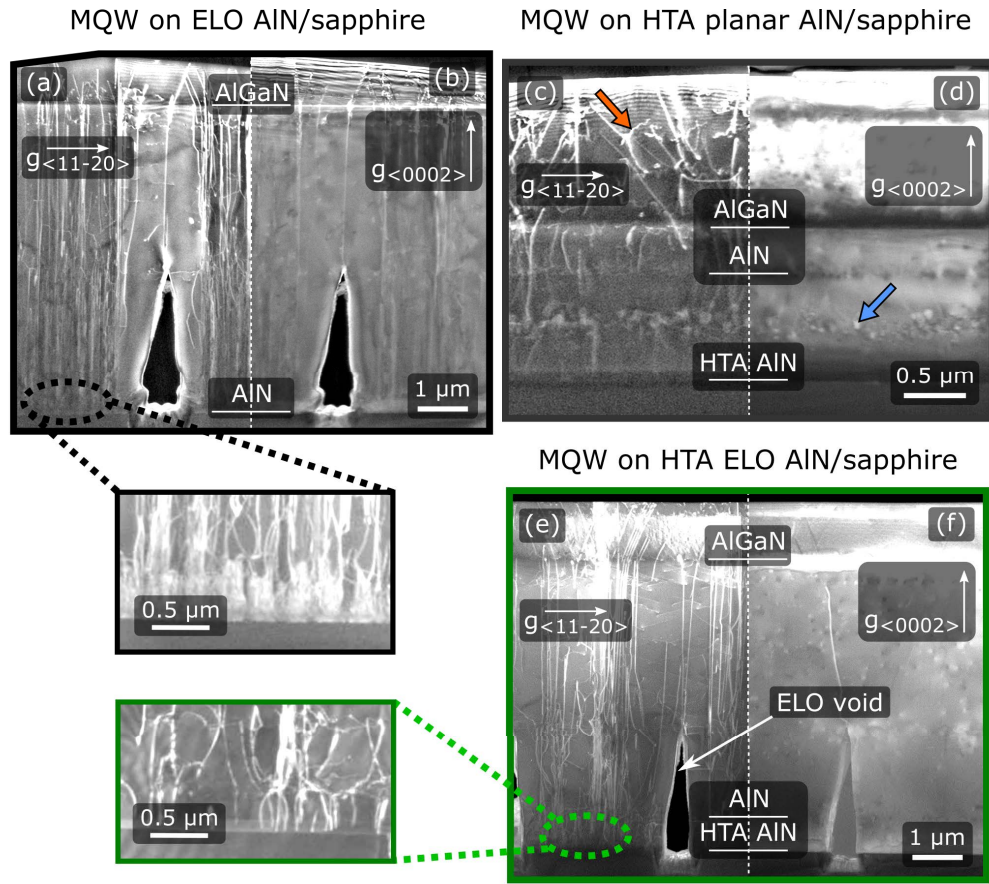


Figure 2.14: Cross-sectional TEM diffraction contrast micrographs of the MQW heterostructures on (a)(b) ELO AlN, (c)(d) HTA AlN and (e)(f) HTA ELO under different diffraction contrast conditions (a)(c)(e) $\vec{g} = \langle 11\bar{2}0 \rangle$ and (b)(d)(f) $\vec{g} = \langle 0002 \rangle$. Note the different scaling of (c)(d) compared to (a)(b) and (e)(f). Measurements performed by L. Cancellara, IKZ.

thickness is increased. At the interface between the AlN and AlGaN layers (in all templates under investigation), the straight dislocation lines begin to bend slightly in relation to the c -axis (measured between $20^\circ - 24^\circ$), which is most probably caused by the different strain state in the layers. These projected angles of inclination are consistent with those observed by Mogilatenko et al. [96] at the interface between ELO AlN and $\text{Al}_{0.80}\text{Ga}_{0.20}\text{N}$ and inclined in the $\langle 1\bar{1}00 \rangle$ (m-AlN) direction. Curved dislocation line segments identified as dislocation loops (orange arrow) are observed at random positions within the $\text{Al}_{0.76}\text{Ga}_{0.24}\text{N}:\text{Si}$ current spreading layer. This type of dislocation will be discussed in more detail in chapter 3. Approximately 300 nm above the sapphire, voids with a diameter of about (10 - 50) nm are observed both in the HTA planar AlN and in the HTA ELO AlN template (blue arrow in Fig. 2.14(d)). The voids may be a result of agglomeration of voids or oxygen precipitation in the cooling phase following the

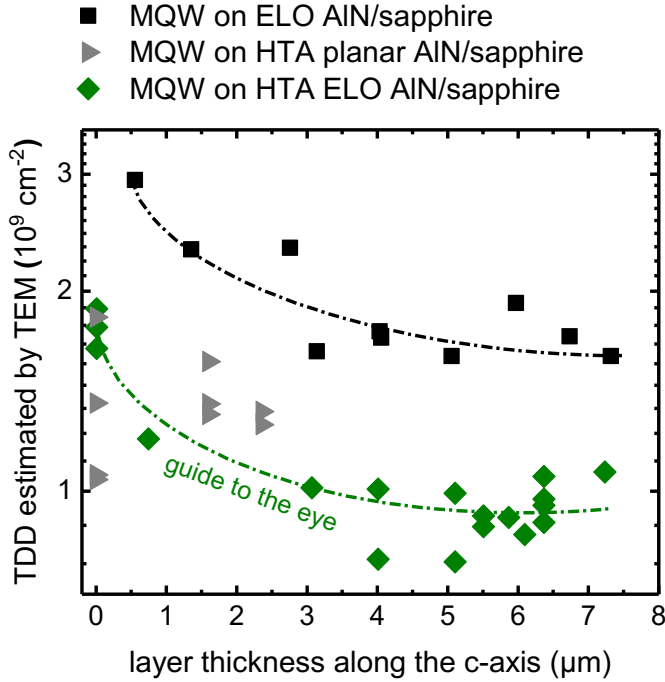


Figure 2.15: Depth distribution of the total TDD of MQW heterostructures on ELO AlN, HTA planar AlN and HTA ELO AlN estimated by cross-sectional TEM. A layer thickness of 0 nm corresponds to the AlN/sapphire interface and 7.2 μm to the AlGaN-based MQW active region. Measurements performed by L. Cancelara, IKZ.

HTA as reported by Czochralski growth in case of Si [97]. Similar defects are observed in TEM diffraction contrast images of SP-HTA AlN layers reported in Ref. [70]. However, since the voids are located exclusively in the AlN layers, no significant direct influence of the voids on the active region and on the IQE is expected.

TEM measurements provide an accurate estimate of the local dislocation density thanks to a reliable estimation of the layer thicknesses. Figure 2.15 shows the TDD distribution in the MQW samples on the different AlN/sapphire templates along the growth direction. The average TDD near the active region of the MQW samples on ELO, HTA planar and HTA ELO is determined to $1.7 \times 10^9 \text{ cm}^{-2}$, $1.3 \times 10^9 \text{ cm}^{-2}$ and $0.9 \times 10^9 \text{ cm}^{-2}$. Note that the measured TDD is taken over a full period of the ELO pattern (see CL results described above and section 2.2.2 for the exact distribution) as the UVC-LED devices always include both the reduced TDD regions above the ELO trenches and the higher TDD regions above the ELO ridges. Since the screw- and mixed-dislocation densities are about one order of magnitude lower than the edge-type dislocation densities, a further reduction in the screw-type dislocation densities approaches the TEM detection limit, leading to unreliable statistics. However, Fig. 2.14 indicates a higher screw- and mixed-type dislocation density of the ELO template compared to the HTA-based templates. Consequently, the total TDD in Fig. 2.15 is mainly attributed to the edge-type dislocation density. Due to dislocation annihilation,

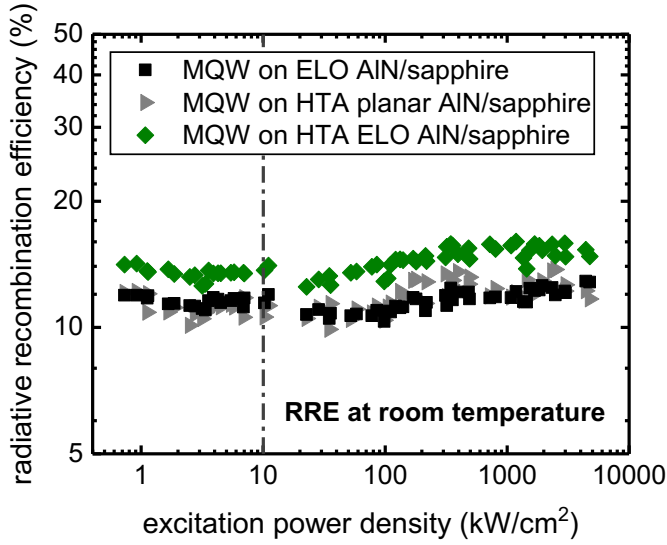


Figure 2.16: Estimated RRE of the MQW heterostructures on ELO AlN (black), HTA planar AlN (gray) and HTA ELO AlN (green) as a function of the excitation power density. Measurements performed by B. Belde, TUB.

a significant reduction of about 50% is observed for the thicker ELO AlN and HTA ELO AlN templates. However, in the HTA planar sample, the TDD remains constant when increasing the layer thickness, which is most likely a result of the thinner sample structure in combination with the already low TDD. A comparison between the MQW sample on ELO AlN and the MQW sample on HTA ELO AlN shows a significant reduction in TDD within the overall structure due to the HTA.

Finally, the RRE of the MQW samples was estimated by excitation power and temperature dependent PL spectroscopy (5 K - 300 K, 0.73 kW/cm^2 - 1170 kW/cm^2) using an ArF*-excimer laser (193 nm excitation wavelength). Similar to Fig. 2.9, all samples exhibit a pronounced MQW single peak emission at 4.8 eV and a barrier peak at 5.0 eV at a temperature of 5 K. The RRE is estimated by the ratio between the integrated PL intensity at 5 K and at 300 K, assuming no Shockley-Read-Hall recombination at 5 K (Fig. 2.16). The RREs at 10 kW/cm^2 are estimated to 11% (ELO AlN), 11% (HTA planar AlN) and 14% (HTA ELO AlN). This trend in between samples is consistent within the whole measurement range. As discussed in section 2.2.2, the RRE estimation with PL is challenging and should only be considered qualitatively. Nevertheless, these results indicate that a HTA treatment leads to reduced TDD within AlGaN-based MQWs and thus to an improved RRE on HTA ELO AlN templates.

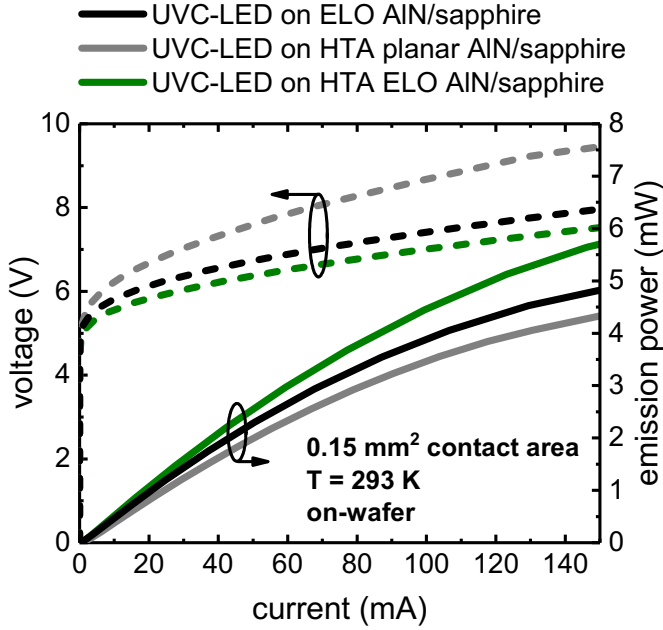


Figure 2.17: Representative LIV curves of the UVC-LEDs grown on ELO AlN, HTA planar AlN and HTA ELO AlN. Measurements performed together with E. Ziffer, TUB.

2.3.2 Enhanced efficiency of UVC-LEDs

To perform electro-optical characterisations, UVC-LEDs grown on the ELO AlN template, HTA planar AlN template and HTA ELO AlN template were fabricated and processed (in the same growth and process run) as described in section 2.1. The EL spectra and output powers of the UVC-LEDs were measured on-wafer at room temperature without active cooling and in cw-operation. Similar to Fig. 2.10(a) the EL spectra (not shown here) exhibit a single peak emission at a wavelength of 263 nm at 20 mA. Figure 2.17 shows the representative LIV curves of the UVC-LEDs grown on the different AlN/sapphire templates. Output powers of 0.9 mW, 0.8 mW and 1.1 mW with operating voltages of 6.1 V, 6.7 V and 5.8 V at a current of 20 mA are achieved for UVC-LEDs grown on ELO AlN, HTA planar AlN and HTA ELO AlN, respectively. Note that due to smaller series resistances of the UVC-LEDs grown on ELO templates, lower operating voltages are observed. These results are consistent with TLM measurements, which revealed a lower sheet resistivity of the *n*-side. It is worth noting here that a high amount of threading dislocations can degrade the electrical properties of AlGaIn:Si [98, 99]. However, the higher voltage of the UVC-LED on HTA planar AlN is probably due to process inaccuracies, as the TDD of the HTA planar AlN template is slightly lower than the TDD of the ELO AlN template (see section 2.3.1). Although the MQW heterostructure grown on the HTA planar AlN template showed a slightly lower TDD compared to the MQW heterostructure grown on the ELO AlN template, the on-wafer

output power in Fig. 2.17 is lower. The higher output power for ELO templates is attributed to the improved LEE due to the stripe-patterned AlN-sapphire interface [91]. Similar to section 2.2.3, the on-wafer LEEs of the UVC-LEDs grown on different AlN/sapphire templates were estimated by Monte Carlo ray-tracing simulations [91]. The degree of optical polarization of the EL emission was determined by in-plane emission from cleaved facets (see section 2.2.3 for further details) [92] to 0.76, 0.86 and 0.79 on the ELO AlN, HTA planar AlN and HTA ELO AlN templates, respectively⁶. Consistent with section 2.2.3, a higher degree of polarization was measured for the MQW heterostructure grown on the HTA-based templates due to the higher compressive strain. The on-wafer LEE of the UVC-LEDs were estimated to 3.4% on the HTA planar template and 3.9% on the ELO templates. These LEE values are identical to those presented in section 2.2.3 and show a 15% enhancement in the LEE due to the stripe patterned voids at the AlN-sapphire interface of the ELO templates.

Figure 2.18 compares the total TDD determined by the RC-FWHM and cross-sectional TEM as well as the dark spot density measured by the panchromatic CL intensity maps (see section 2.3.1). Additionally, the IQE is estimated by the model reported by Karpov et al. [62] using SiLENSe assuming $j = 13 \text{ A/cm}^2$, $\mu_e = 120 \text{ cm}^2/\text{Vs}$ and $\mu_h = 6 \text{ cm}^2/\text{Vs}$. The TDD value used in the model is based on the cross-sectional TEM evaluation. Further non-radiative recombination mechanisms, such as point defects, were not considered in the simulation. The IQEs are estimated to 26% (ELO AlN), 31% (HTA planar AlN) and 40% (HTA ELO AlN). This trend is consistent with the IQEs calculated from EL-EQEs ($j = 13 \text{ A/cm}^2$) and the simulated LEEs ($\text{IQE} = \text{EQE} / \text{LEE}$) as well as with the RREs estimated by PL. However, the RRE should be equal (for $\text{CIE} = 1$) or higher (for $\text{CIE} < 1$) than the IQE (see section 1.1). The too low RRE is most likely attributed to the high uncertainty of the non-resonant PL evaluation, as discussed in section 2.2.2. Nevertheless, the trend for the IQEs and RRE as well as for the estimated TDDs and dark spot densities in Fig. 2.18 are in excellent agreement. In particular, the results demonstrate a reduced TDD and a higher IQE of the MQW heterostructures and UVC-LEDs grown on the HTA ELO AlN template compared to the heterostructures grown on the ELO AlN and HTA planar AlN templates.

The enhanced output power of the UVC-LEDs grown on HTA ELO AlN was also

⁶Ray-tracing simulations and measurements of the optical polarization were performed by M. Guttman, TUB.

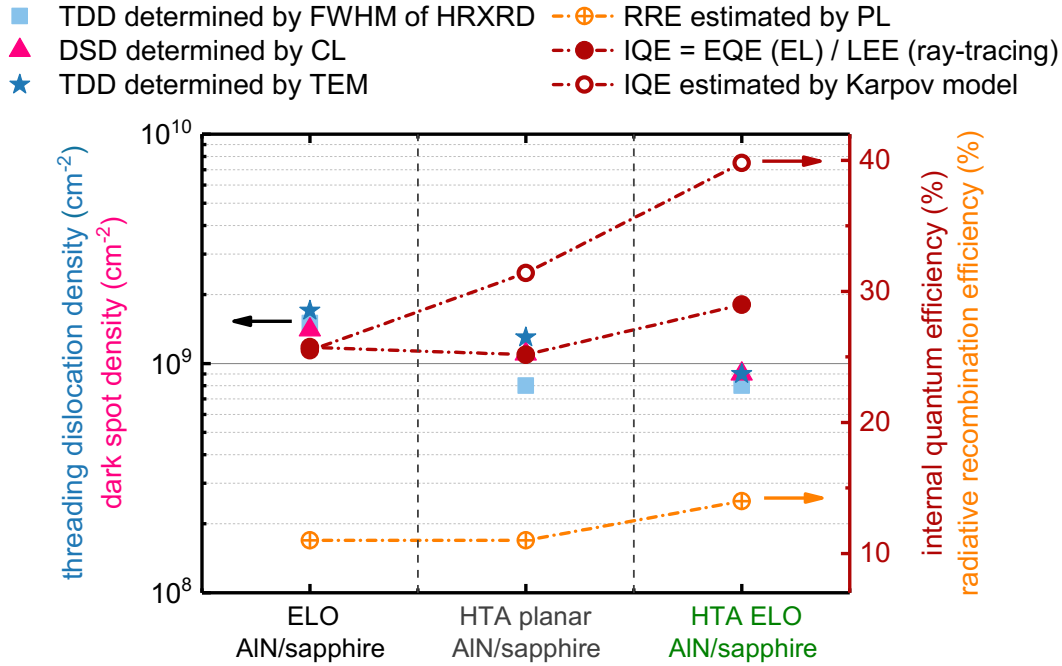


Figure 2.18: TDD determined by HRXRD and by cross-sectional TEM and dark spot density measured by CL topograms. RRE estimated by temperature and excitation power dependent PL at 10 kW/cm² and 300 K as well as the IQE estimated by SiLENSe simulations using the model reported by Karpov et al. [62] and by the EL-results at a current density of $j = 13$ A/cm². SiLENSe simulations performed by M. Guttman.

reproduced on the chip level⁷. The heterostructures were processed into 1-mm² flip-chip LEDs with 0.52-mm² Pt *p*-contacts mounted on AlN-based planar packages. The LI characteristics were measured at a controlled temperature of 288 K and in a calibrated integrating sphere. Figure 2.19 shows the LI characteristics of the UVC-LED chips on ELO AlN and HTA ELO AlN. Due to the improved light and heat extraction, an output power of 24 mW (ELO AlN) and 29 mW (HTA ELO AlN) measured at 350 mA and 13 V was obtained. The EQEs determined at 50 mA of the UVC-LED chips on ELO AlN and HTA ELO AlN are 2.0% and 2.4%, corresponding to WPEs of 1.0% and 1.2%, respectively. Furthermore, a silicone based material, SCHOTT[®] DEEP UV200 with an absorption coefficient of less than 2 cm⁻¹ [100] at a wavelength of 265 nm and with an intermediate refractive index of 1.45 [100] between air (1.0) [101] and sapphire (1.8) [102] was used for the encapsulation of the packaged UVC-LED chips⁸. The encapsulation of the UVC-LED chips into hemispherical DEEP UV200 has improved the total output power by 75% and 62% - from 24 mW to 42 mW and 29 mW to 47 mW for ELO AlN and HTA ELO AlN,

⁷The chip process was performed by J. Rass and N. Lobo-Ploch, FBH.

⁸The encapsulation was performed by S. Wu, TUB.

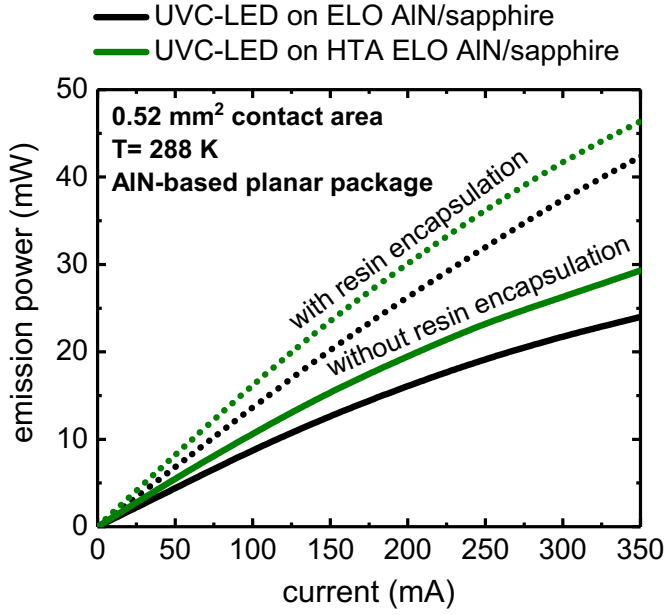


Figure 2.19: Integrating sphere measurements of the EL emission power of UVC-LED chips with (dotted line) and without (solid line) DEEP UV200 encapsulation on ELO (black) and HTA ELO (green). Measurements performed by N. Lobo-Ploch, FBH.

respectively (Fig. 2.19). The maximum EQE of the encapsulated UVC-LED chips using ELO AlN and HTA ELO AlN were 3.0% and 3.6% corresponding to WPEs of 2.2% and 2.7%, respectively, and was measured at 50 mA and 6.3 V. Consistently, ray-tracing simulations of the UVC-LED encapsulated in resin showed a 75% enhancement in the LEE due to the hemispherical encapsulation⁹. Furthermore, the total output power improvement is in agreement with the light extraction enhancement ratio of 1.5 observed by Nagai et al. [103] using a similar UV-absorbing *p*-side [104, 105] and a hemispherical encapsulation [103].

The efficiencies are in line with the results of other publications when comparing the EQEs summarized by Kneissl et al. [3]. The highest reported EQE for AlGaIn-based UVC-LEDs with an emission wavelength smaller than 270 nm is 6.3% at a current of 200 mA ($\lambda = 265$ nm) with the use of AlN bulk substrates [23]. The highest reported EQE between 270 nm and 300 nm is 20% (WPE: 5.7% at 16 V and 20 mA, $\lambda = 275$ nm) and was published in 2017 by Riken in cooperation with Panasonic [22]. Similar to the UVC-LEDs presented in this chapter, the UVC-LEDs were grown on a patterned AlN/sapphire template and later encapsulated with lens-like resins. Note that the high WPE and high EQE in this publications were mainly ascribed to an enhanced LEE by using a transparent *p*-side combined with a highly reflective Rh *p*-electrode. A higher efficiency thanks to a transparent *p*-side and to a reflective *p*-contact is expected also in case of the UVC-LEDs fabricated within this work frame (see chapter 5).

⁹Ray-tracing simulations were performed by M. Guttman, TUB.

However, to ensure reliable comparisons in between the different AlN/sapphire templates a non-transparent p -side rather than a transparent p -side is used in this chapter.

2.3.3 Reduced operation-induced degradation

The emission powers presented in the last section were recorded at 0 h of operation. The lifetime of state-of-the-art UVC-LEDs is currently limited to a few thousands hours [106]. Consequently, a strong decrease in the emission power is expected with increasing operating time. Different degradation mechanisms in (Al)GaN-based UV-LEDs have been reported in the literature [107–114]. Some results indicate that defects may play a role in operation-induced degradation [115]. In particular, an activation of defects is often discussed as the cause of degradation [116]. Accordingly, a low density of threading dislocations (for instance, the use of HTA ELO AlN/sapphire templates) could decelerate the degradation of UVC-LEDs. For this purpose, nominally identical UVC-LED heterostructures emitting at 265 nm were grown on ELO AlN/sapphire and HTA ELO AlN/sapphire. After epitaxial growth, the heterostructures were processed into 1-mm² chip LEDs with 0.33-mm² Pt-based p -contacts and V-based n -contacts. After dicing the wafer, the LEDs were flip-chip mounted on AlN-based planar packages¹⁰.

For each AlN/sapphire template, a batch of 15 UVC-LEDs was investigated. To account for inhomogeneities in the epitaxial growth and in the chip process, the investigated UVC-LEDs were selected from different areas within the wafers. The UVC-LEDs were simultaneously operated with a constant current of 200 mA corresponding to a current density of 60 A/cm² and a controlled heat sink temperature of 20 °C for 1,000 h in air atmosphere. During operation, the emission power of the UVC-LEDs was periodically recorded. In both batches, 13 of 15 UVC-LED chips reached 1,000 h without a catastrophic failure event (e.g. a short circuit). Empirical studies by Ruschel et al. [116] revealed that the emission power during long operating periods depends logarithmically on the time. Accordingly, Fig. 2.20 shows the average normalized emission power over the logarithmic time scale for the UVC-LEDs on HTA ELO AlN and on ELO AlN. The error bars correspond to the standard deviation of the 13 UVC-LED chips. The solid lines in Fig. 2.20 represent the fits according to the empirically

¹⁰The chip process was performed by J. Rass and N. Lobo-Ploch, FBH.

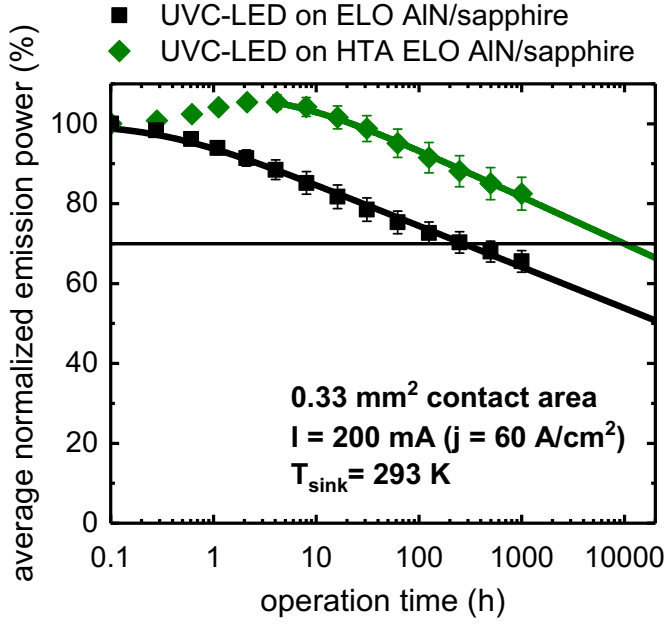


Figure 2.20: Average normalized emission power as a function of the operation time of UVC-LED chips on ELO AlN (black) and HTA ELO AlN (green). The error bars correspond to the standard deviation over 13 measured devices. Measurements performed by J. Ruschel, FBH.

derived Eq.

$$P(t) = -\beta \cdot \ln(\alpha \cdot j^3 + e^{-1/\beta}) \quad (2.1)$$

from Ref. [116], where P is the emission power, α and β are fit parameters and j is the current density. The empirical model allows the prediction of the L70 lifetime, i.e. the operating time after which the emission power is reduced to 70% of its initial value. For UVC-LEDs on HTA ELO AlN, an average L70 lifetime of 10,000 h is expected. This average L70 lifetime is about 40 times longer than the L70 lifetime of the UVC-LEDs on ELO AlN, which was estimated to be 250 h (on average). Figure 2.20 shows a different degradation behaviour in the first 20 h of operation between the UVC-LED on HTA ELO AlN and on ELO AlN. In particular, the operation time after which the logarithmic time dependence (Eq. 2.1) of the degradation of the emission power is observed differs between the UVC-LED on HTA ELO AlN and on ELO AlN. Ruschel et al. [116] suggested that during operation, the activation and/or generation of point defects improves the CIE into the AlGaIn-based MQW active region. For example, the breaking of Mg-H complexes (due to carriers with high energy generated by Auger recombinations, see [116] for further details) could activate Mg acceptors, resulting in improved hole injection. After a certain time of operation, however, this process is saturated and the emission power decreases. This reduction is suggested to be the result of an increase of Shockley-Read-Hall recombination centers. Consequently, the improved degradation behaviour of the UVC-LED on HTA ELO AlN might be caused by a lower density of defects

which are relevant for degradation and are associated with the reduced TDD.

Finally, the results reveal that UVC-LEDs on HTA ELO AlN show an enhanced emission power due to an increase of the IQE as well as the LEE compared to HTA planar AlN and ELO AlN templates. In addition, the degradation behavior is decelerated with the lower TDD. The L70 lifetime value was estimated to be 10,000 h, which is about 40 times longer compared to the UVC-LED on ELO AlN.

2.4 Summary and conclusion

In this chapter, AlGaIn-based MQW heterostructures and UVC-LEDs emitting at around 265 nm were grown on different AlN/sapphire templates with reduced TDD. In the first section, the applicability of relatively thin, inexpensive SP-HTA AlN templates as an alternative to thick and relatively expensive ELO AlN templates was analyzed. HRXRD and panchromatic CL measurements revealed a similar crystal quality and a TDD in the range of $1 \times 10^9 \text{ cm}^{-2}$. Finally, the UVC-LEDs grown on the ELO AlN template and on the SP-HTA AlN templates showed almost identical LI characteristics, with output powers of 0.7 mW at 20 mA (measured on-wafer). Consequently, SP-HTA AlN templates open a new way which allows the low-cost fabrication of efficient UVC-LEDs.

Ray-tracing simulations of the UVC-LED on ELO AlN and on SP-HTA AlN showed a 15% improvement in LEE due to the striped patterned voids, indicating the potential of a combined beneficial effect of HTA and an ELO process. In the second section, the combined effect of a structured AlN-sapphire interface and HTA on the growth and on the electro-optical characteristics of MQW heterostructures and UVC-LEDs was investigated. To break down the effects of a patterned AlN-sapphire interface and HTA, an ELO AlN template and a HTA planar AlN template were also fabricated. HRXRD, panchromatic CL topograms and cross-sectional TEM studies consistently showed a reduced dislocation density below 10^9 cm^{-2} combined with a higher IQE on the HTA ELO AlN template compared to the HTA planar AlN template and ELO AlN template. The UVC-LED performance was also increased by reducing the TDD and improving the LEE. UVC-LED chips using HTA ELO AlN were presented showing an improved extrapolated L70 lifetime of 10,000 h and an EQE of 3.6% corresponding to a WPE of 2.7% at 50 mA and 6.3 V.

3

Strain-induced defect generation in pseudomorphic AlGa_xN:Si

In this chapter, the influence of the design of the Al_xGa_{1-x}N:Si *n*-side on the performance characteristics of UVC-LEDs emitting near 265 nm is investigated. Usually, AlGa_xN:Si current spreading layers with thicknesses in the μm range are used [117, 118]. A thick AlGa_xN:Si layer can cause mutual dislocation annihilation and reduce the sheet resistance [119–121]. The formation of ohmic *n*-electrodes on Al_xGa_{1-x}N:Si layers with low Al mole fractions ($x < 0.7$) is less challenging compared to high Al mole fractions [122] due to a lower and thinner Schottky barrier at the semiconductor-metal interface [123]. Two basic mechanisms are involved [124]. First, the lower electron affinity of Al_xGa_{1-x}N with higher Al mole fraction x [125] in combination with the lack of a suitable metal with a work-function below 4 eV leads to an increase of the potential barrier with increasing Al mole fraction [124]. Secondly, the extraction of N by the contact metal during thermal annealing becomes energetically less favourable for high Al mole fractions, since the AlN bond is energetically more stable than the GaN bond [126]. As N vacancies can act as donors [127], this inhibits the formation of a highly *n*-doped layer directly below the contact metal [128, 129], thus thinning the Schottky barrier [130]. Consequently, Al_xGa_{1-x}N:Si layers with low Al mole fraction ($x < 0.7$) are favorable in order to reduce the contact resistance and the operating voltage of UVC-LEDs [131]. However, the *n*-side must be transparent to the emitted light to avoid re-absorption within the Al_xGa_{1-x}N:Si layer, which would lead to a reduced LEE [131]. For this reason, the transparency of the Al_xGa_{1-x}N:Si layer determines the lower limit for the Al mole fraction. In addition, the lattice mismatch between the AlN/sapphire template and the Al_xGa_{1-x}N:Si current spreading layer increases

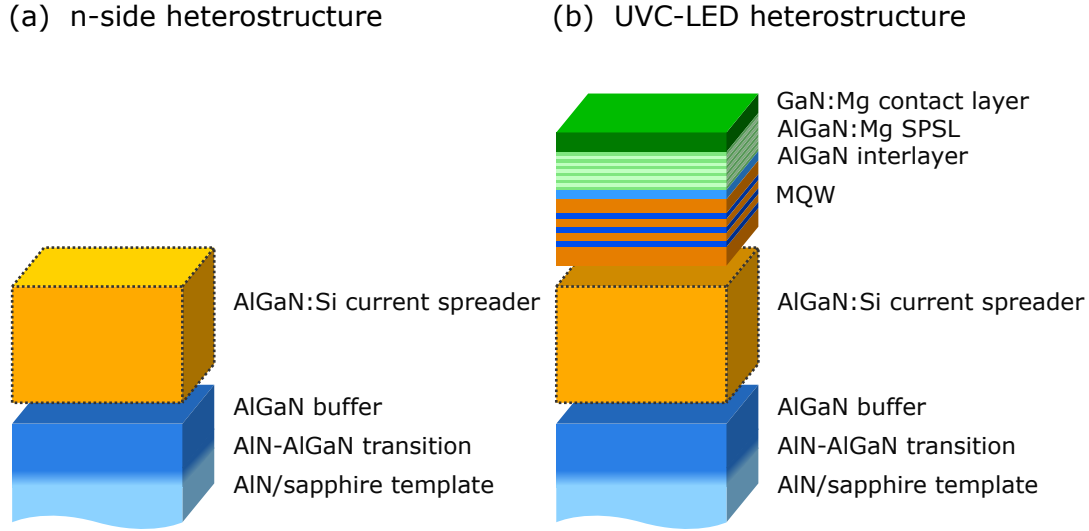


Figure 3.1: Schematic of the (a) *n*-side heterostructure sample and (b) UVC-LED heterostructure grown on ELO AlN/sapphire templates.

with decreasing Al mole fraction x . Thus, the generation of strain-induced defects for low Al mole fraction must also be addressed. Generated defects on the *n*-side are known to increase the sheet resistance [132, 133] and to penetrate the AlGa_xN-based MQW active region, acting as non-radiative recombination centers thus reducing the LED efficiency [60]. In this chapter, a detailed investigation of the effect of the Al mole fraction x in the Al _{x} Ga _{$1-x$} N:Si current spreading layer on the crystal quality of UVC-LED heterostructure as well as on the emission power is presented. The AlGa _{x} N-based heterostructures (schematically shown in Fig. 3.1) were grown by MOVPE on ELO AlN/sapphire templates. After the growth of a 600-nm AlN buffer layer, a 25-nm-thick AlN-AlGa _{x} N transition, a 100-nm-thick Al _{x} Ga _{$1-x$} N buffer and a 1200-nm-thick Al _{x} Ga _{$1-x$} N:Si *n*-side current spreading layer with an Al mole fraction between 0.60 and 0.90 as well as a threefold Al_{0.62}Ga_{0.38}N/Al_{0.48}Ga_{0.52}N MQW were deposited. Subsequently, a 5-nm-thick Al_{0.85}Ga_{0.15}N interlayer, a 100-nm-thick Al_{0.75}Ga_{0.25}N:Mg/Al_{0.55}Ga_{0.45}N:Mg SPSL and a 40-nm-thick GaN:Mg contact layer were grown. In addition, AFM, UV-transmission spectrometry and XRD measurements were performed on Al _{x} Ga _{$1-x$} N:Si *n*-side samples to investigate the morphology, transparency and the strain state. The *n*-side samples are identical to the UVC-LED heterostructure, except for the omitted MQW active region and *p*-layers in order to avoid absorption and an overlap of reflections in the reciprocal space.

3.1 Morphology, transparency and strain

The surface morphology is essential for the growth of the AlGa_xN-based MQW active region. A rough surface for the *n*-side can lead to undesired inhomogeneities in the AlGa_xN composition due to enhanced Ga-incorporation at step edges [134, 135]. Figure 3.2(a) shows AFM topograms of the Al_xGa_{1-x}N:Si *n*-side samples with different Al mole fraction *x*. The high dislocation density of the AlN layer on sapphire results in step-pinning and a high degree of spiral growth leading to a hillock dominated surface morphology (see section 2 and Fig. 2.7(a)) in the AlGa_xN:Si *n*-side layer [136, 137]. A change in the surface morphology for the Al_{0.50}Ga_{0.50}N:Si layers is observed, resulting in a high RMS value of 33 nm in a measurement range of 25 × 25 μm², whereas for *x* > 0.56 RMS values below 7 nm were determined. For *x* > 0.56, a constant hillock height of ~30 nm was measured by AFM independent of the Al mole fraction *x* in the Al_xGa_{1-x}N:Si *n*-side layer. For Al mole fraction *x* < 0.70 small hillocks with a hillock radius < 1 μm and large hillocks with a hillock radius > 1 μm are

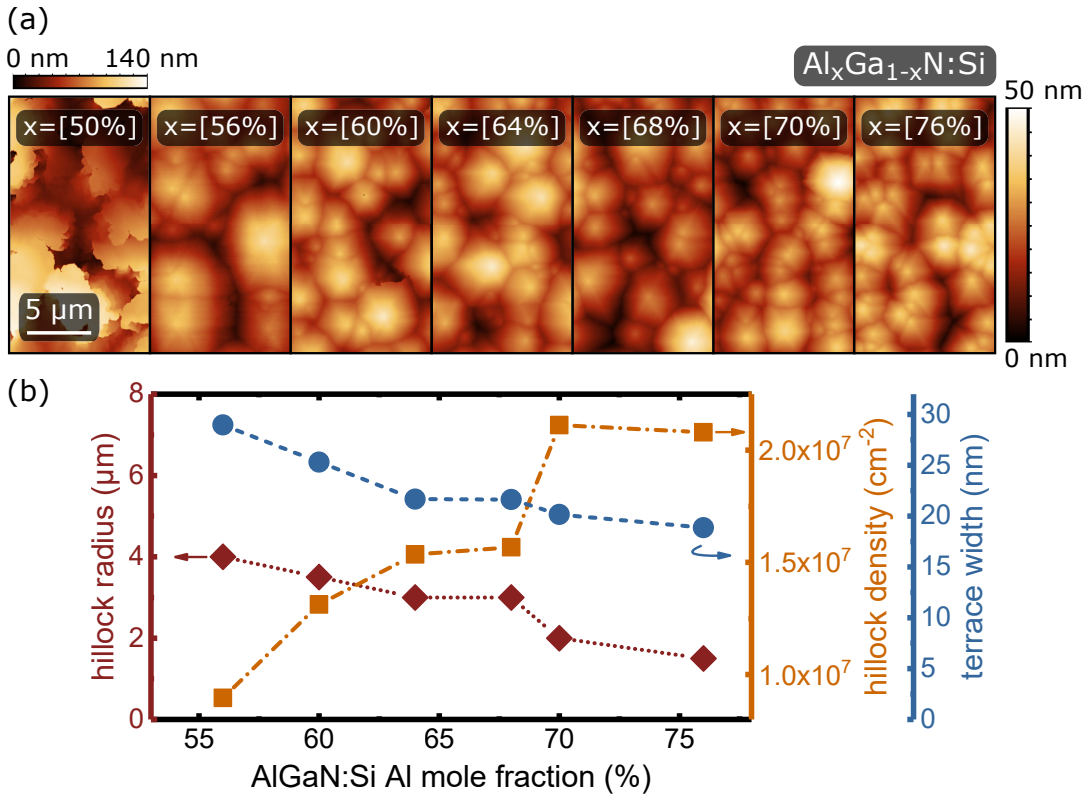


Figure 3.2: (a) AFM topograms of the 1200-nm-thick Al_xGa_{1-x}N:Si layers with different Al mole fraction *x*. (b) Hillock radius and estimated average terrace width of the large hillocks as well as hillock density as a function of the Al mole fraction *x* in the Al_xGa_{1-x}N:Si layers. Measurements performed together with C. Kuhn, TUB.

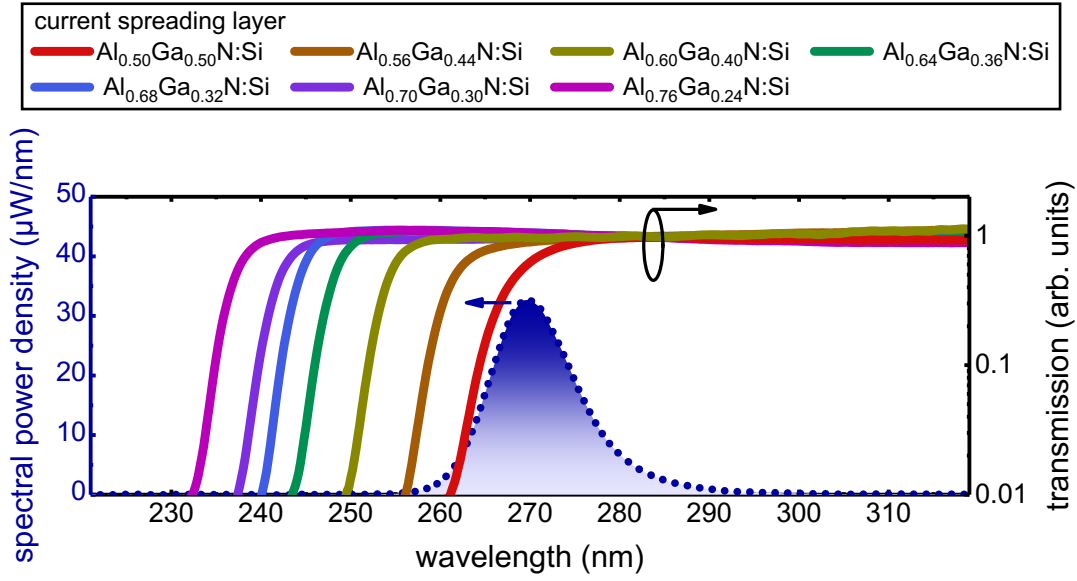


Figure 3.3: Spectral power density of a representative UVC-LED containing a 1200-nm-thick Al_{0.76}Ga_{0.24}N:Si current spreading layer at a current of 20 mA and a temperature of 300 K and transmission spectra of 1200-nm-thick Al_xGa_{1-x}N:Si layers with different Al mole fraction x . Transmission measurements performed together with C. Kuhn, TUB.

observed. In particular, the hillock radius of the large hillocks decreases from 4.0 μm ($x = 0.56$) down to 1.5 μm ($x = 0.76$) with increasing Al mole fraction x (Fig. 3.2(b)). With decreasing hillock radius, the hillock density increases from $0.9 \times 10^7 \text{ cm}^{-2}$ ($x = 0.56$) to $2.1 \times 10^7 \text{ cm}^{-2}$ ($x = 0.76$). When considering a hillock radius R_{hillock} , a hillock height h_{hillock} and a bilayer step height $c/2$ [54], the average spiral terrace width can be estimated by

$$d_{\text{terrace}} = \frac{R_{\text{hillock}}}{h_{\text{hillock}}} \cdot \frac{c}{2}. \quad (3.1)$$

An average spiral terrace width of 29 nm for $x = 0.56$ and of 19 nm for $x = 0.76$ is estimated. The decreasing spiral terrace width with increasing Al mole fraction is congruent with the trend reported in the literature [136, 138, 139]. This is likely due to the short diffusion length of the Al adatoms relative to the Ga adatoms [140]. However, also the change of the growth conditions, such as the V/III partial pressure ratio, can influence the surface morphology [141, 142]. The high surface roughness of the Al_{0.50}Ga_{0.50}N:Si layer may affect the growth of the AlGa_xN-based MQW active region [134, 135] in terms of the homogeneity of the composition and the thickness, while the surface roughness might be sufficiently low for Al mole fractions $x \geq 0.56$ to realize a homogeneous growth.

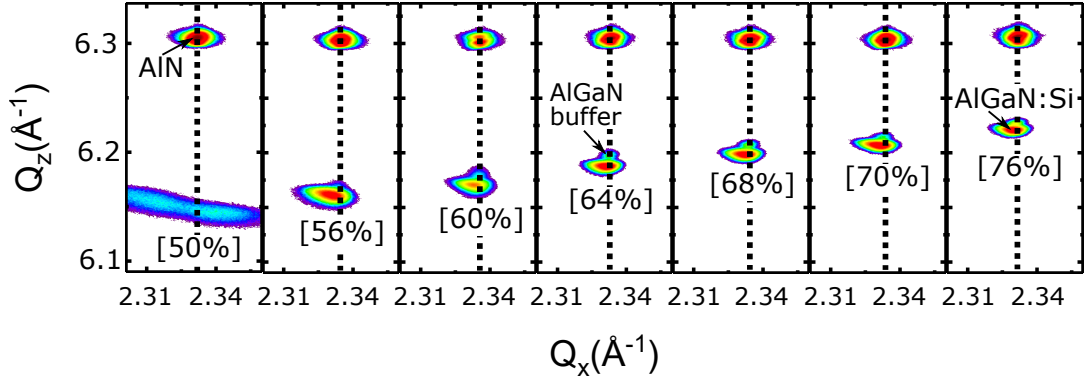


Figure 3.4: XRD reciprocal space maps near the $(10\bar{1}5)$ AlN reflection of 1200-nm-thick $\text{Al}_x\text{Ga}_{1-x}\text{N}:\text{Si}$ n -side samples with different Al mole fraction x . For Al mole fractions $x > 0.6$, only a small fraction of the $\text{Al}_x\text{Ga}_{1-x}\text{N}:\text{Si}$ layer shows partial relaxation. Measurements performed together with C. Kuhn, TUB.

It is worth noting here that the UVC-LEDs are designed as bottom emitters. Consequently, the 1200-nm-thick $\text{Al}_x\text{Ga}_{1-x}\text{N}:\text{Si}$ n -side current spreading layer must be transparent to the UVC-LED emission wavelength to maximize the emission power. Figure 3.3 shows the transmission spectra of $\text{Al}_x\text{Ga}_{1-x}\text{N}:\text{Si}$ n -side samples with an Al mole fraction x varying between 0.50 and 0.76. Additionally, a representative EL emission spectrum of a UVC-LED grown on an $\text{Al}_{0.76}\text{Ga}_{0.24}\text{N}:\text{Si}$ current spreading layer at a current of 20 mA and a temperature of 300 K is shown. The transmission spectra were normalized at 285 nm assuming negligible absorption for all $\text{Al}_x\text{Ga}_{1-x}\text{N}:\text{Si}$ n -side samples at this wavelength. In the $\text{Al}_{0.50}\text{Ga}_{0.50}\text{N}:\text{Si}$ layer, the fundamental absorption exceeds 270 nm, which can lead to a significant absorption and thus to a reduced LEE. With increasing Al mole fraction x , the absorption edge of the $\text{Al}_x\text{Ga}_{1-x}\text{N}:\text{Si}$ layers is shifted to shorter wavelengths and the transparency for the quantum well emission is achieved for Al mole fractions $x > 0.56$.

In addition to the transparency of the n -side current spreading layer, the strain state is an important parameter for the device performance. Due to the larger lattice constant of AlGaN compared to AlN, the AlGaN:Si layers grown on the AlN buffer layers are under compressive stress, which leads to a compressive strain. Accordingly, a relaxation of the compressively strained AlGaN:Si layers must be considered once the critical layer thickness for the corresponding AlGaN composition has been exceeded. The plastic relaxation processes can lead to dislocation formation [119, 143], which may affect the IQE of UVC-LEDs [62, 144]. The strain state of the AlGaN:Si layers is therefore investigated by XRD reciprocal space maps (RSMs). Figure 3.4 shows RSMs near

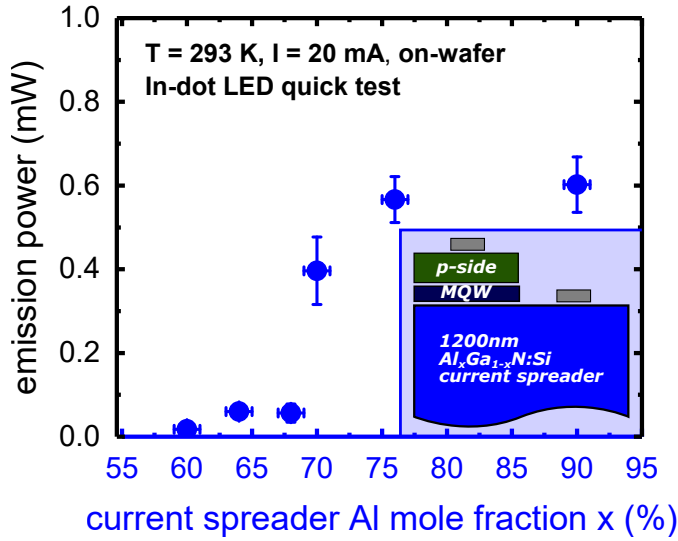


Figure 3.5: Average emission power of UVC-LEDs with 1200-nm-thick $\text{Al}_x\text{Ga}_{1-x}\text{N:Si}$ current spreading layers with different Al mole fraction x . The vertical error bars correspond to the standard deviation over at least four measured wafer positions.

the asymmetric $(10\bar{1}5)$ AlN reflection of the $\text{Al}_x\text{Ga}_{1-x}\text{N:Si}$ n -side samples with different Al mole fraction x . Note that the low-intensity peak at higher Q_z values compared to the $\text{Al}_x\text{Ga}_{1-x}\text{N:Si}$ layer corresponds to the 100-nm-thick AlGaIn buffer layer, which exhibits an approximately 2% higher Al mole fraction. For Al mole fractions $x > 0.6$, almost the same reciprocal lattice constant Q_x is observed in respect to the underlying AlN layer. In addition, no strong broadening of the reflection is visible, indicating an almost coherent growth, with only a small fraction of the $\text{Al}_x\text{Ga}_{1-x}\text{N:Si}$ layer that is partially relaxed. The $\text{Al}_{0.50}\text{Ga}_{0.50}\text{N:Si}$ reflection shows a strong broadening with large Q_x component, indicating a low layer quality. The results indicate that for 1200-nm-thick $\text{Al}_x\text{Ga}_{1-x}\text{N:Si}$ current spreading layers dislocation generation for an Al mole fraction $x < 0.6$ may occur due to plastic relaxation. However, it should be noted that relaxation can also occur without dislocation generation, e.g. by dislocation inclination, which would be less detrimental to the UVC-LED performance [145–148]. The resistivities of the $\text{Al}_x\text{Ga}_{1-x}\text{N:Si}$ layers between $x = 0.5$ and $x = 0.76$ were determined by contactless resistance measurements and show an almost constant resistivity value of $\rho \approx 0.028 \Omega\text{cm}$. However, for $\text{Al}_x\text{Ga}_{1-x}\text{N:Si}$ with $x > 0.80$ an increase in the resistivity is expected [117].

3.2 Reduced device efficiency and defect generation

The emission power of the UVC-LED heterostructures with $\text{Al}_x\text{Ga}_{1-x}\text{N:Si}$ current spreading layers was measured on-wafer, under direct current injection and at

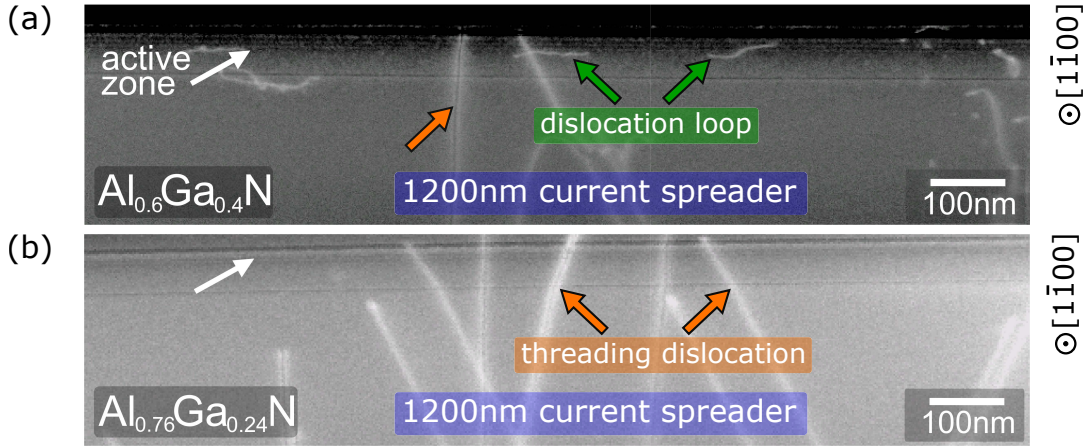


Figure 3.6: Cross-sectional ADF STEM images of the UVC-LEDs with (a) an Al_{0.60}Ga_{0.40}N:Si and with (b) an Al_{0.76}Ga_{0.24}N:Si *n*-side current spreading layer near the MQW active region in [1 $\bar{1}$ 00] direction. Measurements performed by J. Weinrich, IKZ.

room temperature using an indium dot quick test setup. Indium dots with a radius of approximately 500 μm were deposited on the GaN:Mg layer as *p*-contacts. The bottom emission power was measured with a calibrated large-area silicon photodiode. Figure 3.5 shows the emission power of the UVC-LEDs at 20 mA as a function of the Al mole fraction x in the 1200-nm-thick Al _{x} Ga_{1- x} N:Si *n*-side current spreading layer. The emission power between $x = 0.90$ and $x = 0.76$ is almost constant at 0.6 mW. However, as the Al mole fraction in the 1200-nm-thick Al _{x} Ga_{1- x} N:Si layer drops below $x = 0.76$, the emission power decreases drastically to 0.02 mW for $x = 0.60$. The drop in the emission power between $x = 0.76$ and $x = 0.60$ is not expected as no absorption in the *n*-side was observed (Fig. 3.3) and the XRD analysis does not reveal strong strain relaxation (Fig. 3.4) for these Al mole fractions.

In order to directly reveal the dislocation distribution, two UVC-LED heterostructures with an Al mole fraction of $x = 0.76$ and $x = 0.60$ in the Al _{x} Ga_{1- x} N:Si current spreading layer were prepared for TEM using standard thinning techniques. Figure 3.6 shows the cross-sectional annular dark-field (ADF) scanning transmission electron microscopy (STEM) images of the UVC-LED heterostructures with a 1200-nm-thick (a) Al_{0.60}Ga_{0.40}N:Si and (b) Al_{0.76}Ga_{0.24}N:Si layer near the MQW active region in the [1 $\bar{1}$ 00] direction. The position of the AlGaN-based MQW active region is indicated by a white arrow. Note that all types of dislocations (screw, edge and mixed) are visible in ADF STEM. Threading dislocations are indicated by a brown arrow and originate from the ELO AlN/sapphire template below. There appears to be an incline, which is in accordance with

the TEM images in section 2.3.1. It is important to note that the local TDD remains constant within the n -side current spreading layer as well as in the MQW active region. However, there is a formation of dislocation loops and dislocations with an irregular shape of dislocation lines in the UVC-LED heterostructure with an $\text{Al}_{0.60}\text{Ga}_{0.40}\text{N}:\text{Si}$ current spreading layer (green arrows in Fig. 3.6(a)). Assuming nearly in-plane circular loops, qualitatively estimated by several TEM projections, the mean dislocation line length is (230 ± 50) nm, where the error corresponds to the standard deviation. When crossing the AlGaIn-based MQW active region, the dislocation loops might act as non-radiative recombination centers, which obviously can lead to a reduction in the emission power of the UVC-LEDs [62, 149]. On the other hand, no dislocation loops were observed for the UVC-LED heterostructure with an $\text{Al}_{0.76}\text{Ga}_{0.24}\text{N}:\text{Si}$ layer (Fig. 3.6(b)), even after tilting the sample by up to 25° . Note that the generated dislocation loops do not result in large strain relaxation (i.e. a change in the reciprocal lattice constant Q_x), as suggested by the RSMs in Fig. 3.4. Considering the UVC-LED emission power reduction, the strain-induced dislocation generation in the 1200-nm-thick $\text{Al}_x\text{Ga}_{1-x}\text{N}:\text{Si}$ current spreading layer determines the lower limit of the Al mole fraction to $x = 0.76$.

3.3 Heterostructure approach to suppress the defect generation

In order to preserve the emission power, a different approach is required to reduce the Al mole fraction below $x = 0.76$ while suppressing dislocation generation. Since the generation of dislocations is often associated with the layer thickness, the next step is a two-stage heterostructure approach for the n -side as shown schematically in Fig. 3.7. The 1200-nm-thick AlGaIn:Si layer is divided into

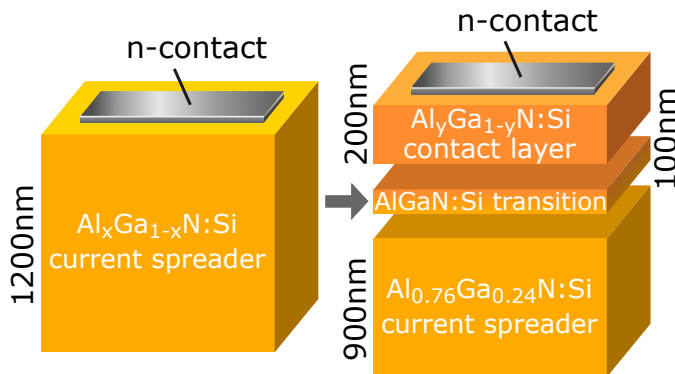


Figure 3.7: Scheme of the two-stage heterostructure approach for the n -side. In the new approach the n -contact is deposited on the 200-nm-thick $\text{Al}_y\text{Ga}_{1-y}\text{N}:\text{Si}$ n -side contact layer.

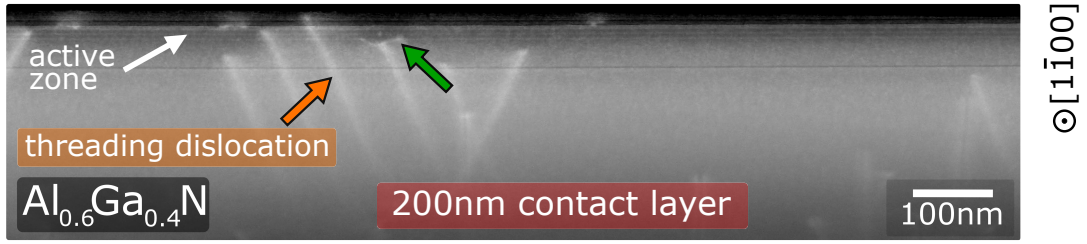


Figure 3.8: Cross-sectional ADF STEM images of the UVC-LED with a 900-nm-thick $\text{Al}_{0.76}\text{Ga}_{0.24}\text{N}:\text{Si}$ n -side current spreading layer, a 100-nm-thick transition layer and a 200-nm-thick $\text{Al}_{0.60}\text{Ga}_{0.40}\text{N}:\text{Si}$ n -side contact layer near the MQW active region in $[1\bar{1}00]$ direction. Measurements performed by J. Weinrich, IKZ.

a 900-nm-thick $\text{Al}_{0.76}\text{Ga}_{0.24}\text{N}:\text{Si}$ n -side current spreading layer, a 100-nm-thick $\text{Al}_{0.76 \rightarrow y}\text{Ga}_{0.24 \rightarrow 1-y}\text{N}:\text{Si}$ transition layer and a 200-nm-thick $\text{Al}_y\text{Ga}_{1-y}\text{N}:\text{Si}$ n -side contact layer. For low Al mole fractions y , this approach should improve the contact properties due to the thinner Schottky barrier while suppressing the formation of dislocation loops.

The new two-stage heterostructure approach for the n -side was integrated into the UVC-LED heterostructure and the Al mole fraction y of the 200-nm-thick $\text{Al}_y\text{Ga}_{1-y}\text{N}:\text{Si}$ n -side contact layer was varied between $y = 0.6$ and $y = 0.76$. Figure 3.8 shows ADF STEM images of the UVC-LED heterostructure with a 200-nm-thick $\text{Al}_{0.60}\text{Ga}_{0.40}\text{N}:\text{Si}$ n -side contact layer close to the MQW active region in $[1\bar{1}00]$ direction. The position of the UVC-LED active region is marked by a white arrow. Similar to Fig. 3.6, the threading dislocations (indicated by a brown arrow) are inclined and originate from the ELO AlN/sapphire template below. The green arrow in Fig. 3.8 might indicate a small dislocation loop segment. Nevertheless, the amount and length of dislocation loops seen in $[1\bar{1}00]$ -direction is significantly reduced compared to the 1200-nm-thick $\text{Al}_{0.60}\text{Ga}_{0.40}\text{N}:\text{Si}$ n -side current spreading layer (Fig. 3.6(a)). Accordingly, the increased formation of dislocation loops was effectively reduced with the two-step heterostructure approach for the n -side.

Figure 3.9 shows in red the on-wafer emission power using an indium dot quick test setup for UVC-LEDs featuring an $\text{Al}_y\text{Ga}_{1-y}\text{N}:\text{Si}$ n -side contact layer with Al mole fraction y . Note that for an Al mole fraction of $x = y = 0.76$ the UVC-LED heterostructures are nominally identical. The emission power of these UVC-LEDs is also similar with overlapping standard deviations. However, in contrast to the UVC-LEDs with 1200-nm $\text{Al}_x\text{Ga}_{1-x}\text{N}:\text{Si}$ n -side current spreading layers (blue circles), the emission power remains constant when the Al mole

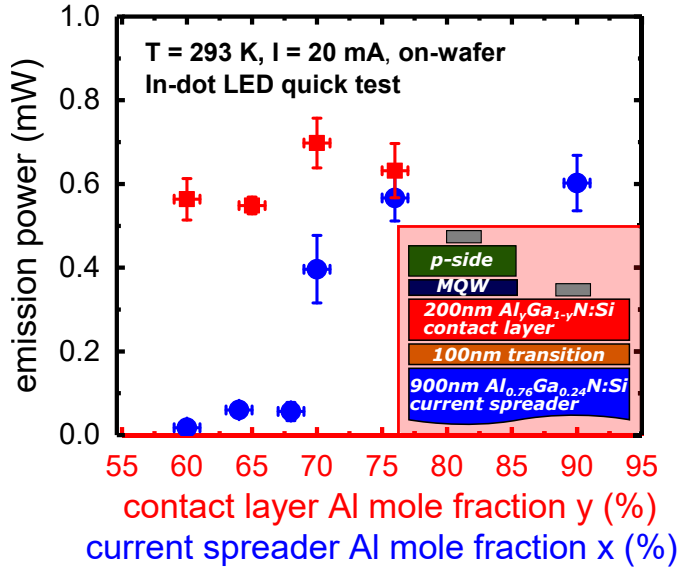


Figure 3.9: Average emission power of UVC-LEDs grown with 900-nm-thick $\text{Al}_{0.76}\text{Ga}_{0.24}\text{N}:\text{Si}$ current spreading layers, 100-nm-thick $\text{AlGaN}:\text{Si}$ transition layers and 200-nm-thick $\text{Al}_y\text{Ga}_{1-y}\text{N}:\text{Si}$ n -side contact layers with different Al mole fraction y (red squares) and with 1200-nm $\text{Al}_x\text{Ga}_{1-x}\text{N}:\text{Si}$ current spreading layers with different Al mole fraction x (blue circles). The vertical error bars corresponds to the standard deviation over at least four measured wafer positions.

fraction y in the 200-nm contact layer is reduced from $y = 0.7$ to $y = 0.6$. Therefore, the two-stage heterostructure approach for the n -side allows for the Al mole fraction to be reduced without sacrificing the emission power. While the layer resistivities of the $\text{AlGaN}:\text{Si}$ layers (with and without contact layer) between $x = y = 0.5$ and $x = y = 0.76$ determined by contactless resistance measurements are almost constant (i.e. $\rho_L \approx 0.028 \Omega\text{cm}$), the contact resistivity of the n -contacts strongly depends on the Al mole fraction. Transfer length method (TLM) measurements showed an increase in the contact resistivity from $\rho_C = (1.1 \pm 0.2) \cdot 10^{-5} \Omega\text{cm}^2$ ($x = y = 0.5$) to $\rho_C = (1.08 \pm 0.05) \cdot 10^{-3} \Omega\text{cm}^2$ ($x = y = 0.76$), where the errors correspond to the Gaussian error propagation of the TLM evaluation [123].

In order to quantify the reduction in the operating voltage when implementing the two-step heterostructure approach for the n -side, UVC-LEDs were processed by standard micro-fabrication techniques using palladium as p -contacts and vanadium-based n -contacts¹. Figure 3.10(a) shows representative current-voltage characteristics of a UVC-LED with a 1200-nm-thick $\text{Al}_{0.76}\text{Ga}_{0.24}\text{N}:\text{Si}$ n -side current spreading layer (blue curve) and of a UVC-LED with a 900-nm-thick $\text{Al}_{0.76}\text{Ga}_{0.24}\text{N}:\text{Si}$ current spreading layer, 100-nm-thick $\text{AlGaN}:\text{Si}$ transition layer and 200-nm-thick $\text{Al}_{0.65}\text{Ga}_{0.35}\text{N}:\text{Si}$ n -side contact layer (red curve). The two-stage heterostructure approach for the n -side is successful in reducing the operating voltage of the UVC-LED. At an injection current of 20 mA, the operating voltage is reduced by 2.2 V (from 8.3 V to 6.1 V).

¹The micro-fabrication process was performed by L. Sulmoni, TUB.

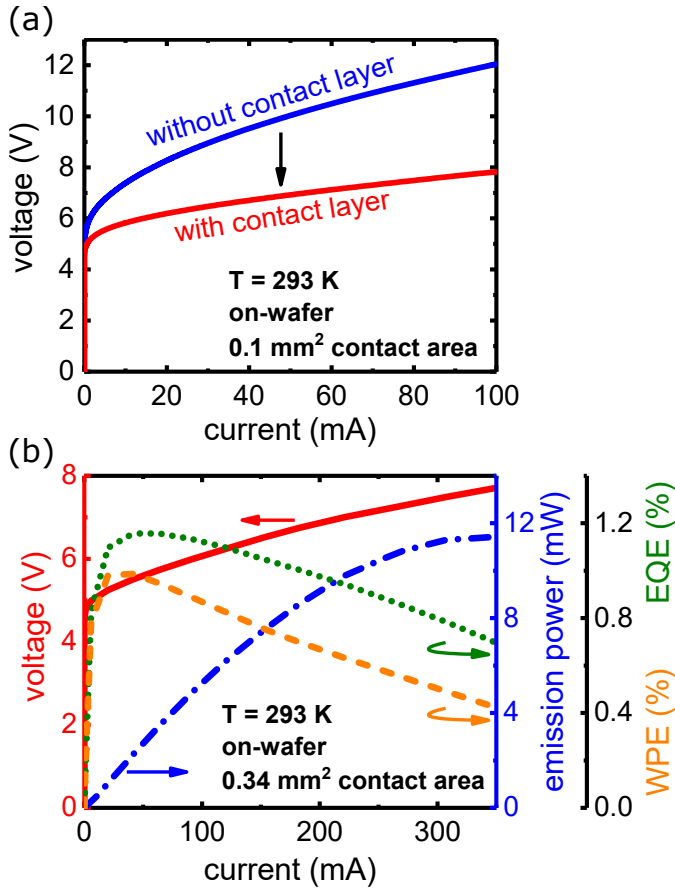


Figure 3.10: (a) Representative current-voltage characteristics of UVC-LEDs with a 1200-nm-thick $\text{Al}_{0.76}\text{Ga}_{0.24}\text{N}:\text{Si}$ n -side current spreading layer and a UVC-LED with a 900-nm-thick $\text{Al}_{0.76}\text{Ga}_{0.24}\text{N}:\text{Si}$ current spreading layer, 100-nm-thick $\text{AlGa}\text{N}:\text{Si}$ transition layer and 200-nm-thick $\text{Al}_{0.65}\text{Ga}_{0.35}\text{N}:\text{Si}$ contact layer. (b) (IV), (I-L), (I-EQE) and (I-WPE) of a UVC-LED with a 900-nm-thick $\text{Al}_{0.76}\text{Ga}_{0.24}\text{N}:\text{Si}$ current spreading layer, 100-nm-thick $\text{AlGa}\text{N}:\text{Si}$ transition layer and 200-nm-thick $\text{Al}_{0.65}\text{Ga}_{0.35}\text{N}:\text{Si}$ contact layer.

The heterostructure approach for the n -side also allows the fabrication of highly efficient UVC-LEDs, which can be operated at higher injection currents due to lower Joule heating. The n -contacts are ohmic with a contact resistivity of $2 \times 10^{-5} \Omega\text{cm}^2$, determined from TLM measurements. Figure 3.10(b) shows the operating voltage (red curve), the emission power (blue curve), the EQE (green curve) and the WPE (orange curve) for a 265-nm UVC-LED with a 200-nm-thick $\text{Al}_{0.65}\text{Ga}_{0.35}\text{N}:\text{Si}$ n -side contact layer as a function of the injected current. The contact area of the UVC-LED was 0.34 mm^2 and was measured on-wafer in continuous-wave operation at room temperature without active cooling. Note that by further optimizing the p -side of the heterostructure and the micro-fabrication process, it was possible to improve further the performance of the 265-nm UVC-LEDs. The maximum emission power of 11.5 mW is achieved at a current of 320 mA, followed by a thermal rollover due to Joule heating. At 20 mA an emission power of 1.1 mW is obtained at an operating voltage of 5.2 V (which already approaches the bandgap $E_G = 4.7 \text{ eV}$ for a 265-nm UVC-LED), resulting in a WPE of 1.0%. This WPE of 1.0% is already in the range of commercially available UVC-LEDs (e.g. 2% reported in Ref. [150]).

The maximum reported WPE is 5.7% from Takano et al. [22]. However, for a conclusive comparison, these devices have still to be diced, flip-chip mounted and encapsulated (see section 2.3.2 for more details about the efficiency increase given by the chip process). These results demonstrate that the *n*-side two-stage heterostructure approach facilitates the growth of UVC-LEDs with low operating voltages, resulting in reduced Joule heating and finally higher WPE.

3.4 Summary and conclusion

In this chapter, the impact of the design of the $\text{Al}_x\text{Ga}_{1-x}\text{N}:\text{Si}$ *n*-side on the performance characteristics of bottom-emitting UVC-LEDs grown on ELO AlN/sapphire templates was investigated. The transparency to the UVC-LED emission wavelength of the $\text{Al}_x\text{Ga}_{1-x}\text{N}:\text{Si}$ *n*-side is mandatory for a decent light extraction and was achieved for $x \geq 0.56$. However, the growth of AlGaIn:Si current spreading layers on AlN/sapphire templates resulted in the formation of dislocation loops introduced by the compressive strain. According to ADF STEM images, the density of these dislocation loops increased with the compressive strain, i.e. with lower Al mole fraction. Furthermore, their presence strongly reduced the emission power of 265-nm UVC-LEDs, thus limiting the lower boundary for the Al mole fraction in the $\text{Al}_x\text{Ga}_{1-x}\text{N}:\text{Si}$ current spreading layer to $x = 0.76$. This process was successfully controlled by implementing a two-stage heterostructure approach for the *n*-side using a second thin $\text{Al}_y\text{Ga}_{1-y}\text{N}:\text{Si}$ contact layer with low Al mole fraction $y < x$. Finally, the operating voltages measured on-wafer were also significantly reduced by implementing an AlGaIn:Si contact layer. A UVC-LED emitting at 265 nm, which contains a 900-nm-thick $\text{Al}_{0.76}\text{Ga}_{0.24}\text{N}:\text{Si}$ *n*-side current spreading layer, a 100-nm-thick $\text{Al}_{0.76 \rightarrow 0.65}\text{Ga}_{0.24 \rightarrow 0.35}\text{N}:\text{Si}$ transition layer and a 200-nm-thick $\text{Al}_{0.65}\text{Ga}_{0.35}\text{N}:\text{Si}$ *n*-side contact layer was presented with an on-wafer emission power of 1.1 mW at an operating voltage as low as 5.2 V and at an injected current of 20 mA, resulting in a WPE of 1% in cw-operation.

4

Determination of the polarization fields in the active region

When designing the MQW active region of a UVC-LED, it is necessary to consider all the factors that influence the IQE of the device. Parallel to the dislocation density in the MQW active region discussed earlier, an additional effect that limits the IQE in III-nitride-based optical devices is the QCSE (see section 1.3). Therefore, it is important to have a good understanding of the influence of the polarization field magnitude to be able to design highly efficient UVC-LEDs. However, the magnitude of the polarization fields in III-nitride-based heterostructures is controversial [45]. In order to determine the polarization fields, an analytical model using capacitance-voltage measurements (CVM) is presented. It is based on the changes in the depletion region width of *pin*-diodes caused by the polarization sheet charges at the interfaces. The change in the width of the depletion region can be precisely determined by capacitance measurements assuming that the *pin*-diode can be described as a parallel plate capacitor. In order to evaluate the polarization fields analytically, it is necessary to compare the depletion region width of a homojunction reference sample (i.e., without polarization sheet charges) to the sample under investigation, including a double heterostructure with polarization sheet charges at the interfaces. As an additional approach, the polarization fields are extracted from the CVM with the help of self-consistent Poisson and drift-diffusion calculations using the internal polarization charges as a fitting parameter.

4.1 Introduction to the CVM-based analytical approach

In this section, the analytical equation for the determination of the internal polarization fields is derived. The assumption of a charge density distribution within the depletion region allows one to derive an equation for the width of the depletion region from which the internal polarization field can be extracted. In order to evaluate the influence of the parameters in the derived equation of the internal polarization field, a detailed accuracy analysis is performed. In addition, to minimize the error of the analytical approach, an advanced equivalent circuit model for the capacitance determination is developed and quantified.

4.1.1 Derivation of the equations

The approach for the derivation of the polarization field equation is the charge density $\rho(x)$ within the depletion region of an abrupt *pin*-junction

$$\begin{aligned} \rho(x) = & -qN_A (\Theta(x) - \Theta(x - x_p)) + \\ & + qN_i (\Theta(x - x_p) - \Theta(x - (x_p + x_i))) + \\ & + qN_D (\Theta(x - (x_p + x_i)) - \Theta(x - (x_p + x_i + x_n))) - \\ & - \sigma\delta(x - (x_p + x_{i1})) + \sigma\delta(x - (x_p + x_{i1} + x_d)). \end{aligned} \quad (4.1)$$

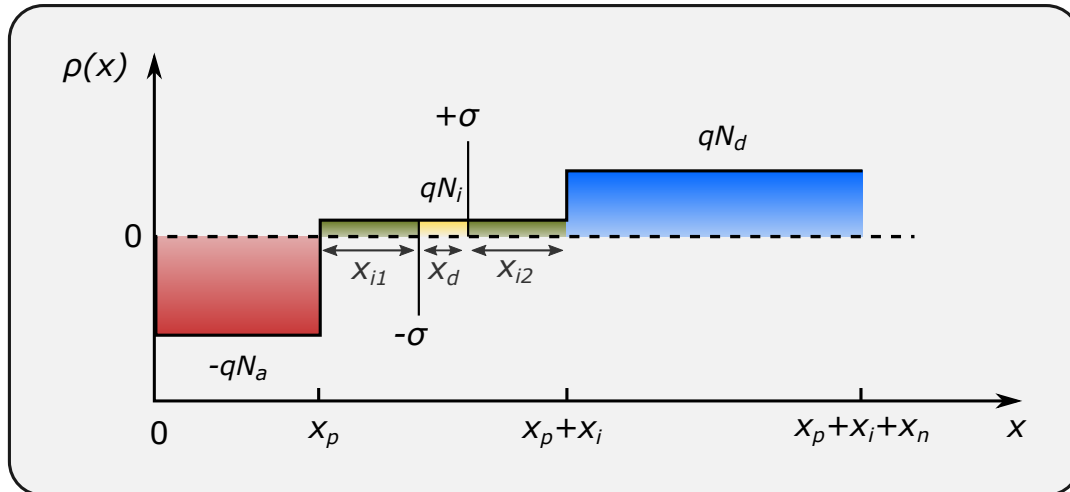


Figure 4.1: Assumed charge density distribution within the depletion region. N_A , N_D and N_i are the acceptor, donor and background doping concentrations. The polarization charges σ at the interfaces of the double heterostructure are described by delta functions.

x is the position in the depletion region, $\Theta(x)$ is the Heaviside step function, N_A and N_D are the acceptor and donor concentration of the p - and n -doped region, N_i is the n -type background doping concentration in the intrinsic region, x_p and x_n are the depletion region widths within the p - and n -sides, x_{i_1} , x_d and x_{i_2} are the different lengths within the double heterostructure, q is the elementary charge and σ the polarization charges. It should be noted that the sum of $x_{i_1} + x_d + x_{i_2}$ gives the thickness of the intrinsic layer x_i . The polarization charges σ at the interfaces of the double heterostructure are taken into account by introducing delta functions $\delta(x - x_0)$, where x_0 is the location of the interface. The assumed charge density distribution of Eq. 4.1 is illustrated in Fig. 4.1. The electric field $E(x)$ is calculated using the Maxwell equation $\nabla E(x) = \rho(x)/\epsilon_0\epsilon_r$

$$\begin{aligned}
 E(x) = \frac{1}{\epsilon_0\epsilon_r} & (-qN_A [x\Theta(x) - (x - x_p)\Theta(x - x_p)] + \\
 & + qN_i [(x - x_p)\Theta(x - x_p) - (x - (x_p + x_i))\Theta(x - (x_p + x_i))] + \\
 & + qN_D(x - (x_p + x_i))\Theta(x - (x_p + x_i)) - \\
 & - qN_D(x - (x_p + x_i + x_n))\Theta(x - (x_p + x_i + x_n)) - \\
 & - \sigma\Theta(x - (x_p + x_{i_1})) + \sigma\Theta(x - (x_p + x_{i_1} + x_d)) + C_1),
 \end{aligned} \tag{4.2}$$

where C_1 is the constant of integration, ϵ_0 is the vacuum permittivity and ϵ_r is the relative permittivity. Using the boundary condition $E(x = 0) \equiv 0 \equiv E(x = x_p + x_i + x_n)$, the constant of integration is given by $C_1 = 0 = qN_A x_p - qN_D x_n - qN_i x_i$, which is the principle of charge neutrality. The electric potential $\Phi(x)$ is calculated by an integration of the electric field $-\nabla\Phi(x) = E(x)$

$$\begin{aligned}
 \Phi(x) = \frac{1}{2\epsilon_0\epsilon_r} & (qN_A [x^2\Theta(x) - (x - x_p)^2\Theta(x - x_p)] - \\
 & - qN_i [(x - x_p)^2\Theta(x - x_p) - (x - (x_p + x_i))^2\Theta(x - (x_p + x_i))] - \\
 & - qN_D(x - (x_p + x_i))^2\Theta(x - (x_p + x_i)) + \\
 & + qN_D(x - (x_p + x_i + x_n))^2\Theta(x - (x_p + x_i + x_n)) - \\
 & - 2\sigma(x - (x_p + x_{i_1}))\Theta(x - (x_p + x_{i_1})) + \\
 & + 2\sigma(x - (x_p + x_{i_1} + x_d))\Theta(x - (x_p + x_{i_1} + x_d)) + C_2).
 \end{aligned} \tag{4.3}$$

The constant of integration $C_2 = 0$ is determined by the boundary condition $\Phi(x = 0) = 0$. With $\Phi(x = x_p + x_i + x_n) = V_{Ref}$ and evaluation of the Heaviside

step function $\Theta(x)$ the reference potential is given by

$$V_{Ref} = \frac{q}{2\epsilon_0\epsilon_r} (N_D x_n^2 + N_A x_p^2 - N_i x_i^2 + 2N_A x_p x_i) + E_{Pol} x_d, \quad (4.4)$$

where $E_{Pol} = \sigma/\epsilon_0\epsilon_r$ is the internal polarization field. It should be noted that the reference potential V_{Ref} is in principle identical to the built-in potential V_{bi} of a polarization unaffected *pin*-diode. Nevertheless, parasitic electric fields (generated by Schottky contacts or Fermi level pinning) can lead to a deviation of the reference potential V_{Ref} from the built-in potential V_{bi} . From Eq. 4.4 and the principle of charge neutrality the depletion region width within the *p*-side x_p and *n*-side x_n can be determined

$$x_n = -\frac{x_i N_D (N_i + N_A)}{N_D (N_A + N_D)} + \frac{\sqrt{N_D N_A \left[\frac{2\epsilon_0\epsilon_r (V_{Ref} - E_{Pol} x_d) (N_A + N_D)}{q} - (N_i - N_D) (N_i + N_A) x_i^2 \right]}}{N_D (N_A + N_D)}, \quad (4.5)$$

$$x_p = -\frac{x_i N_A (N_D - N_i)}{N_A (N_A + N_D)} + \frac{\sqrt{N_D N_A \left[\frac{2\epsilon_0\epsilon_r (V_{Ref} - E_{Pol} x_d) (N_A + N_D)}{q} - (N_i + N_A) (N_i - N_D) x_i^2 \right]}}{N_A (N_A + N_D)}. \quad (4.6)$$

Consequently, the polarization-induced charges are compensated by the change in the depletion region width x_p and x_n . The sum $x_n + x_p + x_i$ is the width of the whole depletion region

$$d = \left\{ \frac{2\epsilon_0\epsilon_r}{q} \left(V_{Ref} - V - E_{Pol} x_d - \frac{2k_B T}{q} \right) \cdot \left(\frac{1}{N_D} + \frac{1}{N_A} \right) + \frac{(N_D - N_i)(N_A + N_i)}{N_A N_D} x_i^2 \right\}^{1/2}, \quad (4.7)$$

where T is the temperature, k_B is the Boltzmann constant and V is an additional

external bias voltage. The correction factor $2k_B T/q$ arises from the contribution of the majority-carrier distribution tail. It is worth noting that with the exception of the correction factor, Eq. 4.7 assumes that all donors and acceptors in the depletion region are ionized. The factor $(N_D - N_i)(N_A + N_i)/N_A N_D$ in Eq. 4.7 describes the influence of an n -type background doping concentration N_i . The background doping concentration of the samples is in the range of $N_i = 5 \times 10^{16} \text{ cm}^{-3}$ (measured by secondary ion mass spectrometry, Evans Analytical Group [151]). Since this is smaller than the typical n - and p -side doping concentration, the influence of the background doping concentration on the width of the depletion region is small. The depletion region width d in Eq. 4.7 can be determined by measuring the capacitance C assuming that the pin -junction can be described as a parallel plate capacitor

$$C = \frac{\epsilon_0 \epsilon_r A}{d}, \quad (4.8)$$

where A describes the area of the equivalent capacitor given by the mesa area. By measuring the capacitance at different voltages, the doping concentration $\frac{1}{N_D} + \frac{1}{N_A}$ in Eq. 4.7 can be calculated. Furthermore, the n -doping concentration N_D can be determined from the voltage derivative of the capacitance-voltage measurement, since $N_A \gg N_D$

$$N_D = - \left[\frac{q \epsilon_0 \epsilon_r A^2}{2} \frac{\partial}{\partial V} \left(\frac{1}{C^2} \right) + \frac{1}{N_A} \right]^{-1}. \quad (4.9)$$

When evaluating the capacitance-voltage measurements using Eq. 4.7, it is not possible to distinguish between the reference potential V_{Ref} and the polarization term $E_{Pol} x_d$ since the reference potential V_{Ref} differs from the built-in potential V_{bi} . Only the sum of both can be determined. In order to calculate the reference potential V_{Ref} and to finally extract the polarization term $E_{Pol} x_d$ in Eq. 4.7, an additional homojunction reference sample with same layer thicknesses and doping concentrations is required. In the homojunction reference sample, the polarization influenced layer (i.e. the double heterostructure) is replaced by the matrix material with the same thickness. The analytic expression of the depletion region width of the homojunction reference sample is identical to Eq. 4.7 except for the omission of the polarization term $E_{Pol} x_d$. Using Eq. 4.7 and 4.8 for the reference sample and the sample under investigation, the polarization field E_{Pol} and the reference potential \widetilde{V}_{Ref} can be calculated, respectively

$$E_{Pol} = \frac{1}{x_d} \left\{ \widetilde{V}_{Ref} - V - \frac{2k_B T}{q} - \left(\frac{\partial}{\partial V} \frac{1}{C^2} \right)^{-1} \cdot \left(\frac{x_i^2}{\epsilon_0^2 \epsilon_r^2 A^2} \cdot \frac{(N_D - N_i)(N_A + N_i)}{N_A N_D} - \frac{1}{C^2} \right) \right\}, \quad (4.10)$$

where

$$\widetilde{V}_{Ref} = V + \frac{2k_B \widetilde{T}}{q} + \left(\frac{\partial}{\partial V} \frac{1}{\widetilde{C}^2} \right)^{-1} \cdot \left(\frac{\widetilde{x}_i^2}{\epsilon_0^2 \widetilde{\epsilon}_r^2 \widetilde{A}^2} \cdot \frac{(\widetilde{N}_D - \widetilde{N}_i)(\widetilde{N}_A + \widetilde{N}_i)}{\widetilde{N}_A \widetilde{N}_D} - \frac{1}{\widetilde{C}^2} \right). \quad (4.11)$$

Values with a tilde symbol correspond to values of the reference structure. Consequently, the polarization field can be analytically evaluated by measuring the capacitance of the reference sample and the sample under investigation at different voltages. Nevertheless, for a precise determination, the reference sample and the heterostructure sample require the same doping levels and layer structure. Otherwise, the widths of the depletion regions are not comparable and the measurement error increases, as will be discussed in the next section.

4.1.2 Accuracy analysis

In principal, errors can be caused by deviations of the sample structure from the nominal structure, for example if caused by growth or process deviations between the *pin*-diodes. In order to evaluate the influence of each parameter in Eq. 4.10, each error is varied from 0% up to +50% while all the other errors and parameters stayed constant at a chosen value, using the Gaussian error propagation. The error, here determined for an $\text{Al}_{0.41}\text{Ga}_{0.59}\text{N}$ *pin*-diode (see section 4.6), of the polarization field in dependence of every parameter in Eq. 4.10 is shown in Fig. 4.2(a). Note that in the following sections the relative errors given in the table in Fig. 4.2(b) are used. With these assumed errors the relative error of the polarization field is 14%. It should be noted that the relative error of N_D is assumed to be less than the relative error of N_A , since N_D is calculated by Eq. 4.9. The relative error of the capacitances (\widetilde{C} , C), the slope of the capacitances ($\partial/\partial V \widetilde{C}^{-2}$, $\partial/\partial V C^{-2}$) and the thickness of the layer of interest (x_d) have a huge impact on the accuracy of the polarization field determination, whereas the other parameters have a negligible impact even up to 50% relative error. In order to minimize the error of the polarization field determination,

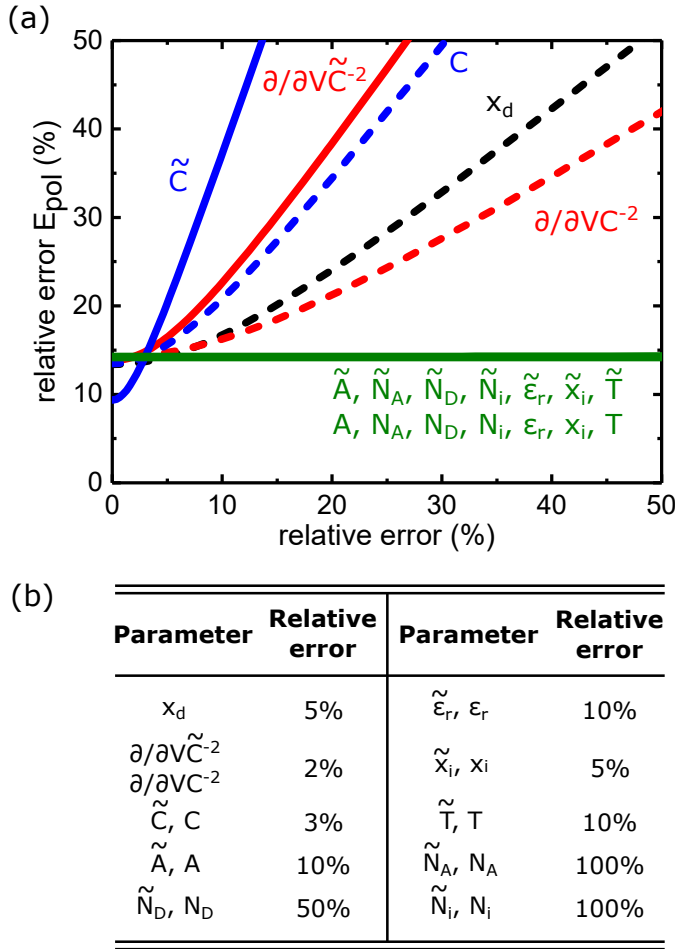


Figure 4.2: (a) Relative error of the polarization field determined by Gaussian error propagation as a function of the relative error of each parameter in Eq. 4.10. Dashed lines correspond to parameters of the sample under investigation and solid lines to parameters of the reference sample. (b) Estimated relative errors of the parameters in Eq. 4.10. Values with a tilde symbol correspond to values of the reference structure.

the thickness of the layers of interest were determined by TEM. Furthermore, an advanced equivalent circuit model for the capacitance determination was developed, quantified and used for an accurate determination of the capacitance.

4.1.3 Advanced capacitance-voltage-profiling

It should be noted that the *pin*-diodes used for the polarization field determination do not represent an ideal capacitor. The *pin*-diodes have a series resistance that result from the contact and the sheet resistances as well as a finite parallel resistance caused by leakage currents via impurity transport or leakage paths along defects, drift and diffusion in forward bias and thermal charge carrier generation in the depletion region in reverse bias. In this thesis, an equivalent circuit directly related to the sample structure has been used and compared to common equivalent circuit models of a LCR Meter. Most LCR Meters have two capacitance measurement methods, namely the $C_S R_S$ and the $C_P R_P$ model. The $C_P R_P$ model assumes a resistor connected parallel to the capacitor and

neglects all series resistors and the $C_S R_S$ model assumes a resistor connected in series to the capacitor and neglects all parallel resistors. Assuming a series resistance R_S as well as a parallel resistance R_P in the equivalent circuit to the capacitance C of the *pin*-diode, the impedance Z can be expressed as:

$$Z = R_S + \left(\frac{1}{R_P} + i \cdot 2\pi f C \right)^{-1}, \quad (4.12)$$

where f is the frequency and i the imaginary unit. Note, that the imaginary part of Eq. 4.12 is independent of the series resistance R_S :

$$\Im(Z) = -\frac{2\pi f C}{R_P^{-2} + 4\pi^2 f^2 C^2}. \quad (4.13)$$

Eliminating the parallel resistance terms using the first order derivative of Eq. 4.13 with respect to the frequency f results in

$$C = \frac{\frac{\partial}{\partial f} \frac{-f}{2\pi \Im(Z)}}{\frac{\partial}{\partial f} f^2}, \quad (4.14)$$

where the imaginary part $\Im(Z) = |Z| \cdot \sin(\Phi)$ is given by the absolute value of the impedance $|Z|$ and the phase shift Φ . In order to estimate the accuracy of the capacitance determination, networks of single resistors and capacitors were measured and compared to the measurement values of the single capacitors. The circuit has been chosen to be similar to the equivalent circuit of the *pin*-diode. According to this, capacitances in the pF range, series resistances in the Ω range and parallel resistances in the M Ω range were used. The capacitances were determined by Eq. 4.14 and compared to the built-in models of a Keysight E4980A Precision LCR-Meter. Figure 4.3 shows the deviation of the determined capacitance from the measured value of the single capacitor ($C = 22$ pF) using the built-in models of the LCR and Eq. 4.14 as a function of the frequency for a *pin*-diode-like circuit. The measured value of the single capacitor showed an identical value as the specified capacitance, regardless of the model and frequency used. The $C_P R_P$ model and the $C_S R_S$ model show similar deviations of about 2.25%. The capacitance determined by Eq. 4.14 exhibits the smallest deviation with an average error of 1% over the entire frequency range. In order to make statistical statements about the accuracy of the models, 70 different circuits with different capacitors and resistors were measured. As in Fig. 4.3, the

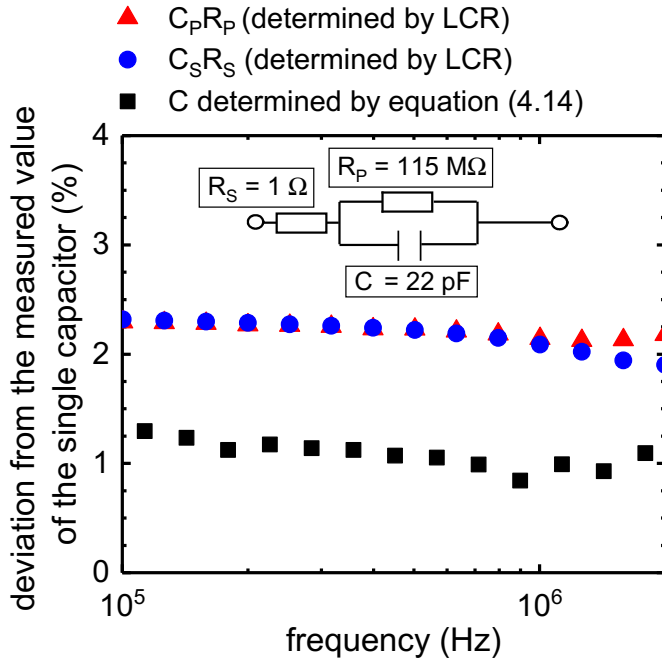


Figure 4.3: Deviation of the determined capacitance from the measured value of the single capacitor ($C = 22 \text{ pF}$) using the built-in $C_P R_P$ model (red), built-in $C_S R_S$ model (blue) and Eq. 4.14 (black) for a *pin*-diode-like circuit. The capacitance determined by Eq. 4.14 exhibits the smallest deviation.

evaluation of the capacitance by Eq. 4.14 is most accurate in all cases where the electrical circuit is similar to the equivalent circuit of a *pin*-diode. Accordingly, in this work, Eq. 4.14 is used to determine the capacitance in Eq. 4.10 and the relative error is estimated to be below 3%.

4.2 CVM-based Poisson-carrier transport simulation approach

It should be noted that Eq. 4.10 contains several simplifications, such as the screening of the polarization field by free carriers and the discontinuity of the relative permittivity. An alternative polarization field determination approach, that overcomes these simplifications, can be achieved by fitting the experimental CVM with a coupled Poisson/carrier transport simulation of the entire *pin*-diode¹. This approach is based on a small signal method and uses a 2-dimensional simulation. Incomplete acceptor ionization was included using an acceptor ionization model as presented in Ref. [152]. Note that the incomplete acceptor ionization has no effect on the junction capacitance since the carrier depletion completely ionizes the acceptors within the depletion region. The acceptors are considered to be incompletely ionized only outside of the depletion region. The

¹Simulations were performed by B. Witzigmann, CEP Kassel.

layer structure is discretized in space and the doping concentrations as well as the polarization charges n_{2D} are used as adjustable parameters of the model. The polarization field can be calculated from the interface charges n_{2D} by

$$E_{Pol} = \frac{n_{2D}q}{\epsilon_0\epsilon_r}. \quad (4.15)$$

The main advantage of the CVM-based coupled Poisson-carrier transport simulation is that no reference sample is required, and the CV curves are determined based on the epitaxial layer structure. A detailed description of the simulation approach can be found in Ref. [40]. It should be noted that for the simulation approach an error determination was not possible. However, similar errors to those described in the section 4.1.2 are expected since this approach is also based on the accuracy of the CVM and the heterostructure thickness.

4.3 Polarization fields predicted by DFT calculations

Since experimental determination of the internal polarization field is usually difficult, first-principle density-functional theory (DFT) calculations for the spontaneous and piezoelectric polarization constants are widely used. The internal polarization fields in GaN/ $X_xY_{1-x}N$ /GaN double heterostructures grown in the c -direction (see section 1.3 for more details) are given by

$$E_{Pol} = \frac{e}{\epsilon_0\epsilon_r} \left(\Delta P_{sp} - 2\epsilon_1^{XYN} \left(e_{31}^{XYN} - e_{33}^{XYN} \frac{C_{13}^{XYN}}{C_{33}^{XYN}} \right) + \right. \\ \left. + 2\epsilon_1^{GaN} \left(e_{31}^{GaN} - e_{33}^{GaN} \frac{C_{13}^{GaN}}{C_{33}^{GaN}} \right) \right), \quad (4.16)$$

where

$$\epsilon_1 = \frac{a - a_0}{a_0}, \quad (4.17)$$

is the relative change of the lattice constant a with respect to the lattice constant of the relaxed crystal a_0 . C_{ij} are the elastic constants and e is the elementary charge. The second term in Eq. 4.16 describes the contribution of the

Material parameter	AlN	InN	GaN
a	3.103	3.560	3.189
ϵ_r	9.21	15.3	10.04
C_{13}	108	92	106
C_{33}	373	224	398
e_{31}^*	-2.027	-1.63	-1.863
e_{31}	-0.53	-0.41	-0.34
e_{33}^*	1.569	1.238	1.020
e_{33}	1.5	0.81	0.67
P_{sp}^*	1.351	1.026	1.312
P_{sp}	-0.09	-0.042	-0.034

Table 4.1: Lattice constants a in units of \AA [46], relative permittivity ϵ_r [154, 155], elastic constants C_{ij} in units of GPa [54], piezoelectric polarization constants e_{ij} in units of C/m^2 [46] and effective spontaneous polarization constants P_{sp} in units of C/m^2 [46]. Values with an asterisk are taken from Dreyer et al. [45].

piezoelectric polarization of the GaN matrix. Both the spontaneous polarization constants P_{sp} and piezoelectric polarization constants e_{31} and e_{33} given in the literature show considerable scattering [44, 45]. In particular, the choice of the so-called proper and improper piezoelectric polarization constants [49, 50] as well as the choice of the reference structure for the calculation of the spontaneous polarization constants [45, 153] is discussed. In this work values recommended by Ambacher et al. [46], i.e. using the zincblende reference structure and the proper piezoelectric constants as well as Dreyer et al. [45], i.e. using the layered hexagonal reference structure and the improper piezoelectric constants, are compared. The corresponding material parameters for AlN, InN and GaN are listed in Table 4.1 and were linearly interpolated for ternary compounds. However, for the values published by Ambacher et al. a bowing parameter of the spontaneous polarization constants between AlN and GaN of $b = 0.021$ as well as InN and AlN of $b = 0.070$ is assumed [46].

4.4 Sample structure of the pin-diodes

The scope of this chapter is to determine the internal polarization fields of III-nitride double heterostructures. Therefore, *pin*-diodes were grown on (0001) sapphire by MOVPE. The layer structure was chosen to allow ohmic *n*- and *p*-contacts as well as avoid additional heterointerfaces (especially within the depletion region). The layer structure is illustrated in Fig. 4.4. On top of a GaN-based buffer layer on the (0001) sapphire substrate, a 200-nm-thick n^+

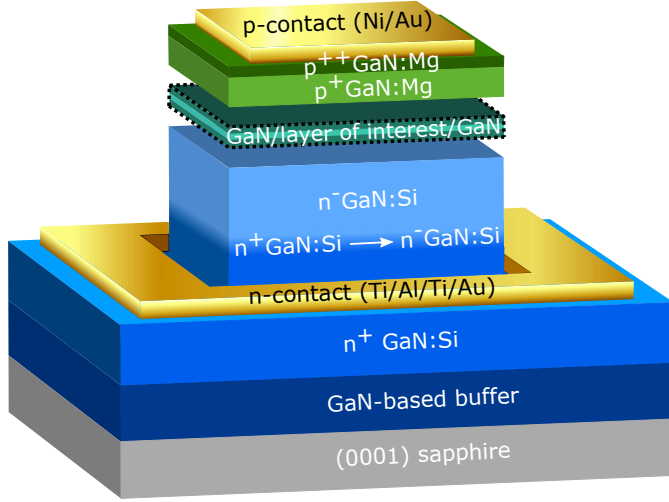


Figure 4.4: Schematic sample structure of the GaN-based *pin*-diodes grown on (0001) sapphire.

GaN:Si current spreading layer with a nominal Si-doping level of $3 \times 10^{18} \text{ cm}^{-3}$ was deposited followed by a 100-nm-thick GaN:Si layer with a graded n -doping concentration down to $1 \times 10^{17} \text{ cm}^{-3}$ and a 400-nm-thick low doped n^- GaN:Si layer with a Si-concentration of $1 \times 10^{17} \text{ cm}^{-3}$. The low Si-doping concentration of $1 \times 10^{17} \text{ cm}^{-3}$ was chosen to increase the depletion region width (Eq. 4.7) and therefore to increase the effect of the polarization charges on the capacitance C , since the capacitance is inverse proportional to the depletion region width (Eq. 4.8). It should be noted that due to the low Si-doping concentration, N_D approaches the background doping concentration of the intrinsic region N_i . However, Eq. 4.10 also considers the background doping concentration of the intrinsic region N_i . Since a high n -doping concentration is required for ohmic metal contacts, the contact layer was highly doped.

The layer of interest with thicknesses between 4 nm and 5 nm (see section 4.5 and section 4.6 for exact layer thicknesses) within the intrinsic double heterostructure is sandwiched between two GaN layers with layer thicknesses of 10 nm. It is worth mentioning that if the layer of interest is too thick, the Fermi-level could cross the valance or conduction band due to the heterostructure- and polarization-induced band bending. The generated carriers would affect the junction capacitance, making the polarization field determination impossible. However, if the layer of interest is too thin, small growth inaccuracies and growth fluctuations have a strong influence on the polarization field evaluation.

Finally the heterostructure was capped by a 150-nm-thick p^+ GaN:Mg layer with a nominal Mg-concentration of $8 \times 10^{18} \text{ cm}^{-3}$ and a 10-nm-thick p^{++} GaN:Mg contact layer. After epitaxial layer growth, the *pin*-diodes were fabricated by

standard lithography and metallization techniques using Ni/Au as p -contacts and Ti/Al/Ti/Au as n -contacts². The CVM were performed on $196 \times 196 \mu\text{m}^2$ p -contacts.

In order to compare the polarization fields evaluated by the CVM-based analytical and the coupled Poisson-carrier transport simulation approach with the values predicted by density functional theory [45, 46], the lattice constant of the GaN matrix is determined in Eq. 4.3. The different thermal expansion coefficients of GaN and sapphire lead to a compressive strain in the GaN matrix at room temperature [156–158]. This strain contributes to the piezoelectric polarization of the GaN matrix. The a - and c -lattice constant of the GaN matrix were measured by HRXRD. Based on Frentrup et al. [159], several reflections were measured in symmetric and skew-symmetric geometry and the lattice constants were calculated accordingly. The a - and c -lattice constant was determined to be $a_{\text{GaN}}^{\text{Matrix}} = (3.18537 \pm 0.00036) \text{ \AA}$ and $c_{\text{GaN}}^{\text{Matrix}} = (5.18778 \pm 0.00016) \text{ \AA}$, respectively³.

4.5 Spontaneous polarization field determination in InAlN/GaN

The remarkable property of $\text{In}_x\text{Al}_{1-x}\text{N}/\text{GaN}$ heterostructures is that they can be grown lattice matched for In mole fractions of $x \approx 0.18$ [160–162]. Such a lattice matched InAlN/GaN heterostructure exhibits a vanishing piezoelectric polarization due to the absence of strain in the basal plane (see Eq. 1.7). Nevertheless, a strong total polarization field occurs in lattice matched InAlN/GaN heterostructures because of large differences in the spontaneous polarization coefficients between InAlN and GaN [46, 163]. Accordingly, lattice matched InAlN/GaN heterostructures are ideally suited to determine the spontaneous polarization field independently of the piezoelectric polarization. Since the generated spontaneous polarization field depends on both the InAlN layer and the GaN matrix, the chosen sample structure allows insight into the spontaneous polarization coefficients of all three ternary compounds, i.e. InN, AlN and GaN. Furthermore, an optical bandgap of 4.2 eV is expected for $\text{In}_{0.18}\text{Al}_{0.82}\text{N}$ layers, which in principle allows UV-emission at a wavelength of 295 nm [164]. In particular, Pampili et al. [165] recently reported on the fabrication of an

²The micro-fabrication process was performed by M. Rychetsky, TUB.

³Measurements were performed by J. Enslin, TUB.

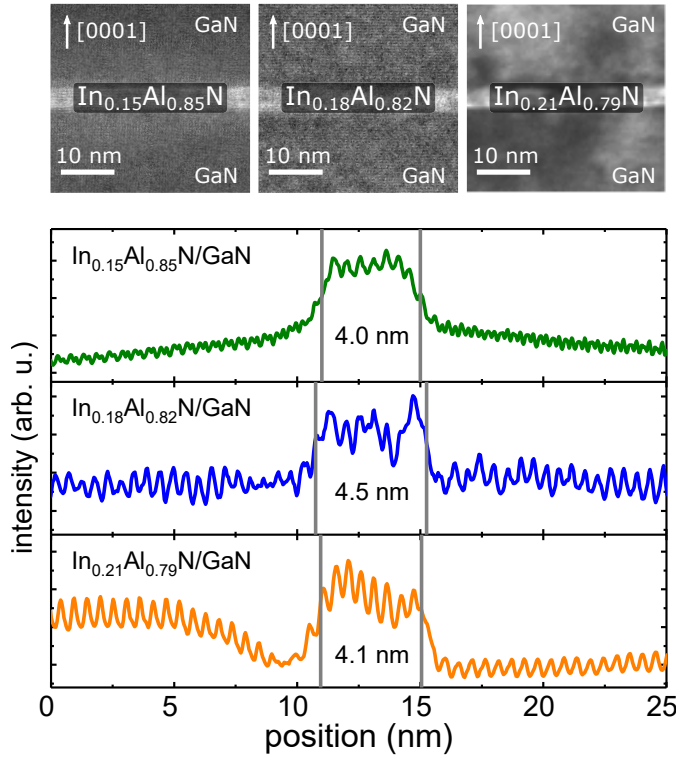


Figure 4.5: Cross-sectional TEM images of the InAlN layers in a GaN matrix. The line-scans are recorded along the $[0001]$ growth direction. Measurements performed by M. Narodovitch, TUB.

operational UV-LED using $\text{In}_{0.14}\text{Al}_{0.86}\text{N}$ MQWs. If the polarization constants in such UV-LED devices are known, a polarization-matched heterostructure with reduced or no QCSE can be designed.

To determine the spontaneous polarization field three *pin*-diodes (with the sample structure described in section 4.4) containing 4-nm $\text{In}_x\text{Al}_{1-x}\text{N}$ layers with In mole fractions close to 18% ($\text{In}_{0.15}\text{Al}_{0.85}\text{N}$, $\text{In}_{0.18}\text{Al}_{0.82}\text{N}$ and $\text{In}_{0.21}\text{Al}_{0.79}\text{N}$) were grown on (0001) sapphire by MOVPE [166]⁴. The In mole fraction was varied by adjusting the growth temperature and determined by HRXRD ω - 2θ measurements close to the symmetric (0002) GaN reflection on calibration samples. In addition, a reference homojunction sample with a GaN layer instead of $\text{In}_x\text{Al}_{1-x}\text{N}$ of the same thickness was grown. To minimize the error of the polarization field determination (see section 4.1.2), the thickness of the $\text{In}_x\text{Al}_{1-x}\text{N}$ layers were determined by several line-scans performed along the $[0001]$ direction as shown in the lower part of Fig. 4.5. The intensity varies over 2-3 monolayers at the InAlN/GaN interfaces indicating a gradual change of the In mole fraction along the growth direction. The layer thickness was obtained by considering the

⁴MOVPE growth performed by S. Neugebauer, OVGU.

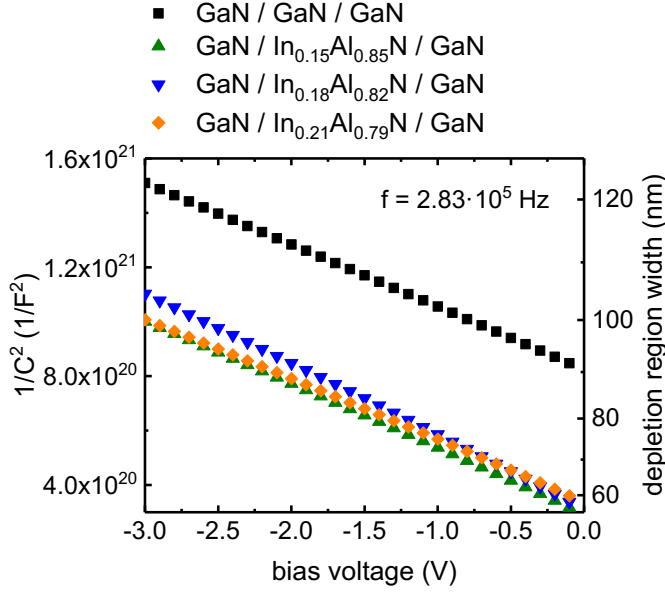


Figure 4.6: C^{-2} and depletion region width as a function of the reverse bias voltage of the reference *pin*-diode (black) and the *pin*-diodes containing a GaN/InAlN/GaN double heterostructure. The polarization fields lead to a significant reduction in the width of the depletion region. Measurements performed together with G. Roumeliotis, TUB.

FWHM, as marked in the line-scans. Accordingly, layer thicknesses of (4.0 ± 0.3) nm, (4.5 ± 0.3) nm and (4.1 ± 0.3) nm for the $\text{In}_{0.15}\text{Al}_{0.85}\text{N}$, $\text{In}_{0.18}\text{Al}_{0.82}\text{N}$, and the $\text{In}_{0.21}\text{Al}_{0.79}\text{N}$ *pin*-diodes were determined, respectively.

In order to determine the polarization field with Eq. 4.10, the capacitance must be evaluated as a function of the reverse bias voltage (Fig. 4.6). It is worth noting here that the capacitance at each individual voltage in Fig. 4.6 is calculated by Eq. 4.14. However, the differential quotient is replaced by the difference quotient between the frequencies 250 kHz and 315 kHz, resulting in an average frequency of 283 kHz. The three *pin*-diodes with an $\text{In}_x\text{Al}_{1-x}\text{N}/\text{GaN}$ double heterostructure show larger capacitances compared to the reference *pin*-diode at each applied reverse bias voltage, which is associated with a reduction of the depletion region width (see Eq. 4.8) of about 30 nm. This is in agreement with the expected positive polarization field direction (see Eq. 4.7). The linearity of the curves in Fig. 4.6 indicates a constant effective doping concentration $N_{eff} = (N_D^{-1} + N_A^{-1})^{-1}$. The reference *pin*-diode ($4.3 \times 10^{17} \text{ cm}^{-3}$) has similar effective doping concentrations to the *pin*-diode with an $\text{In}_{0.15}\text{Al}_{0.85}\text{N}$ layer ($3.9 \times 10^{17} \text{ cm}^{-3}$) and an $\text{In}_{0.21}\text{Al}_{0.79}\text{N}$ layer ($4.2 \times 10^{17} \text{ cm}^{-3}$). However, the $\text{In}_{0.18}\text{Al}_{0.82}\text{N}$ *pin*-diode has a slightly lower effective doping concentration of $3.4 \times 10^{17} \text{ cm}^{-3}$ leading to a larger slope of the CVM curve in Fig. 4.6. Accordingly, the determination of the polarization field with Eq. 4.10 for the *pin*-diode with an $\text{In}_{0.18}\text{Al}_{0.82}\text{N}$ layer exhibits a slightly larger error. Note that the difference in the effective doping concentration has no effect on the precision of the determination method using the coupled Poisson/carrier transport simulation approach.

In order to determine the internal polarization fields using Eq. 4.10, the reference potential \widetilde{V}_{Ref} is required. The reference potential \widetilde{V}_{Ref} was determined from Eq. 4.11 using the CVM of the reference sample (black squares in Fig. 4.6), i.e. the *pin*-diode without heterostructure. The reference potential was evaluated at a DC voltage of 0 V, a temperature of 298 K and an unintentionally *n*-type doping of $5 \times 10^{16} \text{ cm}^{-3}$. The reference potential was determined to be $(3.28 \pm 0.22) \text{ eV}$ and used to solve the polarization field Eq. 4.10. It is worth noting that this value is very close to the expected built-in potential of GaN as described in section 4.1.1.

In Fig. 4.7, the internal polarization fields evaluated using both methods (Eq. 4.10 and Poisson/carrier transport simulations) are illustrated. The polarization fields using Eq. 4.10 were determined using the CVM shown in Fig. 4.6, a DC voltage of 0 V, a temperature of 298 K and an unintentional *n*-doping concentration of $5 \times 10^{16} \text{ cm}^{-3}$. Both evaluation methods yield the correct positive polarization field directions. The error bars in Fig. 4.7 correspond to the Gaussian error propagation of all parameters in Eq. 4.10 (see section 4.1.2). In addition, Fig. 4.10 shows the polarization sheet charges calculated using a simple parallel-plate capacitor model ($E = ne/(\epsilon_0\epsilon_r)$) with a relative dielectric constant for InN of 15.30 [167], for AlN of 9.21 [154] and a linear interpolation for $\text{In}_x\text{Al}_{1-x}\text{N}$. The CVM-based analytical approach using the Eq. 4.10 reveals high polarization fields for $\text{In}_{0.15}\text{Al}_{0.85}\text{N}$ ($5.9 \pm 0.8 \text{ MV/cm}$), $\text{In}_{0.18}\text{Al}_{0.82}\text{N}$ ($5.4 \pm 0.9 \text{ MV/cm}$), and $\text{In}_{0.21}\text{Al}_{0.79}\text{N}$ ($5.1 \pm 0.8 \text{ MV/cm}$). The internal polarization fields evaluated by the CVM-based Poisson/carrier transport simulation approach for $\text{In}_{0.15}\text{Al}_{0.85}\text{N}$ (6.2 MV/cm), $\text{In}_{0.18}\text{Al}_{0.82}\text{N}$ (5.5 MV/cm), and $\text{In}_{0.21}\text{Al}_{0.79}\text{N}$ (5.3 MV/cm) show agreement with the CVM-based analytical approach. The orange solid line in Fig. 4.7 shows the values predicted by Dreyer et al. [45], using the layered hexagonal reference structure, the improper piezoelectric constants and the elastic constants from Vurgaftman et al. [54]. The green dashed line in Fig. 4.7 shows the internal polarization field based on Ambacher et al. [46] using the piezoelectric constants and elastic constants from Zoroddu et al. [168] and Bernardini et al. [37] (see section 4.3). In addition, the spontaneous polarization and piezoelectric polarization field based on Ambacher et al. is shown indicating a vanishing piezoelectric polarization field at an In mole fraction of 0.18. The theoretically predicted and measured values show the same trend with overlapping confidence intervals. Since the total polarization field in the selected In mole fraction range is mainly determined by the spontaneous polarization field (see Fig. 4.7), the

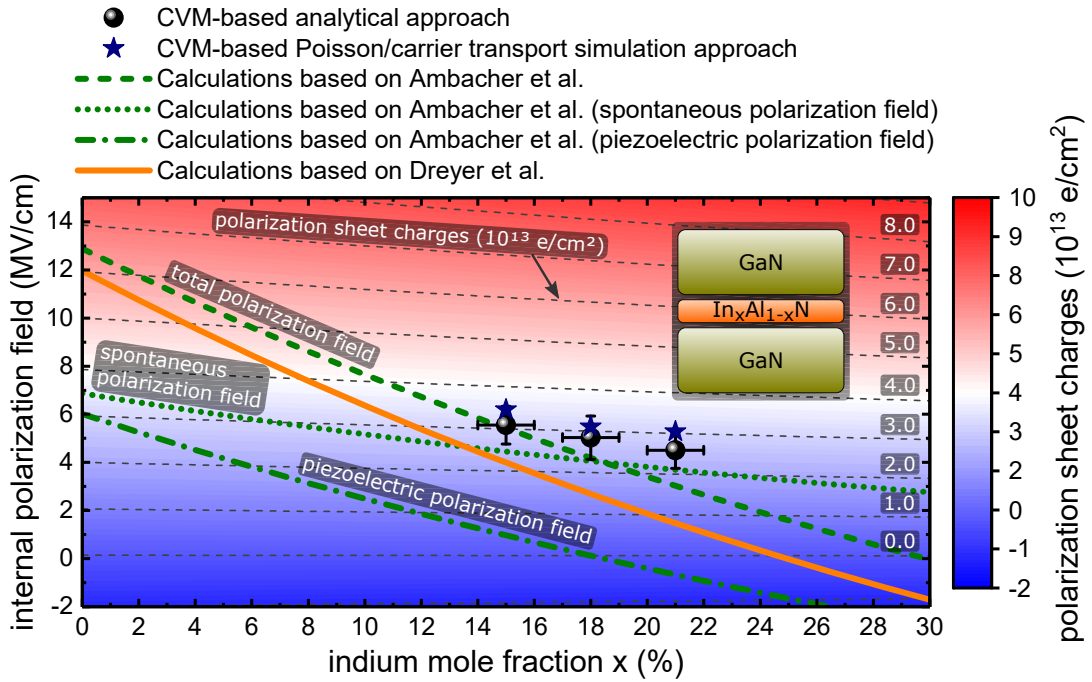


Figure 4.7: Internal polarization fields determined with the CVM-based analytical approach (black dots) and the CVM-based Poisson/carrier transport simulation approach (blue stars). In addition, theoretically predicted values by Ambacher et al. [46] and Dreyer et al. [45] are shown. The internal polarization fields were converted to polarization sheet charges using a simple parallel-plate capacitor model.

CVM-based approaches indicate similar spontaneous polarization coefficients as the theoretical predictions of the three ternary compounds InN, AlN and GaN given in Table 4.1. However, most experimental studies on polarization fields show an underestimation of the internal polarization field strength compared to the theoretical predictions. For lattice-matched InAlN/GaN heterostructures, values between 2.5 MV/cm and 3.0 MV/cm are published [46, 169]. A detailed discussion of the experimentally determined internal polarization fields presented in the literature can be found in the next section.

4.6 Polarization field determination in AlGaN/GaN

In addition to the spontaneous polarizations, piezoelectric polarizations occur in AlGaN/GaN heterostructures leading to strong polarization fields in the order of MV/cm [45, 46]. To understand the carrier transport and recombination in AlGaN semiconductors, a precise determination of the polarization fields is of great importance. Consequently *pin*-diode heterostructures (sample structure

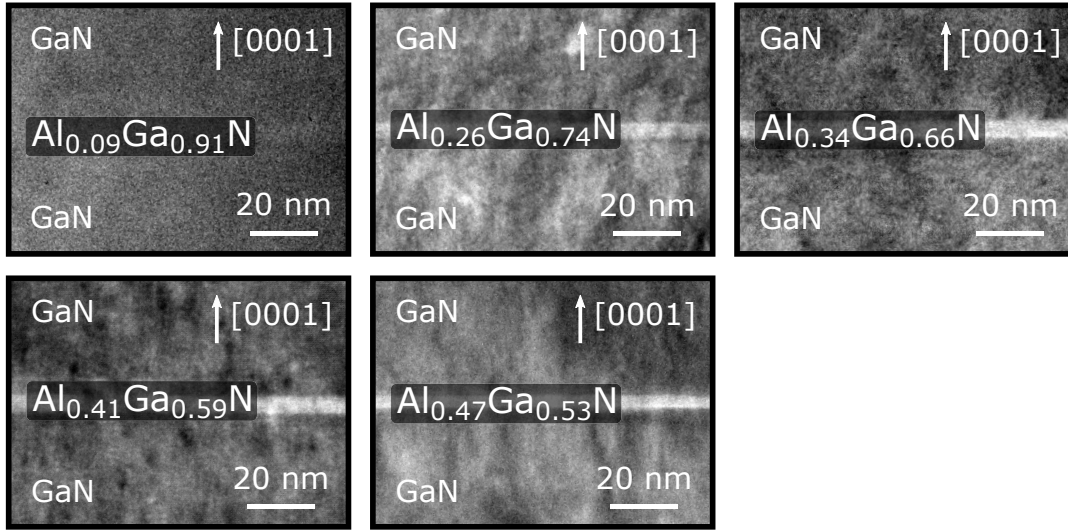


Figure 4.8: Cross-sectional TEM images of the GaN/ $\text{Al}_x\text{Ga}_{1-x}\text{N}$ /GaN double heterostructures with different Al mole fractions x . Measurements performed by M. Narodovitch, TUB.

described in section 4.4) containing a nominal 5-nm-thick $\text{Al}_x\text{Ga}_{1-x}\text{N}$ layer were grown on c -plane sapphire substrates⁵. The Al mole fraction x was varied between $x = 0.09$ and $x = 0.47$. In addition, a reference sample with a GaN layer instead of $\text{Al}_x\text{Ga}_{1-x}\text{N}$ was grown. The Al mole fraction was determined by HRXRD ω - 2θ measurements close to the symmetric (0002) GaN reflection on calibration samples. In order to increase the precision of the polarization field determination, the thicknesses of the $\text{Al}_x\text{Ga}_{1-x}\text{N}$ layers were determined by cross-sectional TEM (Fig. 4.8). Several line-scans along the [0001] direction were performed. Average thicknesses of (4.5 ± 0.5) nm ($\text{Al}_{0.09}\text{Ga}_{0.91}\text{N}$), (5.3 ± 0.3) nm ($\text{Al}_{0.26}\text{Ga}_{0.74}\text{N}$), (5.2 ± 0.3) nm ($\text{Al}_{0.34}\text{Ga}_{0.66}\text{N}$), (5.2 ± 0.3) nm ($\text{Al}_{0.41}\text{Ga}_{0.59}\text{N}$), and (4.6 ± 0.2) nm ($\text{Al}_{0.47}\text{Ga}_{0.53}\text{N}$) were determined. The TEM results for x_d , were used to calculate the internal polarization field assuming an error of 5% and 10% for the $\text{Al}_{0.09}\text{Ga}_{0.91}\text{N}$ /GaN sample due to the low intensity contrast. In order to determine the polarization fields with Eq. 4.10, the reference potential \widetilde{V}_{Ref} is required using the CVM of the reference sample. To reduce the error of a single measurement, 50 *pin*-diodes were evaluated across the wafer. The reference potential was determined at a DC voltage of 0 V, a temperature of 298 K and an unintentionally n -type doping of $5 \times 10^{16} \text{ cm}^{-3}$. Figure 4.9 shows the reference potential as a function of the position on the quarter wafer. The reference potential was determined to be (3.88 ± 0.26) eV with a standard deviation of ± 0.16 . The error was estimated by the Gaussian error propagation as described

⁵MOVPE growth performed by I. Koslow, FBH.

in section 4.1.2. It is worth noting here that the reference potential \widetilde{V}_{Ref} does not reflect the built-in potential and is only used to determine the internal polarization fields, as discussed in section 4.1.1. For each sample, the internal polarization fields of 50 *pin*-diodes were determined using \widetilde{V}_{Ref} and Eq. 4.10. The maps shown in Fig. 4.9 reveal that the *pin*-diodes at the edges have slightly lower values for the polarization field compared to the *pin*-diodes in the center of the wafer. At the wafer edge inhomogeneities during the growth of the samples lead to a deviation of the heterostructure [170] i.e. layer thickness, composition and doping, which affects the capacitance of these diodes and the determined polarization fields. Accordingly, *pin*-diodes close to the wafer edge (marked in gray in Fig. 4.9) were excluded from further evaluations. From the remaining *pin*-diodes the average value of the polarization field was determined with the corresponding average errors:

$$E_{Pol}(\text{Al}_{0.09}\text{Ga}_{0.91}\text{N}) = (0.6 \pm 0.7) \text{ MV/cm}$$

$$E_{Pol}(\text{Al}_{0.26}\text{Ga}_{0.74}\text{N}) = (2.3 \pm 0.6) \text{ MV/cm}$$

$$E_{Pol}(\text{Al}_{0.34}\text{Ga}_{0.66}\text{N}) = (3.1 \pm 0.6) \text{ MV/cm}$$

$$E_{Pol}(\text{Al}_{0.41}\text{Ga}_{0.59}\text{N}) = (4.0 \pm 0.7) \text{ MV/cm}$$

$$E_{Pol}(\text{Al}_{0.47}\text{Ga}_{0.53}\text{N}) = (5.0 \pm 0.8) \text{ MV/cm}$$

Figure 4.10 shows the internal polarization field and polarization sheet charges as a function of the Al mole fraction in the double heterostructure. The black error bars are determined by the Gaussian error propagation and the red errors indicate the standard deviation. The polarization sheet charges are calculated using a simple parallel-plate capacitor model with a relative dielectric constant for AlN of 9.21 [154] and for GaN of 10.04 [155] and a linear interpolation for Al_xGa_{1-x}N. Additionally, Fig. 4.10 shows the internal polarization field determined by the CVM-based coupled Poisson-carrier transport simulation (blue stars). Both approaches are consistent and reveal the same trend with overlapping confidence intervals. However, the CVM-based Poisson-carrier transport simulation approach shows lower internal polarization fields for Al mole fractions of more than 9%. Here, further investigation is necessary to quantify the possible influence of non-abrupt doping profiles and parasitic capacitances on the determined polarization fields by the two methods. The

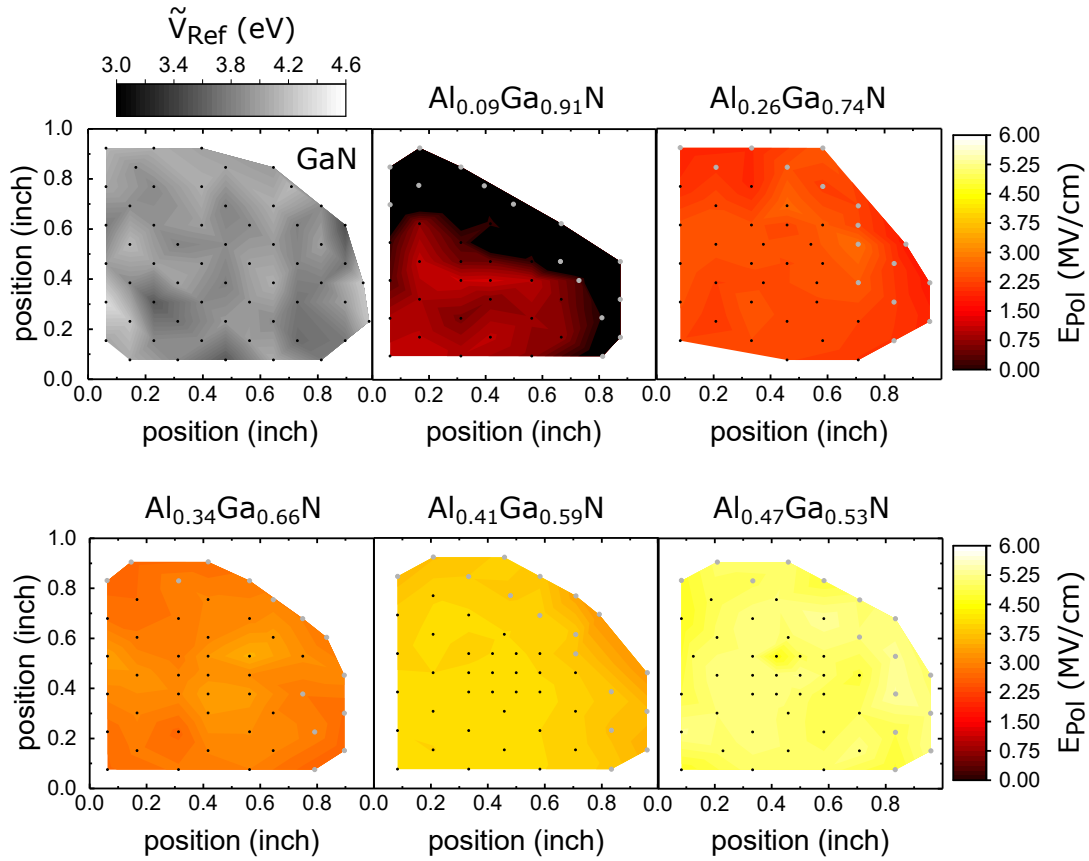


Figure 4.9: Reference potential and internal polarization fields of the *pin*-diodes with different Al mole fraction as a function of the position on a quarter wafer. The dots are the location of the measured *pin*-diode. The *pin*-diodes close to the wafer edge (marked in gray) were excluded from further evaluations. Measurements performed together with M. Schilling, TUB.

analytical model is expected to be robust to effects that uniformly increase the capacitance in the reference and heterostructure *pin*-diode since they cancel each other out when added in Eq. 4.10 and Eq. 4.11.

The orange solid line in Fig. 4.10 shows the implementation recommended by Dreyer et al. [45], i.e., using the layered hexagonal reference structure, the improper piezoelectric constants and the elastic constants from Vurgaftman et al. [54]. Quantities for alloys were obtained using linear interpolation, however with the experimentally measured lattice constants for strain free GaN and AlN and the strained GaN matrix (see section 4.3). The green dashed line in Fig. 4.10 shows the internal polarization field based on Ambacher et al. [46] using the piezoelectric constants and elastic constants from Zoroddu et al. [168] and Bernardini et al. [37]. Similarly as before, the internal polarization fields were converted into polarization sheet charges using a simple parallel plate capacitor model. The results show that the internal field direction and strength agree with

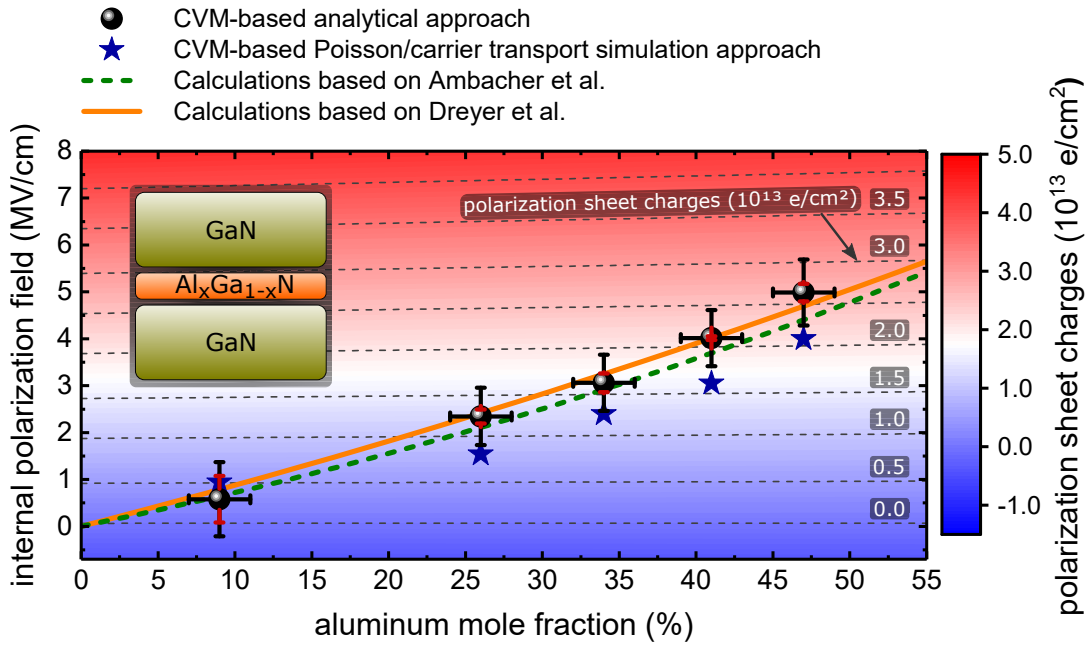


Figure 4.10: Internal polarization fields determined by the CVM-based analytical model and coupled Poisson-carrier transport simulation approach. In addition, theoretically predicted values by Ambacher et al. [46] and Dreyer et al. [45] are shown. The internal polarization fields were converted to polarization sheet charges using a simple parallel-plate capacitor model. Black error bars are determined by the error propagation and red errors by the standard deviation.

values predicted by theoretical calculation of ternary alloys. The dependence of the internal field strength on the Al mole fraction x can be approximated by a quadratic equation:

$$E_{Pol}(\text{Al}_x\text{Ga}_{1-x}\text{N}) = (6.2x + 9.0x^2) \frac{\text{MV}}{\text{cm}}. \quad (4.18)$$

It should be noted that most experimental studies (optical and electrical) show an underestimation of the internal field strength and a significant scatter compared to the theoretical prediction, which merits some discussion [45]. In optically based experiments, e.g. electron holography and photoluminescence, screening effects due to additionally generated free carriers could influence the polarization field evaluation [43, 171–173]. Additionally, most optically based experiments rely on Schrödinger-Poisson simulations to determine the magnitude of the internal polarization field, and therefore suffer from uncertainties in the input parameters [45, 174]. Measuring the density of the 2DEG in a HEMT structure by capacitance-voltage profiling [175] or Hall-measurements [176] to extract the internal polarization field can suffer from compensating surface states [176].

The polarization fields evaluated in this chapter were measured in the dark to eliminate optical excitation and measured at low reverse bias. Therefore, only few carriers are present in the junction and screening effects should not occur. Nevertheless, the CVM-based Poisson/carrier transport simulation approach also considers free carriers. Furthermore, the heterostructure is buried deep below the surface and surface states cannot influence the evaluation. By comparing the sample under investigation with a reference sample, the number of input parameters is minimized, and the internal polarization field is mainly determined by the difference of the measured capacitances.

Finally, the results indicate similar spontaneous polarization coefficients and piezoelectric polarization coefficients as the theoretical DFT calculations of the ternary compounds listed in Table 4.1, which allows the prediction of the internal polarization fields in AlGa_N-based UVC-LEDs.

4.7 Predicted polarization fields in AlGa_N-based UVC-LEDs

The results obtained in the last sections allow the prediction of the polarization fields generated in the AlGa_N-based MQW active region of UVC-LEDs. Figure 4.11(a) shows the spontaneous polarization field (green), the piezoelectric polarization field (gray) and the total polarization field (black) of a pseudomorphically grown 1.4-nm-thick Al_{*x*}Ga_{1-*x*}N quantum well embedded in relaxed AlN barriers as a function of the quantum well Al mole fraction *x*. The resulting quantum well emission wavelength between 211 nm and 342 nm was calculated by $\mathbf{k} \cdot \mathbf{p}$ -perturbation theory [177]. It should be noted, that the $\mathbf{k} \cdot \mathbf{p}$ -simulation includes the wavelength shift due to the QCSE. The material properties of GaN and AlN are taken from [178]. However, for the internal polarization fields, Fig. 4.11 uses the implementation recommended by Dreyer et al. [45]. High values of the piezoelectric polarization field (up to -13 MV/cm) and the spontaneous polarization field (up to 4.5 MV/cm) are observed. For a typical heterostructure, the AlN buffer is followed by AlGa_N and the negative piezoelectric polarization field is oriented anti-parallel to the positive spontaneous polarization field. Consequently, the total polarization field for an AlGa_N quantum well embedded in AlN barriers is always lower than the piezoelectric polarization. Figure 4.11(b) shows the polarization fields of a 1.4-nm-thick Al_{*x*}Ga_{1-*x*}N quantum well embedded in Al_{*y*}Ga_{1-*y*}N barriers. It is assumed that

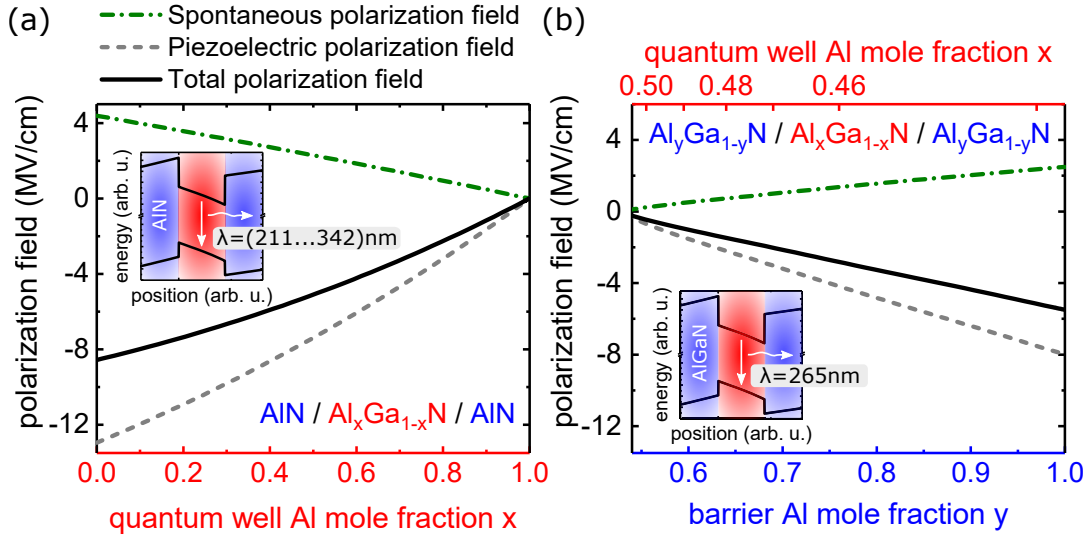


Figure 4.11: The spontaneous polarization field (green), the piezoelectric polarization field (gray) and the total polarization field (black) of a 1.4-nm-thick $\text{Al}_x\text{Ga}_{1-x}\text{N}$ quantum well embedded in (a) AlN barriers and (b) $\text{Al}_y\text{Ga}_{1-y}\text{N}$ barriers pseudomorphically grown on relaxed AlN buffer layers. In (b) the Al mole fraction x of the quantum well is adjusted in the sense that the emission wavelength is always at 265 nm. The emission wavelength in (a) and the quantum well Al mole fraction in (b) was determined by $\mathbf{k} \cdot \mathbf{p}$ -simulations. The calculated polarization fields use the implementation recommended by Dreyer et al. [45]. $\mathbf{k} \cdot \mathbf{p}$ -simulations performed by M. Guttmann, TUB.

the quantum well and the barriers are pseudomorphically strained to an AlN buffer layer. The Al mole fraction of the barriers varies between $y = 0.54$ and $y = 1.0$. In addition, the Al mole fraction of the quantum well is adjusted in the sense that the quantum well emission wavelength is always constant at 265 nm. The corresponding quantum well Al mole fraction for the 265 nm emission was calculated by $\mathbf{k} \cdot \mathbf{p}$ -simulations. High total polarization fields of up to -5.5 MV/cm are predicted. In the case of an $\text{Al}_{0.63}\text{Ga}_{0.37}\text{N}/\text{Al}_{0.48}\text{Ga}_{0.52}\text{N}$ quantum well, as used in the UVC-LED heterostructures investigated in this work, a total polarization field of -1.4 MV/cm is expected. The predicted values of the internal polarization field can be used to perform device simulations as discussed in the following section.

4.8 Influence of the QCSE on the emission characteristics

The strong internal polarization fields determined in the previous sections lead to the QCSE in AlGaIn -based MQW active regions. In the presence of the QCSE a reduced overlap of hole and electron wave functions as well as a red shift of the

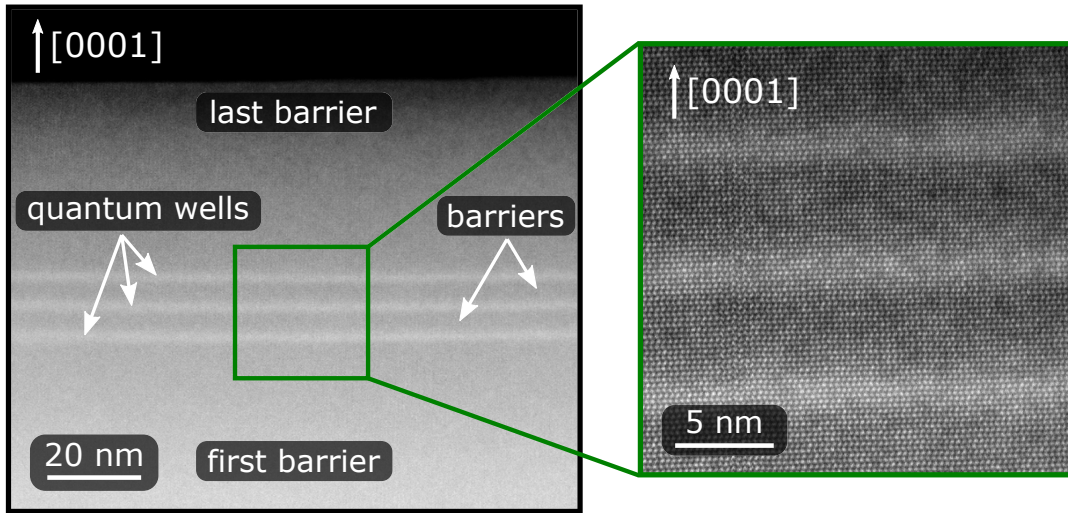


Figure 4.12: Cross-sectional STEM-HAADF images of an MQW heterostructure sample near the active region. Indicated are the 40-nm-thick first and last barrier as well as the 1.4-nm-thick quantum wells, which are separated by 5-nm-thick barriers. Measurements performed by Leonardo Cancellara, IKZ.

emission wavelength is expected (see section 1.3). However, it is assumed that the spatial separation of electrons and holes can be suppressed by using thin quantum wells [179]. The results obtained in the previous section enable to fix the internal polarization fields in simulation models, e.g. to the values proposed by Dreyer et al. [45]. Accordingly, $\mathbf{k} \cdot \mathbf{p}$ simulations [177] were performed for the emission wavelengths and the overlap integrals of the electron and hole wave function for different quantum well thicknesses. The material properties of GaN and AlN are taken from [178].

In order to compare the simulated emission wavelengths with experimental values, AlGa_N-based UVC-LEDs were grown on ELO AlN/sapphire templates. The UVC-LED heterostructure consist of a 600-nm AlN buffer layer, a 1200-nm-thick Al_{0.76}Ga_{0.24}N:Si *n*-side current spreading layer, an MQW active region, a 5-nm-thick Al_{0.85}Ga_{0.15}N interlayer, a 25-nm-thick Al_{0.80}Ga_{0.20}N:Mg/Al_{0.70}Ga_{0.30}N:Mg SPSL, a 183-nm-thick Al_{0.27}Ga_{0.73}N:Mg/Al_{0.17}Ga_{0.83}N:Mg SPSL and a 40-nm-thick GaN:Mg contact layer. In particular, the active region contains a 40-nm first Al_{0.63}Ga_{0.37}N:Si barrier, three Al_{0.48}Ga_{0.52}N quantum wells with thicknesses between 1 nm and 3.2 nm, separated by two 5-nm-thick Al_{0.63}Ga_{0.37}N:Si barriers and a 5-nm-thick last Al_{0.63}Ga_{0.37}N barrier. The simulations assume atomically flat heterointerfaces between the quantum wells and the barriers, which is especially crucial for thin quantum wells. Accordingly, cross-sectional high-angle annular dark-field scanning transmission electron microscopy (HAADF-STEM)

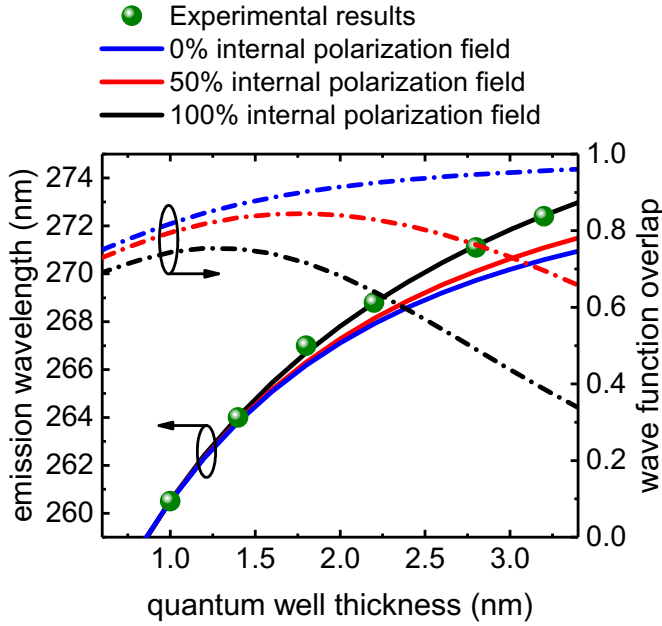


Figure 4.13: $\mathbf{k} \cdot \mathbf{p}$ simulations of the emission wavelength and the wave function overlap using the polarization fields recommended by Dreyer et al. [45]. The green dots represent the measured emission wavelengths at a current of 20 mA of three-fold MQW UVC-LEDs. Simulations performed by M. Guttman, TUB.

measurements were performed on an MQW sample using 1.4-nm-thick quantum wells. The MQW sample is basically identical to the UVC-LEDs described above, except for the omission of the p -layers and the increase in thickness to 40 nm for the last barrier. The HAADF-STEM images in Fig. 4.12 of the three-fold MQW active region reveal a quantum well thickness of (1.4 ± 0.3) nm, which is in agreement with the nominal quantum well thickness of 1.4 nm. In addition, relatively sharp heterointerfaces between the quantum wells and barriers are observed compared to the MQWs reported in the literature [118, 180, 181]. Consequently, a comparison between the $\mathbf{k} \cdot \mathbf{p}$ simulations and the experimental values is justified.

Figure 4.13 shows $\mathbf{k} \cdot \mathbf{p}$ simulations for the emission wavelengths using a constant energy offset as a fitting parameter, the wave function overlaps and the measured EL emission wavelengths of the UVC-LEDs. In addition, $\mathbf{k} \cdot \mathbf{p}$ simulations are shown without internal polarization fields and with 50% internal polarization fields. In general, an increasing emission wavelength with increasing quantum well thickness is observed. For thicknesses thinner than 1.5 nm, the red-shift in the emission wavelength is nearly independent of the internal polarization field and is mainly determined by the smaller quantum confinement [182]. However, for thicknesses above 1.5 nm, the emission wavelength depends on the internal polarization field due to the QCSE. At a quantum well thickness of 3 nm a red-shift of the emission wavelength from 270.0 nm (0% polarization field) to 271.9 nm (100% polarization field) is observed. The emission wavelength for

quantum well thicknesses above 1.5 nm is a result of the QCSE, which is caused by the internal polarization fields. Furthermore, an almost perfect agreement between the measured emission wavelengths of the UVC-LEDs and the $\mathbf{k} \cdot \mathbf{p}$ simulations is observed under the assumption of 100% internal polarization fields.

Figure 4.13 reveals a maximum of the overlap integrals of the electron and hole wave function at a quantum well thickness of 1.3 nm. With decreasing internal polarization field the maximum of the wave function overlap shifts to higher quantum well thicknesses and vanishes under the assumption of 0% internal polarization field. Consequently, the decreasing wave function overlap for quantum well thicknesses above 1.3 nm is caused by the QCSE. The QCSE spatially separates the electron and hole wave function, whereby the spatial separation increases with increasing quantum well thickness. For thickness below 1.3 nm the wave function overlap decreases with decreasing quantum well thickness due to the difference in the effective masses of electrons and holes [183]. The lower effective mass of the electrons leads to a higher penetration depth of the electron wave function into the barriers compared to the hole wave function (see Fig. 1.3), resulting in a decrease of the wave function overlap for quantum well thicknesses below 1.3 nm. The maximum of the overlap integrals of the electron and hole wave function at a quantum well thickness of 1.3 nm is in agreement with optimized quantum well thicknesses reported in literature [179, 184, 185]. Also in this work an optimal quantum well thickness of 1.3 nm was found (not shown here). Accordingly, the UVC-LEDs fabricated in this thesis contain quantum wells with thicknesses close to 1.3 nm. However, it should be noted that the different overlap integrals is not the only effect affecting the EQE by varying the thickness of the quantum wells. By reducing the thickness of the quantum well, it is expected that the number of charge carriers and the charge carrier confinement decreases, thus lowering the EQE (see Ref. [185] for further details). Nevertheless, for quantum wells with thicknesses of more than 3 nm the small overlap of the wave functions is the dominant effect in terms of the EQE [184, 185]. These results emphasize the importance of an accurate identification of the magnitude and direction of the internal polarization fields.

4.9 Summary and conclusion

In this chapter a new approach for the determination of polarization fields in III-nitride double heterostructures based on capacitance-voltage measurements was presented. The polarization fields can be evaluated either with a coupled Poisson-carrier transport simulation or a reference sample. Both methods are based on the change in the depletion region width of *pin*-diodes, which is caused by the polarization sheet charges at the interfaces. A comprehensive accuracy analysis showed a high influence of the capacitance precision. In order to be able to evaluate the internal polarization field as accurately as possible, an advanced capacitance-voltage-profiling and special sample structure design were developed and discussed.

Diodes with a nearly lattice-matched InAlN/GaN heterostructure enabled the determination of the spontaneous polarization field independently of the piezoelectric polarization field. The results showed a good agreement with theoretically predicted values indicating similar spontaneous polarization coefficients as the theoretical DFT calculations of the ternary compounds AlN, GaN and InN. Subsequently, the internal polarization fields of diodes with an AlGaN/GaN heterostructure, which exhibit both spontaneous and piezoelectric polarization fields, were investigated. The results showed that both CVM-based approaches are in excellent agreement with the values predicted by DFT calculations. Finally, the internal polarization fields were used to determine the polarizations fields in AlGaN-based UVC-LEDs and perform $\mathbf{k} \cdot \mathbf{p}$ simulations for the emission wavelengths and the overlap integrals of the electron and hole wave function. In particular, simulations were performed for different quantum well thicknesses, since it is expected that the spatial separation of electrons and holes can be suppressed by using thin quantum wells. A nearly perfect agreement between measured emission wavelengths of UVC-LEDs and the $\mathbf{k} \cdot \mathbf{p}$ simulations was observed. The simulations show a maximum of the wave function overlap at a quantum well thickness of 1.3 nm, which corresponds to the optimized quantum well thicknesses found in the literature [179, 184, 185].

The results presented in this chapter show that the developed and validated CVM-based approaches provide a quantitative measurement of the internal polarization field, which can be used as a more reliable input parameter in device simulations for further work.

5

Enhanced light extraction using a semi-transparent p-side

Typically, magnesium-doped GaN:Mg contact layers are used in the *p*-side of UVC-LEDs in order to realize ohmic *p*-metal contacts [3]. Unfortunately, these devices suffer from a reduced LEE due to the strong fundamental absorption in the GaN:Mg contact layer [186, 187]. By introducing a UVC-transparent AlGaIn:Mg contact layer in combination with a UV-reflective *p*-metal contact, an encapsulated flip-chip UVC-LED with an EQE of more than 20% was demonstrated by Takano et al. [22]. Nevertheless, this approach leads to an increased operating voltage resulting from the higher resistivity of the AlGaIn:Mg contact layer and the contact resistance of the interface between the AlGaIn:Mg layer and the *p*-metal contact [22]. It should be noted that in the last chapters only UVC-LEDs with a non-transparent *p*-side were discussed. In order to improve the LEE of UVC-LEDs, UV-reflective ohmic contacts on thin GaN:Mg layers might offer a solution [186]. Therefore, a semi-transparent *p*-side is designed using UV-transparent *p*-AlGaIn layers as well as UV-absorbing GaN:Mg contact layers. The thickness of the GaN:Mg contact layer is varied and the structural and electro-optical properties are systematically investigated.

UVC-LED heterostructures with a semi-transparent *p*-side were grown by MOVPE on ELO AlN/sapphire templates (Fig. 5.1). Up to the 25-nm-thick Al_{0.75}Ga_{0.25}N:Mg EBL the device heterostructure is identical to the heterostructure presented in chapter 2.3, i.e. a 900-nm-thick Al_{0.76}Ga_{0.24}N:Si current spreading layer, a 100-nm-thick AlGaIn:Si transition layer, a 200-nm-thick Al_{0.65}Ga_{0.35}N:Si contact layer, a triple Al_{0.62}Ga_{0.38}N/Al_{0.48}Ga_{0.52}N MQW, a 10-nm-thick Al_{0.85}Ga_{0.15}N interlayer and a 25-nm-thick Al_{0.75}Ga_{0.25}N EBL were

UVC-LED heterostructure

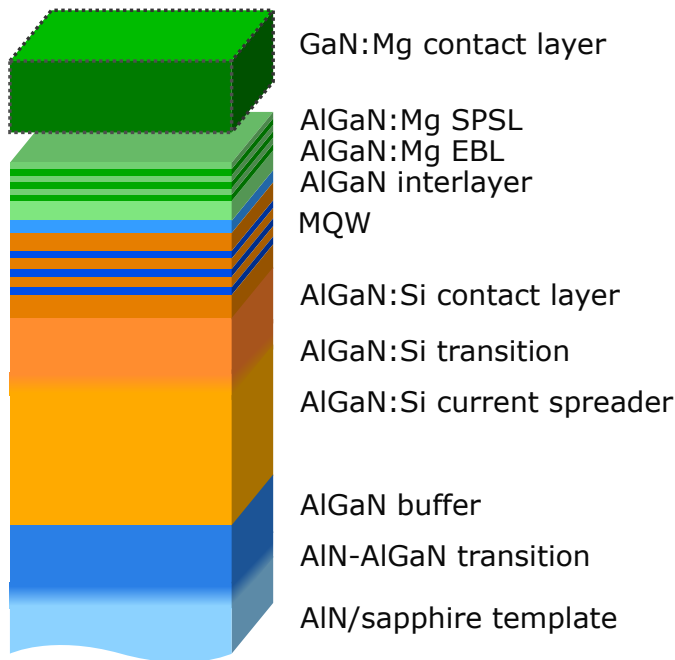


Figure 5.1: Schematic of the UVC-LED heterostructures grown on ELO AlN/sapphire templates with nominal GaN:Mg contact layer thicknesses varying between 0 nm and 250 nm.

used. Subsequently, a 90-nm-thick $\text{Al}_{0.65}\text{Ga}_{0.35}\text{N:Mg}/\text{Al}_{0.71}\text{Ga}_{0.29}\text{N:Mg}$ SPSL was grown with a period of 6 nm using equal thicknesses of 3 nm for both layers. Finally, the UVC-LED heterostructure was capped with a GaN:Mg contact layer with layer thicknesses between 0 nm and 250 nm. However, the structural investigations in the following section 5.1 show that the growth of thin GaN:Mg contact layers is complex and the determined layer thicknesses are only nominal. The p -doping of the contact layer was obtained by a constant $\text{Cp}_2\text{Mg}/\text{TMGa}$ precursor partial pressure ratio of 2.0%. Secondary ion mass spectroscopy measurements (performed by Evans Analytical Group [151]) showed a Mg-concentration in the GaN:Mg contact layer of $1.0 \times 10^{20} \text{ cm}^{-3}$. It should be noted that the UVC-LED heterostructure is transparent for UVC emission except for the GaN:Mg contact layer, which will be discussed in the next section.

5.1 Inhomogeneous growth and transparency of the GaN:Mg layer

In this section, the structural and optical properties of the GaN:Mg contact layers grown on the 90-nm-thick $\text{Al}_{0.65}\text{Ga}_{0.35}\text{N:Mg}/\text{Al}_{0.71}\text{Ga}_{0.29}\text{N:Mg}$ SPSL are investigated. Figure 5.2 shows AFM topograms of the surface of UVC-LED heterostructures covered with a GaN:Mg contact layer with the aforementioned het-

erostructure and varied nominal thickness of the GaN:Mg contact layer between 0 nm and 250 nm. The surface morphology depends strongly on the GaN:Mg contact layer thickness. Figure 5.2(a) shows the UVC-LED heterostructure surface without a GaN:Mg contact layer. The typical spiral growth dominated surface morphology is observed, which is mainly determined by the n -side current spreading layer (see chapter 3 for further details about the n -side morphology). The samples with a nominal GaN:Mg contact layer thickness of 5 nm and 10 nm (Fig. 5.2(b)(c)), corresponding to a growth time of 23 s and 46 s, show similar surface morphologies. In contrast, at a nominal thickness of 20 nm small GaN clusters with a height between 3 nm and 10 nm and a radius between 40 nm and 60 nm are observed along the hillock steps. The density of these clusters was determined to $1.2 \times 10^9 \text{ cm}^{-2}$ by the $5 \times 5 \mu\text{m}^2$ AFM topogram shown in the inset of Fig. 5.2(d). For a GaN:Mg contact layer thickness of 40 nm, the clusters with an average height of around 20 nm appear to coalesce and grow laterally between the hillocks, while the growth on the hillock cores seems to be delayed. As the GaN:Mg layer continues to grow, the islands begin to coalesce. The inset in Fig. 5.2(g) shows an AFM topogram between the GaN:Mg islands. By comparing the inset in Fig. 5.2(b) and (g) a significant change in the hillock morphology is observed, indicating GaN:Mg growth at the hillock cores. Nevertheless, even with a nominal 160-nm-thick GaN:Mg layer, holes with a depth of 130 nm are observed on the UVC-LED surface. At a nominal GaN:Mg contact layer thickness of 250 nm, the layer is fully coalesced. It should be noted that the measured island height of the GaN:Mg contact layer (Fig. 5.2(e)-(i)) is always 20 nm to 30 nm thinner than the nominal GaN:Mg contact layer thickness. These results might indicate a delayed growth of the GaN:Mg contact layer by about 90 s corresponding to a thickness of 20 nm. However, the cause of the delayed growth needs further investigation.

In order to analyze the optical properties of the UVC-LED heterostructures transmission measurements were performed. Figure 5.3(a) shows the transmission spectra of the UVC-LED heterostructures with varying GaN:Mg contact layer thickness. The transmission measurements were performed with a two-beam absorption UV-VIS-Shimadzu UV-2600 spectrophotometer under normal incidence in an integrating sphere. In addition, a representative EL emission spectrum exhibiting single peak emission at $\lambda = 265 \text{ nm}$ of a UVC-LED without GaN:Mg contact layer is shown in Fig. 5.3(a). The transmission spectra are normalized to the UVC-LED heterostructure without a GaN:Mg contact layer

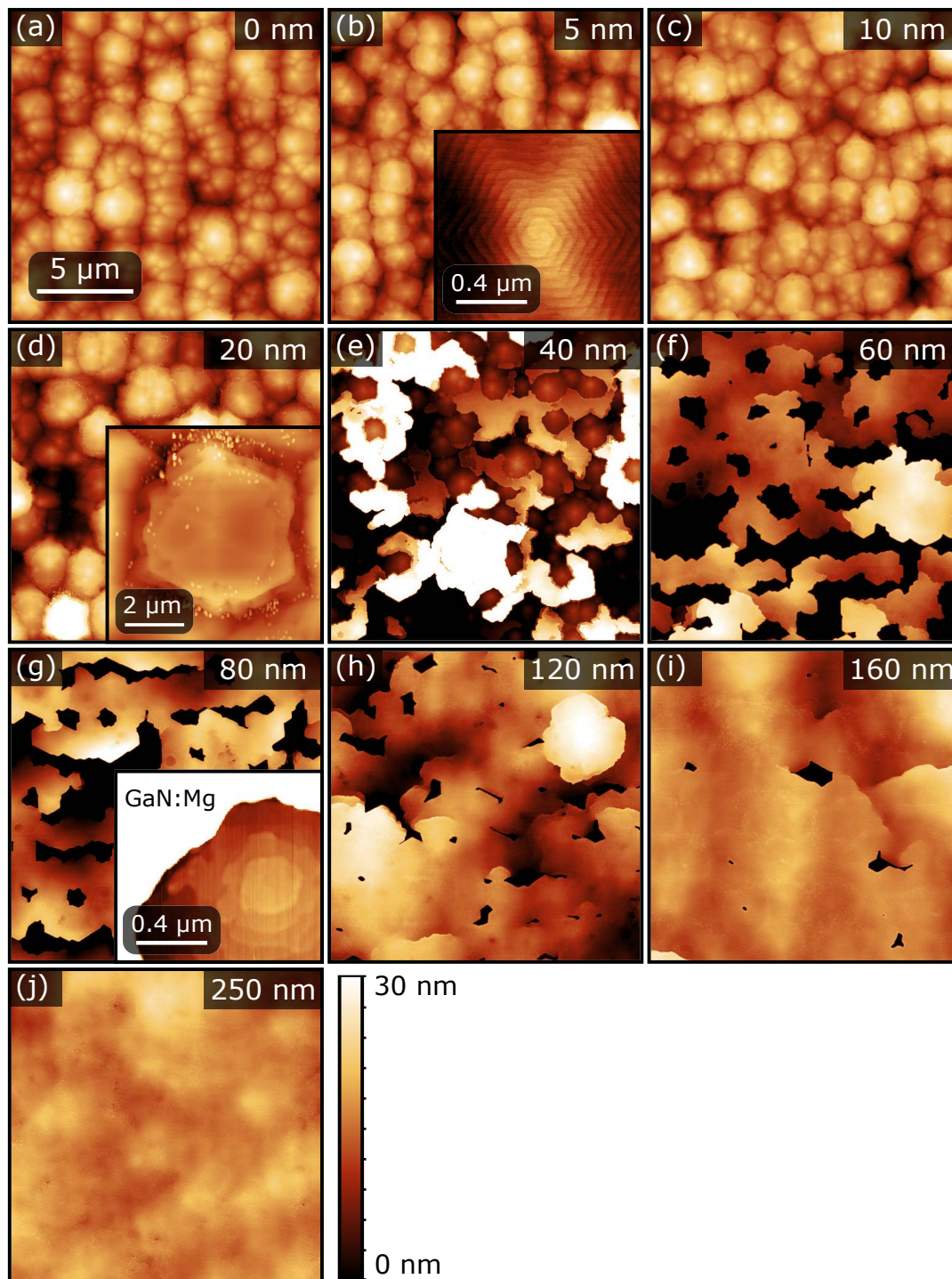


Figure 5.2: AFM topograms of UVC-LED heterostructures with nominal GaN:Mg contact layer thicknesses varying between 0 nm and 250 nm. In (b) and (c) no evidence of a GaN:Mg contact layer is observed. The height of the GaN:Mg islands in (e)-(i) is always 20 nm to 30 nm smaller than the nominal GaN:Mg contact layer thickness. The inset in (g) shows a morphological change (compared to (b)) of the hillocks, indicating GaN growth on the hillock cores. Measurements performed together with E. Ziffer, TUB.

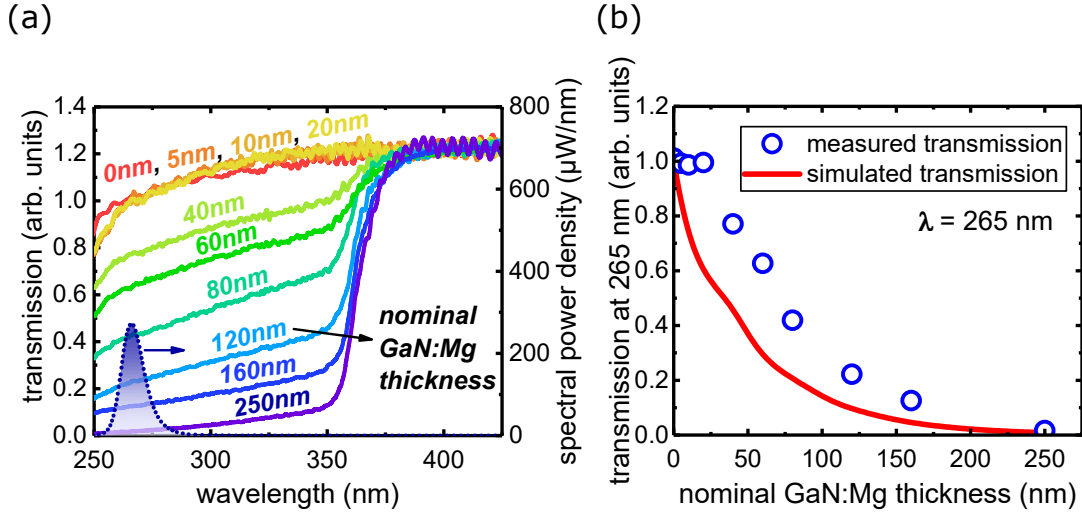


Figure 5.3: (a) Transmission spectra of the UVC-LED heterostructures with different GaN:Mg contact layer thicknesses as well as the spectral power density of a representative UVC-LED without a GaN:Mg contact layer at an injection current of 20 mA and room temperature. (b) Measured and simulated transmission at a wavelength of 265 nm as a function of the nominal GaN:Mg layer thickness. Measurements performed together with E. Ziffer, TUB. Transfer matrix simulations performed by M. Guttman, TUB.

at 265 nm, assuming a negligible absorption of the heterostructure at this wavelength [188,189]. All transmission spectra show a slightly decreasing transmission with decreasing wavelength, which is most likely related to the higher refractive index [190] and thus increased losses due to light scattering at the ELO voids. In line with the AFM topograms in Fig. 5.2(a)-(c), no significant difference in the transmission spectra is observed between the UVC-LEDs with and without a nominal 5-nm and 10-nm-thick GaN:Mg contact layer. Furthermore, the GaN:Mg clusters observed in Fig. 5.2(d), at a nominal GaN:Mg contact layer thickness of 20 nm, do not lead to any significant absorption. However, for GaN:Mg contact layers thicker than nominal 40 nm, the corresponding absorption edge of GaN at 364 nm [191] becomes visible and results in a continuously decreasing transmission with increasing GaN:Mg contact layer thickness. It is noteworthy that in the UVC-LED, the portion of UV-light reflected at the p -metal contacts must pass through the GaN:Mg contact layer at least twice before it can be coupled out through the sapphire. Figure 5.3(b) shows the measured and normalized transmissions at $\lambda = 265$ nm for the UVC-LEDs as a function of the GaN:Mg contact layer thickness. Moreover, the transmissions at 265 nm were simulated with the transfer matrix method (red curve in 5.3(b)) [192] using an absorption coefficient for GaN of $\alpha = 185000 \text{ cm}^{-1}$ [190]. The transmissions calculated by the transfer matrix method show an almost exponential decrease

with increasing GaN:Mg contact layer thickness, which is consistent with the Lambert-Beer law [193]. However, due to interference effects, a slight deviation at approximately 30 nm is observed. The simulated transmission values are lower compared to the measured values for nominal GaN:Mg contact layer thicknesses between 5 nm and 160 nm. The discrepancy between the transmission values decreases with increasing GaN:Mg layer thickness. Similarly, the AFM results showed an island height of the GaN:Mg contact layer 20 nm to 30 nm thinner compared to the nominal GaN:Mg contact layer thickness (Fig. 5.2(e)-(i)). Even after assuming a 30-nm-thicker GaN:Mg contact layer the simulated transmission values are still lower (not shown here). However, the residual discrepancy can be explained by the inhomogeneous coverage of the GaN:Mg contact layer for thicknesses between 40 nm and 160 nm.

5.2 Improved efficiency of the semi-transparent UVC-LEDs

To investigate the influence of the inhomogeneous distribution of the GaN:Mg layer and the varying transmission on the electrical-optical performance, the emission power of the UVC-LEDs was measured on-wafer with a calibrated large-area silicon photodiode at room temperature. Figure 5.4 shows the emission power at a current of 20 mA of the UVC-LEDs as a function of the nominal GaN:Mg thickness measured with an indium quick test setup. For this purpose, In dots with a radius of around 500 μm were distributed on the surface of the UVC-LEDs as *p*-metal contacts. It should be noted that In has a high reflectivity

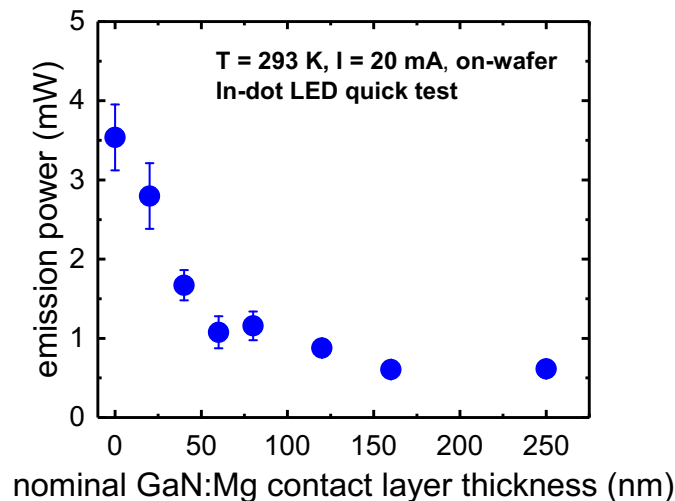


Figure 5.4: Average emission power at an injection current of 20 mA as a function of the nominal GaN:Mg contact layer thickness. The vertical error bars corresponds to the standard deviation. Measurements performed together with E. Ziffer, TUB.

of 0.87 ± 0.02 at the UVC-LED emission peak wavelength of 265 nm [194]. The reflectivity of the *p*-metal contact on sapphire was determined using a Shimadzu UV-2600 UV-VIS spectrophotometer as described in Ref. [194]. The emission power values in Fig. 5.4 were averaged over four different UVC-LEDs across the wafer and the error bars correspond to the standard deviation. UVC-LEDs without detectable emission power, e.g., due to short circuits, are not included in the evaluation in Fig. 5.4. With decreasing GaN:Mg thickness an increasing emission power is observed. This behaviour can be explained by the lower absorption in the *p*-side heterostructure in combination with the highly UV-reflective In *p*-metal contact, resulting in an enhanced LEE. In case of thin GaN:Mg contact layers, the UVC-LED emission power is strongly dependent on the GaN:Mg layer thickness due to exponentially increasing absorption. However, for thicknesses larger than 160 nm, no significant change in the emission power is observed. This is most probably because the UV-light emitted towards the *p*-side is nearly completely absorbed in the GaN:Mg contact layer. The highest emission power at 20 mA of (3.5 ± 0.4) mW was recorded for the UVC-LED without a GaN:Mg contact layer. Therefore, the emission power of the UVC-LED without a GaN:Mg contact layer is almost six times higher than that of the UVC-LED with a nominal 250-nm GaN:Mg layer, which exhibits an emission power of (0.6 ± 0.1) mW. However, for thin GaN:Mg contact layers, a higher emission power fluctuation and an increased probability of short circuits during operation are observed.

To further investigate the efficiency increase with decreasing GaN:Mg contact layer thickness, the LEE was simulated with a Monte-Carlo ray-tracing model [91,186] (see section 2.2.3 for more details about simulation). In order to consider the complex morphology of the GaN:Mg contact layer and the influence of the deviation from the nominal GaN:Mg thickness on the LEE, the transmission measurements from Fig. 5.3 were used. According to the Lambert-Beer law, effective thicknesses were determined from the measured transmission values at 265 nm (blue dots in Fig. 5.3(b)) using an absorption coefficient for GaN of $\alpha = 185000 \text{ cm}^{-1}$ [190]. The calculated effective thicknesses were used in the ray-tracing simulation for the GaN:Mg contact layer thickness. Figure 5.5 shows the simulated LEE as a function of the nominal GaN:Mg contact layer thickness and the EQE determined from the on-wafer emission powers at 20 mA. The scaling factor between the axes in Fig. 5.3 corresponds to the IQE ($\text{EQE} = \text{IQE} \times \text{LEE}$). The IQE was set to 26% (see Fig. 2.18 regarding ELO AlN/sapphire) based on

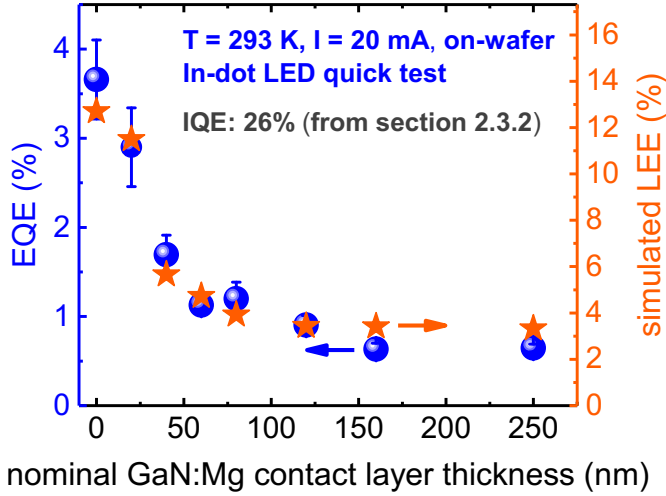


Figure 5.5: Average EQE at a current of 20 mA as a function of the nominal GaN:Mg thickness. The vertical error bars corresponds to the standard deviation. Furthermore, the simulated LEE is shown using the effective GaN:Mg thickness determined from the transmission measurements. The scaling factor of 0.26 (which represents the IQE) between the axes corresponds to the IQE determined in section 2.3.2. Simulations performed by M. Guttman, TUB.

the evaluations in the section 2.3.2. Similar to the emission power at 20 mA, the EQE increases from $(0.7 \pm 0.1)\%$ to $(3.7 \pm 0.4)\%$ with decreasing GaN:Mg contact layer thickness. Almost the same ratio of the efficiency improvement is observed for the simulated LEE with decreasing GaN:Mg layer thickness assuming an IQE of 26%. The LEE increases nearly exponentially with decreasing GaN:Mg contact layer thickness from 3.3% to 12.7%. The overlap of the EQE and the simulated LEE in Fig. 5.5 assuming a constant IQE of 26% shows that the increase in the EQE can be explained by an increase in the LEE. Accordingly, the results show no dependence of the REE and INJ on the GaN:Mg contact layer thickness.

In order to investigate the operating voltage, the UVC-LED heterostructures with a nominal 10-nm, 20-nm, 40-nm, 80-nm and 160-nm-thick GaN:Mg contact layer were processed with standard micro-fabrication techniques using V-based *n*-metal contacts and In *p*-metal contacts¹. Figure 5.6 shows representative current-voltage characteristics of the processed UVC-LEDs with different GaN:Mg contact layer thicknesses. At a current of 0.1 mA (inset in Fig. 5.6), i.e. a current density of 1 A cm^{-2} (sometimes referred as turn-on voltage [194]), a decreasing device operating voltage between 13.2 V and 8.8 V is observed with increasing GaN:Mg contact layer thickness. However, the UVC-LEDs with a nominal 80-nm and 160-nm-thick GaN:Mg contact layer exhibit similar voltages at 0.1 mA. Transfer length method (TLM) measurements revealed an ohmic behavior of the *n*-metal contacts and a rectifying behavior for the *p*-metal contacts. Therefore, the deviation from the built-in potential $\sim 4.7 \text{ V}$ [194] and

¹The micro-fabrication process was performed by L. Sulmoni, TUB.

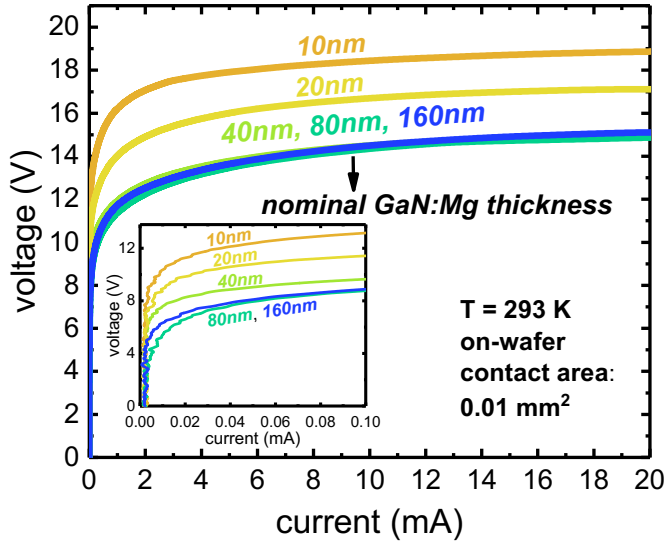


Figure 5.6: Representative current-voltage characteristics of UVC-LEDs with GaN:Mg contact layers with thicknesses between 10 nm and 160 nm. The inset shows the current-voltage characteristics at lower currents. The characteristics were measured on-wafer using In *p*-metal contacts and V-based *n*-metal contacts. Measurements performed together with E. Ziffer, TUB.

the device operating voltage at 0.1 mA is most likely caused by the Schottky barrier at the interface between the semiconductor and the *p*-metal contact. The results suggest the following explanation for the decreasing voltage with increasing nominal GaN:Mg contact layer thickness: The UVC-LED with a nominal 10-nm GaN:Mg contact layer most likely exhibits the highest total Schottky barrier, since the AFM (Fig. 5.2) and transmission measurements (Fig. 5.3) indicate the absence of GaN:Mg on the surface. As the nominal thickness of the GaN:Mg contact layer increases, the total Schottky barrier decreases due to the areas covered with GaN:Mg. However, at locations without GaN:Mg, the direct contact with the $\text{Al}_{0.65}\text{Ga}_{0.35}\text{N:Mg}/\text{Al}_{0.71}\text{Ga}_{0.29}\text{N:Mg}$ SPSL will lead to a higher Schottky barrier at these positions [186]. This configuration of regions with and without GaN:Mg, corresponding to regions with a higher and lower Schottky barrier, can be described as parallel connected components. Accordingly, the majority of the charge carriers will flow through the areas with lower resistance, i.e. most likely through the areas covered with GaN:Mg. With increasing nominal thickness (resulting in higher coalescence, Fig. 5.2) the effective contact area with low resistance becomes larger and the voltage decreases due to the lower current density. After exceeding the nominal 80-nm GaN:Mg contact layer thickness, the change in the voltage due to further coalescence becomes negligible and no further reduction in voltage is observed.

In order to investigate the applicability of UVC-LEDs with a semi-transparent *p*-side for high-power devices, 1-mm² flip-chip LEDs with 0.52-mm² Pt *p*-metal contacts mounted on AlN-based planar packages were fabricated². Based on the

²The chip process was performed by J. Rass and N. Lobo-Ploch, FBH.

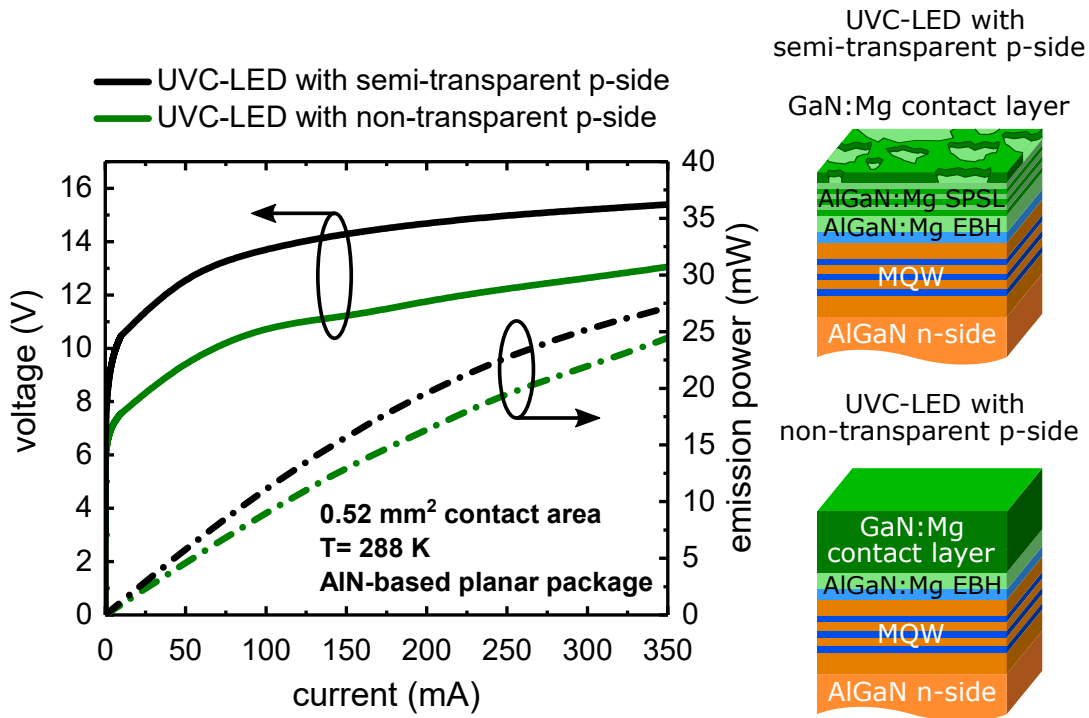


Figure 5.7: Integrating sphere measurements of the EL emission power of UVC-LED with a semi-transparent *p*-side and a non-transparent *p*-side. Furthermore, the heterostructure design of the semi-transparent *p*-side (transparent SPSL and nominal 60-nm GaN:Mg) and the non-transparent *p*-side (nominal 230-nm GaN:Mg) is shown. Measurements performed by N. Lobo-Ploch, FBH.

aforementioned results, the UVC-LED heterostructure with a nominal 60-nm GaN:Mg contact layer was chosen due to the combination of high emission power and low operating voltage. In addition, a similar UVC-LED heterostructure with a non-transparent *p*-side using exclusively 230-nm GaN:Mg, i.e. no SPSL, on the *p*-side after the EBL (Fig. 5.7) was fabricated into a 1-mm² flip-chip LED. The LIV characteristics were measured in a calibrated integrating sphere at a controlled temperature of 288 K. Figure 5.7 shows the LIV characteristics of the UVC-LEDs with a semi-transparent *p*-side consisting of an Al_{0.65}Ga_{0.35}N:Mg/Al_{0.71}Ga_{0.29}N:Mg SPSL and a 60-nm GaN:Mg contact layer as well as a non-transparent *p*-side consisting of 230-nm GaN:Mg. The IV characteristics reveal a higher operating voltage of the UVC-LED with a semi-transparent *p*-side compared to the UVC-LED with a non-transparent *p*-side. At 20 mA a voltage difference of 3 V (11.0 V → 8.0 V) is observed. It should be noted that besides the *p*-side, the UVC-LED heterostructures are nominally identical. Accordingly, the additional voltage drop is most likely related to the difference in the *p*-side heterostructure. However, the difference in the voltage drop at the interface between the semiconductor and the *p*-metal contact is

assumed to be less than 0.5 V based on the results shown in Fig. 5.6. Furthermore, if the SPSL behaves like a series resistor with constant resistance, the voltage difference would depend on the injection current according to Ohm's law. However, the voltage difference between the UVC-LED with a semi-transparent p -side and the UVC-LED with a non-transparent p -side is almost constant with increasing current. This indicates a dependence of the SPSL resistivity on the voltage. Such voltage-dependence of the resistivity might be explained by the Poole-Frenkel effect [195–197]. The Poole-Frenkel effect describes the reduced effective ionization energy in semiconductors, due to the lowering of the Coulomb potential barrier by an applied electric field. This increases the free carrier concentration and thus the conductivity of the doped semiconductor. The decreasing resistivity with increasing voltage caused by the Poole-Frenkel effect could be an explanation for the almost constant voltage drop difference of about 3 V. As a result of the increase in the LEE, the UVC-LED with a semi-transparent p -side exhibits a higher emission power of 27 mW at a current of 350 mA compared to the UVC-LED with a non-transparent p -side, which has an emission power of 24 mW at 350 mA. Here it is worth noting that the relative improvement in the emission power is smaller compared to the results obtained in Fig. 5.4 due to the lower reflectivity of Pt (0.32 ± 0.02 at 265 nm) compared to In (0.87 ± 0.02 at 265 nm). As described in Ref. [194] the reflectivity of the p -metal contacts was determined by reflection measurements on sapphire with a Shimadzu UV-2600 UV-VIS spectrophotometer³. However, due to its low melting point of 157 °C [198] In is not suitable as a p -metal contact for flip-chip UVC-LEDs. The WPEs of the semi-transparent UVC-LED and the non-transparent UVC-LED are similar at 0.91% and 0.96%, respectively. The increase in the EQE due to the improvement of the LEE is compensated by the additional voltage drop at the $\text{Al}_{0.65}\text{Ga}_{0.35}\text{N:Mg}/\text{Al}_{0.71}\text{Ga}_{0.29}\text{N:Mg}$ SPSL.

In order to improve the WPE, a semi-transparent UVC-LED in combination with a highly reflective p -metal contact is required. Al might be the most suitable material because of its very high reflectivity in the UVC spectral range ($R \geq 0.9$) [199]. Nevertheless, Al does not form an ohmic contact to GaN:Mg due to its small working function [199]. An alternative approach is the deposition of a thin, semi-transparent metal layer between the semiconductor and the Al metal layer, which reduces the contact resistance. For example, Jo et al. reported on enhanced light extraction in 260-nm UVC-LED using a Ni/Al p -

³Reflection measurements performed by M. Guttman, TUB.

metal contact [200]. Other approaches are based on Rh [22] or Mo *p*-metal contacts [201]. However, all reported *p*-metal contacts with high reflectivity showed an increased operating voltage compared to a standard *p*-metal contact with low reflectivity [199]. Accordingly, the use of the semi-transparent *p*-side presented in this chapter requires the formation of ohmic *p*-metal contacts with high reflectivity in the UVC spectral range, which needs further investigation and process development.

5.3 Summary and conclusion

In order to enhance the EQE by improving the light extraction of UVC-LEDs, the applicability of semi-transparent *p*-sides was investigated. A transparent $\text{Al}_{0.65}\text{Ga}_{0.35}\text{N}:\text{Mg}/\text{Al}_{0.71}\text{Ga}_{0.29}\text{N}:\text{Mg}$ SPSL was implemented in the *p*-side of the UVC-LED heterostructure and the thickness of the (UV-absorbing) GaN:Mg contact layer was varied. The structural investigation showed that the GaN:Mg growth is complex and the surface morphology of the UVC-LED heterostructure is strongly dependent on the GaN:Mg contact layer thickness. The inhomogeneous 3D growth occurred preferentially in the hillock valleys, which provide many step edges. With increasing layer thickness the GaN:Mg layer coalesced, resulting in a nearly closed layer for nominal thicknesses higher than 160 nm. Furthermore, by using highly reflective In *p*-metal contacts a drastically increased emission power with decreasing GaN:Mg contact layer thickness was observed. Ray-tracing simulations of the LEE of UVC-LEDs showed that less absorption in the GaN:Mg contact layer leads to increased emission power for thinner GaN:Mg layers. Moreover, the results indicated no dependence of the IQE on the GaN:Mg contact layer thickness. On the other hand, the device operating voltage increased with decreasing GaN:Mg layer thickness. However, the operating voltage reached its minimum even before the surface was completely coalesced, which could offer the possibility of improved light extraction and a low operating voltage. Accordingly, a UVC-LED heterostructure with a semi-transparent *p*-side was processed into a flip-chip LED using an uncoalesced nominal 60-nm-thick GaN:Mg contact layer. Additionally, a similar UVC-LED heterostructure with a non-transparent *p*-side using exclusively 230-nm GaN:Mg and no SPSL on the *p*-side was fabricated into a flip-chip LED. In order to provide a convenient *p*-electrode, Pt was chosen as the *p*-metal contact. However, due to the low reflectivity of Pt of (0.32 ± 0.02) at 265 nm) the improvement of the emission power could not compensate the higher operating voltage due to the strong voltage drop at the

$\text{Al}_{0.65}\text{Ga}_{0.35}\text{N:Mg}/\text{Al}_{0.71}\text{Ga}_{0.29}\text{N:Mg}$ SPSL. Therefore the resulting WPEs of the semi-transparent p -side UVC-LED and the non-transparent p -side UVC-LED were similar. In order to further increase the WPE of the semi-transparent p -side, ohmic p -metal contacts with high reflectivity in the UVC spectral range are required.

6

Summary and perspectives

In this thesis, the heterostructure design and the epitaxial growth of AlGaIn-based UVC-LEDs with emission wavelengths near 265 nm were investigated. Furthermore, a comprehensive and fundamental study of the internal polarization fields occurring in UVC-LEDs was presented. The aim was to realize UVC-LEDs with high emission power with the potential to be used in applications such as sterilization and water disinfection.

The first step in designing the LED-heterostructure was the choice of a suitable template. Based on the beneficial influence of high temperature annealing on the crystal quality of AlN/sapphire templates, the applicability of low-cost sputtered-based HTA AlN/sapphire templates was investigated for the growth of UVC-LEDs and compared to ELO AlN/sapphire templates. HRXRD and panchromatic CL topograms showed a lower TDD of $1 \times 10^9 \text{ cm}^{-2}$ of the sputtered HTA AlN template compared to the ELO AlN template. Consistent with these results, temperature and excitation power dependent PL investigations indicated a higher RRE of the AlGaIn-based MQW on the sputtered HTA AlN templates. Due to the increase in the LEE caused by the striped patterned voids of the ELO process, nearly identical LI characteristics were measured, exhibiting an on-wafer emission power of 0.7 mW at 20 mA. Nevertheless, these results could help to accelerate the implementation of UVC-LEDs in different applications by bringing down the chip costs through the implementation of low-production-cost sputtering and HTA. To further improve the emission power, the HTA approach was combined with the ELO process. HRXRD, panchromatic CL topograms and cross-sectional TEM studies consistently showed a dislocation density of around $0.9 \times 10^9 \text{ cm}^{-2}$, which improved the RRE of UVC-LEDs on the HTA ELO AlN template relative to the HTA planar AlN and ELO AlN template. Finally,

the emission power as well as the device lifetime of the UVC-LEDs on HTA ELO AlN were also improved, making them suited for high power UVC-LEDs. UVC-LED chips on HTA ELO AlN templates with an emission power of 47 mW at 350 mA, an maximum EQE of 3.6% and an extrapolated L70 lifetime of 10,000 h were realized.

The growth of the AlGa_xN layers on AlN/sapphire templates can also lead to the generation of defects caused by the compressive strain. Cross-sectional TEM investigations indicated a formation of dislocation loops in the AlGa_xN layers. The density of these dislocation loops increases with increasing compressive strain as well as the layer thickness and their presence strongly reduces the emission power of the UVC-LEDs. The generation of the strain-induced dislocation loops was successfully suppressed by using a heterostructure approach for the *n*-side containing a 900-nm-thick Al_{0.76}Ga_{0.24}N:Si *n*-side current spreading layer, a 100-nm-thick Al_{0.76→0.65}Ga_{0.24→0.35}N:Si transition layer and a 200-nm-thick Al_{0.65}Ga_{0.35}N:Si *n*-side contact layer. The introduction of a second AlGa_xN:Si contact layer opened the way to reduce the operating voltage by 2.2 V at a current of 20 mA of the UVC-LEDs, while maintaining the emission power. As a result an on-wafer WPE of 1.0% at an operating voltage of 5.2 V and 20 mA was achieved.

In addition, the internal polarization fields are a critical factor for the performance of AlGa_xN-based UVC-LEDs. Unfortunately, the magnitude of the polarization fields, which is crucial for accurate device simulations, is still controversially discussed. A new approach was derived, presented and examined using capacitance-voltage measurements to determine the polarization fields. Both approaches are based on the change in the width of the depletion region, caused by the polarization sheet charges at the interfaces. The polarization fields were extracted either by using a reference sample or a coupled Poisson-carrier transport simulation. A comprehensive study on the accuracy of the approaches showed that both the capacitance and the thickness of the layer of interest are crucial for the precise determination of the polarization fields. In order to improve the accuracy, an advanced model for measuring the capacitance-voltage profiles was developed and the thickness of the layer of interest was determined by cross-sectional TEM. The two approaches showed consistent results of the magnitude and direction of the internal polarization fields, which were found to be in agreement with the values predicted by theory. Diodes with a lattice-matched InAlN/GaN double heterostructure enabled the determination of the

spontaneous polarization field to (5.4 ± 0.9) MV/cm without superposition with a piezoelectric polarization field. For AlGaN/GaN double heterostructures an increasing magnitude of the total polarization field between (0.6 ± 0.7) MV/cm ($\text{Al}_{0.09}\text{Ga}_{0.91}\text{N}$) and (5.0 ± 0.8) MV/cm ($\text{Al}_{0.47}\text{Ga}_{0.53}\text{N}$) were determined. The extracted polarization fields agree with the values predicted by DFT calculations and the redshift of the emission wavelength caused by the QCSE.

In order to increase the EQE and the output power, heterostructure designs that increase the LEE were investigated. Typically, thick GaN:Mg contact layers are used in the p -side of UVC-LEDs, limiting the LEE due to fundamental absorption. In order to increase the emission power and maintaining the electrical performance, the applicability of semi-transparent p -sides was studied. A transparent $\text{Al}_{0.65}\text{Ga}_{0.35}\text{N:Mg}/\text{Al}_{0.71}\text{Ga}_{0.29}\text{N:Mg}$ SPSL was incorporated in the p -side of the UVC-LEDs and the thickness of the (absorbing) GaN:Mg layer was varied between 250 nm and 0 nm. By using highly UV-reflective In p -metal contacts, a six-fold increase in the emission power was observed for the UVC-LED without GaN:Mg compared to the UVC-LED with 250 nm GaN:Mg due to a higher LEE. On the other hand, the operating voltage increased by 4 V at 20 mA when the GaN:Mg layer thickness was reduced. However, the operating voltage reached its minimum in regards to the GaN:Mg layer thickness before the UVC light is fully absorbed in the GaN:Mg layer, offering the possibility of improved light extraction and low operating voltage. UVC-LED chips with a semi-transparent p -side and Pt p -metal contacts were presented, showing an emission power of 27 mW at 350 mA. To further improve the emission power, it is necessary to develop highly UV-reflective p -metal contacts that are suitable for an LED chip process.

The work of this thesis has contributed to the development of highly efficient UVC-LEDs as a part of the German research consortium *Advanced UV for Life* and the *Joint Lab GaN-Optoelektronik*. For UVC-LEDs with an emission wavelength of 265 nm, among the highest EQEs (3.6%) and WPEs (2.7%) published so far were attained. In addition, the developed UVC-LEDs exhibited excellent lifetimes ($L_{70} \geq 10,000$ h) and yield of functioning devices ($\geq 95\%$). The achieved performance characteristics paved the way for the use of these devices in various applications. Within the *Advanced UV for Life consortium* a disinfection reactor module is planned using 90×265 -nm UVC-LEDs.

7

Bibliography

- [1] M. Kneissl, J. Rass, *III-Nitride ultraviolet emitters* (Springer, 2016).
- [2] V. Adivarahan, J. Zhang, A. Chitnis, W. Shuai, J. Sun, R. Pachipulusu, M. Shatalov, M. A. Khan, *Sub-Milliwatt Power III-N Light Emitting Diodes at 285 nm*, Japanese Journal of Applied Physics **41**, L435 (2002).
- [3] M. Kneissl, T.-Y. Seong, J. Han, H. Amano, *The emergence and prospects of deep-ultraviolet light-emitting diode technologies*, Nature Photonics **13**, 233 (2019).
- [4] H. Hirayama, *Recent Progress and Future Prospects of AlGaIn-based Deep-UV LEDs*, in *Light, Energy and the Environment*, pages DW2C.1 (Optical Society of America, 2014).
- [5] Y. Muramoto, M. Kimura, S. Nouda, *Development and future of ultraviolet light-emitting diodes: UV-LED will replace the UV lamp*, Semiconductor Science and Technology **29**, 084004 (2014).
- [6] M. A. Khan, M. Shatalov, H. P. Maruska, H. M. Wang, E. Kuokstis, *III-Nitride UV Devices*, Japanese Journal of Applied Physics **44**, 7191 (2005).
- [7] J. Rass, T. Kolbe, N. Lobo-Ploch, T. Wernicke, F. Mehnke, C. Kuhn, J. Enslin, M. Guttman, C. Reich, A. Mogilatenko, J. Glaab, C. Stoelmacker, M. Lapeyrade, S. Einfeldt, M. Weyers, M. Kneissl, *High-power UV-B LEDs with long lifetime*, Proc. SPIE **9363**, 93631K (2015).

-
- [8] P. J. Hargis, T. J. Sobering, G. C. Tisone, J. S. Wagner, S. A. Young, R. J. Radloff, *Ultraviolet fluorescence identification of protein, DNA, and bacteria*, Proc. SPIE **2366**, 147 (1995).
- [9] J. C. Chang, S. F. Ossoff, D. C. Lobe, M. H. Dorfman, C. M. Dumais, R. G. Qualls, J. D. Johnson, *UV inactivation of pathogenic and indicator microorganisms*, Applied and Environmental Microbiology **49**, 1361 (1985).
- [10] Y. W. Lee, H. Do Yoon, J.-H. Park, U.-C. Ryu, *Application of 265-nm UVC LED Lighting to Sterilization of Typical Gram Negative and Positive Bacteria*, Journal of the Korean Physical Society **72**, 1174 (2018).
- [11] K. Song, M. Mohseni, F. Taghipour, *Application of ultraviolet light-emitting diodes (UV-LEDs) for water disinfection: A review*, Water Research **94**, 341 (2016).
- [12] S. Vilhunen, H. Särkkä, M. Sillanpää, *Ultraviolet light-emitting diodes in water disinfection*, Environmental Science and Pollution Research **16**, 439 (2009).
- [13] M. Würtele, T. Kolbe, M. Lipsz, A. Külberg, M. Weyers, M. Kneissl, M. Jekel, *Application of GaN-based ultraviolet-C light emitting diodes – UV LEDs – for water disinfection*, Water Research **45**, 1481 (2011).
- [14] G. Y. Lui, D. Roser, R. Corkish, N. Ashbolt, P. Jagals, R. Stuetz, *Photovoltaic powered ultraviolet and visible light-emitting diodes for sustainable point-of-use disinfection of drinking waters*, Science of The Total Environment **493**, 185 (2014).
- [15] Z. Du, L. Wang, S. Chauchemez, X. Xu, X. Wang, B. Cowling, L. Meyers, *Risk for Transportation of 2019 Novel Coronavirus Disease From Wuhan to Other Cities in China*, Emerging Infectious Diseases **26**, 5 (2020).
- [16] World Health Organization, *Coronavirus disease 2019 (COVID-19) Situation Report – 130*, (2020).
- [17] F. Wu, S. Zhao, B. Yu, Y.-M. Chen, W. Wang, Z.-G. Song, Y. Hu, Z.-W. Tao, J.-H. Tian, Y.-Y. Pei, M. Yuan, Y. Zhang, F. Dai, Y. Liu, Q. Wang, J. Zheng, L. Xu, E. Holmes, Y. Zhang, *A new coronavirus associated with human respiratory disease in China*, Nature **579**, 265 (2020).

-
- [18] M. E. Darnell, K. Subbarao, S. M. Feinstone, D. R. Taylor, *Inactivation of the coronavirus that induces severe acute respiratory syndrome, SARS-CoV*, Journal of Virological Methods **121**, 85 (2004).
- [19] S. Duan, X. Zhao, R. Wen, J.-J. Huang, G. Pi, S. Zhang, J. Han, S. Bi, L. Ruan, X.-P. Dong et al., *Stability of SARS coronavirus in human specimens and environment and its sensitivity to heating and UV irradiation*, Biomedical and Environmental Sciences **16**, 246 (2003).
- [20] Y. Tsunetsugu-Yokota, *Large-scale preparation of UV-inactivated SARS coronavirus virions for vaccine antigen*, in *SARS-and Other Coronaviruses*, pages 119–126 (Springer, 2008).
- [21] K. Bedell, A. H. Buchaklian, S. Perlman, *Efficacy of an Automated Multiple Emitter Whole-Room Ultraviolet-C Disinfection System Against Coronaviruses MHV and MERS-CoV*, Infection Control and Hospital Epidemiology **37**, 598 (2016).
- [22] T. Takano, T. Mino, J. Sakai, N. Noguchi, K. Tsubaki, H. Hirayama, *Deep-ultraviolet light-emitting diodes with external quantum efficiency higher than 20% at 275 nm achieved by improving light-extraction efficiency*, Applied Physics Express **10**, 031002 (2017).
- [23] S.-I. Inoue, T. Naoki, T. Kinoshita, T. Obata, H. Yanagi, *Light extraction enhancement of 265 nm deep-ultraviolet light-emitting diodes with over 90 mW output power via an AlN hybrid nanostructure*, Applied Physics Letters **106**, 131104 (2015).
- [24] M. Kneissl, *UV LED Efficiency November 2018*, <https://www.ifkp.tu-berlin.de/menue/arbeitsgruppen/agkneissl/> (08.03.2020).
- [25] S. Nakamura, T. Mukai, M. Senoh, N. Iwasa, *Thermal Annealing Effects on P-Type Mg-Doped GaN Films*, Japanese Journal of Applied Physics **31**, L139 (1992).
- [26] F. Mireles, S. E. Ulloa, *Acceptor binding energies in GaN and AlN*, Physical Review B **58**, 3879 (1998).
- [27] Y. Taniyasu, M. Kasu, T. Makimoto, *An aluminium nitride light-emitting diode with a wavelength of 210 nanometres*, Nature **441**, 325 (2006).

-
- [28] J. Stellmach, M. Pristovsek, O. Savas, J. Schlegel, E. Yakovlev, M. Kneissl, *High aluminium content and high growth rates of AlGaN in a close-coupled showerhead MOVPE reactor*, Journal of Crystal Growth **315**, 229 (2011).
- [29] D. F. Davidson, K. Kohse-Höinghaus, A. Y. Chang, R. K. Hanson, *A pyrolysis mechanism for ammonia*, International Journal of Chemical Kinetics **22**, 513 (1990).
- [30] N. Dietz, M. Straßburg, V. Woods, *Real-time optical monitoring of ammonia flow and decomposition kinetics under high-pressure chemical vapor deposition conditions*, Journal of Vacuum Science & Technology A **23**, 1221 (2005).
- [31] U. W. Pohl, *Epitaxy of Semiconductors: Introduction to Physical Principles*, Graduate texts in physics (Springer, 2013).
- [32] F. Brunner, V. Hoffmann, A. Knauer, E. Steimetz, T. Schenk, J.-T. Zettler, M. Weyers, *Growth optimization during III-nitride multiwafer MOVPE using real-time curvature, reflectance and true temperature measurements*, Journal of Crystal Growth **298**, 202 (2007).
- [33] F. Brunner, A. Knauer, T. Schenk, M. Weyers, J.-T. Zettler, *Quantitative analysis of in situ wafer bowing measurements for III-nitride growth on sapphire*, Journal of Crystal Growth **310**, 2432 (2008).
- [34] F. Brunner, A. Mogilatenko, A. Knauer, M. Weyers, J.-T. Zettler, *Analysis of doping induced wafer bow during GaN:Si growth on sapphire*, Journal of Applied Physics **112**, 033503 (2012).
- [35] V. Hoffmann, A. Mogilatenko, U. Zeimer, S. Einfeldt, M. Weyers, M. Kneissl, *In-situ observation of InGaN quantum well decomposition during growth of laser diodes*, Crystal Research and Technology **50**, 499 (2015).
- [36] M. A. Moram, M. E. Vickers, *X-ray diffraction of III-nitrides*, Reports on Progress in Physics **72**, 036502 (2009).
- [37] F. Bernardini, V. Fiorentini, D. Vanderbilt, *Spontaneous polarization and piezoelectric constants of III-V nitrides*, Physical Review B **56**, R10024 (1997).

-
- [38] O. Ambacher, J. Smart, J. R. Shealy, N. G. Weimann, K. Chu, M. Murphy, W. J. Schaff, L. F. Eastman, R. Dimitrov, L. Wittmer, M. Stutzmann, W. Rieger, J. Hilsenbeck, *Two-dimensional electron gases induced by spontaneous and piezoelectric polarization charges in N- and Ga-face Al-GaN/GaN heterostructures*, Journal of Applied Physics **85**, 3222 (1999).
- [39] Simulations are based on the software package SiLENSe 5.8 (STR Group, Ltd.).
- [40] M. Rychetsky, I. Koslow, B. Avinc, J. Rass, T. Wernicke, K. Bellmann, L. Sulmoni, V. Hoffmann, M. Weyers, J. Wild, J. Zweck, B. Witzigmann, M. Kneissl, *Determination of polarization fields in group III-nitride heterostructures by capacitance-voltage-measurements*, Journal of Applied Physics **119**, 095713 (2016).
- [41] D. A. B. Miller, D. S. Chemla, T. C. Damen, A. C. Gossard, W. Wiegmann, T. H. Wood, C. A. Burrus, *Electric field dependence of optical absorption near the band gap of quantum-well structures*, Physical Review B **32**, 1043 (1985).
- [42] D. A. B. Miller, D. S. Chemla, T. C. Damen, A. C. Gossard, W. Wiegmann, T. H. Wood, C. A. Burrus, *Band-Edge Electroabsorption in Quantum Well Structures: The Quantum-Confined Stark Effect*, Physical Review Letters **53**, 2173 (1984).
- [43] T. Takeuchi, S. Sota, M. Katsuragawa, M. Komori, H. Takeuchi, H. Amano, I. Akasaki, *Quantum-confined Stark effect due to piezoelectric fields in GaInN strained quantum wells*, Japanese Journal of Applied Physics **36**, L382 (1997).
- [44] M. Feneberg, K. Thonke, *Polarization fields of III-nitrides grown in different crystal orientations*, Journal of Physics: Condensed Matter **19**, 403201 (2007).
- [45] C. E. Dreyer, A. Janotti, C. G. Van de Walle, D. Vanderbilt, *Correct Implementation of Polarization Constants in Wurtzite Materials and Impact on III-Nitrides*, Physical Review X **6**, 021038 (2016).
- [46] O. Ambacher, J. Majewski, C. Miskys, A. Link, M. Hermann, M. Eickhoff, M. Stutzmann, F. Bernardini, V. Fiorentini, V. Tilak, B. Schaff, L. East-

-
- man, *Pyroelectric properties of Al(In)GaN/GaN hetero- and quantum well structures*, Journal of Physics: Condensed Matter **14**, 3399 (2002).
- [47] W. Gordy, W. O. Thomas, *Electronegativities of the elements*, The Journal of Chemical Physics **24**, 439 (1956).
- [48] H. Angerer, D. Brunner, F. Freudenberg, O. Ambacher, M. Stutzmann, R. Höppler, T. Metzger, E. Born, G. Dollinger, A. Bergmaier, S. Karsch, H.-J. Körner, *Determination of the Al mole fraction and the band gap bowing of epitaxial $Al_xGa_{1-x}N$ films*, Applied Physics Letters **71**, 1504 (1997).
- [49] R. M. Martin, *Piezoelectricity*, Physical Review B **5**, 1607 (1972).
- [50] D. Vanderbilt, *Berry-phase theory of proper piezoelectric response*, Journal of Physics and Chemistry of Solids **61**, 147 (2000).
- [51] F. Mehnke, *Design, Epitaxie und Charakterisierung AlGaN-basierter Leuchtdioden mit Emissionswellenlängen unterhalb von 250 nm*, Dissertation, Technische Universität Berlin (2017).
- [52] W. Bludau, A. Onton, W. Heinke, *Temperature dependence of the band gap of silicon*, Journal of Applied Physics **45**, 1846 (1974).
- [53] H. Morkoç, S. Strite, G. B. Gao, M. E. Lin, B. Sverdlov, M. Burns, *Large-band-gap SiC, III-V nitride, and II-VI ZnSe-based semiconductor device technologies*, Journal of Applied Physics **76**, 1363 (1994).
- [54] I. Vurgaftman, J. R. Meyer, *Band parameters for nitrogen-containing semiconductors*, Journal of Applied Physics **94**, 3675 (2003).
- [55] R. T. Bondokov, S. G. Mueller, K. E. Morgan, G. A. Slack, S. Schujman, M. C. Wood, J. A. Smart, L. J. Schowalter, *Large-area AlN substrates for electronic applications: An industrial perspective*, Journal of Crystal Growth **310**, 4020 (2008).
- [56] P. Lu, R. Collazo, R. F. Dalmau, G. Durkaya, N. Dietz, Z. Sitar, *Different optical absorption edges in AlN bulk crystals grown in *m*- and *c*-orientations*, Applied Physics Letters **93**, 131922 (2008).
- [57] M. Bickermann, B. M. Epelbaum, O. Filip, P. Heimann, S. Nagata, A. Winnacker, *Point defect content and optical transitions in bulk aluminum nitride crystals*, Physica Status Solidi B **246**, 1181 (2009).

-
- [58] M. Bickermann, B. M. Epelbaum, O. Filip, P. Heimann, S. Nagata, A. Winnacker, *UV transparent single-crystalline bulk AlN substrates*, Physica Status Solidi C **7**, 21 (2010).
- [59] R. Moser, N. Ojha, M. Kunzer, U. T. Schwarz, *Sub-surface channels in sapphire made by ultraviolet picosecond laser irradiation and selective etching*, Optics Express **19**, 24738 (2011).
- [60] M. Kneissl, T. Kolbe, C. Chua, V. Kueller, N. Lobo, J. Stellmach, A. Knauer, H. Rodriguez, S. Einfeldt, Z. Yang, N. M. Johnson, M. Weyers, *Advances in group III-nitride-based deep UV light-emitting diode technology*, Semiconductor Science and Technology **26**, 014036 (2010).
- [61] O. Reentilä, F. Brunner, A. Knauer, A. Mogilatenko, W. Neumann, H. Protzmann, M. Heuken, M. Kneissl, M. Weyers, G. Tränkle, *Effect of the AlN nucleation layer growth on AlN material quality*, Journal of Crystal Growth **310**, 4932 (2008).
- [62] S. Y. Karpov, Y. N. Makarov, *Dislocation effect on light emission efficiency in gallium nitride*, Applied Physics Letters **81**, 4721 (2002).
- [63] A. Knauer, A. Mogilatenko, S. Hagedorn, J. Enslin, T. Wernicke, M. Kneissl, M. Weyers, *Correlation of sapphire off-cut and reduction of defect density in MOVPE grown AlN*, Physica Status Solidi B **253**, 809 (2016).
- [64] M. Funato, M. Shibaoka, Y. Kawakami, *Heteroepitaxy mechanisms of AlN on nitridated c-and a-plane sapphire substrates*, Journal of Applied Physics **121**, 085304 (2017).
- [65] N. Okada, N. Kato, S. Sato, T. Sumii, T. Nagai, N. Fujimoto, M. Imura, K. Balakrishnan, M. Iwaya, S. Kamiyama, H. Amano, I. Akasaki, H. Maruyama, T. Takagi, T. Noro, A. Bandoh, *Growth of high-quality and crack free AlN layers on sapphire substrate by multi-growth mode modification*, Journal of Crystal Growth **298**, 349 (2007).
- [66] N. Susilo, S. Hagedorn, D. Jaeger, H. Miyake, U. Zeimer, C. Reich, B. Neuschulz, L. Sulmoni, M. Guttman, F. Mehnke, C. Kuhn, T. Wernicke, M. Weyers, M. Kneissl, *AlGaIn-based deep UV LEDs grown on sputtered and high temperature annealed AlN/sapphire*, Applied Physics Letters **112**, 041110 (2018).

-
- [67] H. Hirayama, S. Fujikawa, J. Norimatsu, T. Takano, K. Tsubaki, N. Kamata, *Fabrication of a low threading dislocation density ELO-AlN template for application to deep-UV LEDs*, *Physica Status Solidi C* **6**, 356 (2009).
- [68] V. Küller, *Versetzungsreduzierte AlN- und AlGaN-Schichten als Basis für UV LEDs*, Dissertation, Technische Universität Berlin (2014).
- [69] H. Miyake, G. Nishio, S. Suzuki, K. Hiramatsu, H. Fukuyama, J. Kaur, N. Kuwano, *Annealing of an AlN buffer layer in N₂-CO for growth of a high-quality AlN film on sapphire*, *Applied Physics Express* **9**, 025501 (2016).
- [70] H. Miyake, C.-H. Lin, K. Tokoro, K. Hiramatsu, *Preparation of high-quality AlN on sapphire by high-temperature face-to-face annealing*, *Journal of Crystal Growth* **456**, 155 (2016).
- [71] S. Walde, S. Hagedorn, M. Weyers, *Impact of intermediate high temperature annealing on the properties of AlN/sapphire templates grown by metalorganic vapor phase epitaxy*, *Japanese Journal of Applied Physics* **58**, SC1002 (2019).
- [72] M. Imura, K. Nakano, N. Fujimoto, N. Okada, K. Balakrishnan, M. Iwaya, S. Kamiyama, H. Amano, I. Akasaki, T. Noro, T. Takagi, A. Bandoh, *High-Temperature Metal-Organic Vapor Phase Epitaxial Growth of AlN on Sapphire by Multi Transition Growth Mode Method Varying V/III Ratio*, *Japanese Journal of Applied Physics* **45**, 8639 (2006).
- [73] V. Kueller, A. Knauer, F. Brunner, U. Zeimer, H. Rodriguez, M. Kneissl, M. Weyers, *Growth of AlGaN and AlN on patterned AlN/sapphire templates*, *Journal of Crystal Growth* **315**, 200 (2011).
- [74] U. Zeimer, V. Kueller, A. Knauer, A. Mogilatenko, M. Weyers, M. Kneissl, *High quality AlGaN grown on ELO AlN/sapphire templates*, *Journal of Crystal Growth* **377**, 32 (2013).
- [75] M. Hayakawa, S. Ichikawa, M. Funato, Y. Kawakami, *Al_xGa_{1-x}N-Based Quantum Wells Fabricated on Macrosteps Effectively Suppressing Nonradiative Recombination*, *Advanced Optical Materials* **7**, 1801106 (2019).
- [76] B. Pantha, R. Dahal, M. Nakarmi, N. Nepal, J. Li, J. Lin, H. Jiang, Q. Paduano, D. Weyburne, *Correlation between optoelectronic and struc-*

-
- tural properties and epilayer thickness of AlN*, Applied Physics Letters **90**, 241101 (2007).
- [77] S. R. Lee, A. M. West, A. A. Allerman, K. E. Waldrip, D. M. Follstaedt, P. P. Provencio, D. D. Koleske, C. R. Abernathy, *Effect of threading dislocations on the Bragg peakwidths of GaN, AlGa_N, and AlN heterolayers*, Applied Physics Letters **86**, 241904 (2005).
- [78] K. Shojiki, R. Ishii, K. Uesugi, M. Funato, Y. Kawakami, H. Miyake, *Impact of face-to-face annealed sputtered AlN on the optical properties of AlGa_N multiple quantum wells*, AIP Advances **9**, 125342 (2019).
- [79] G. Kusch, M. Nouf-Allahiani, F. Mehnke, C. Kuhn, P. R. Edwards, T. Wernicke, A. Knauer, V. Kueller, G. Naresh-Kumar, M. Weyers, M. Kneissl, C. Trager-Cowan, R. W. Martin, *Spatial clustering of defect luminescence centers in Si-doped low resistivity Al_{0.82}Ga_{0.18}N*, Applied Physics Letters **107**, 072103 (2015).
- [80] U. Zeimer, J. Jeschke, A. Mogilatenko, A. Knauer, V. Kueller, V. Hoffmann, C. Kuhn, T. Simoneit, M. Martens, T. Wernicke, M. Kneissl, M. Weyers, *Spatial inhomogeneities in Al_xGa_{1-x}N quantum wells induced by the surface morphology of AlN/sapphire templates*, Semiconductor Science and Technology **30**, 114008 (2015).
- [81] B. Heying, E. J. Tarsa, C. R. Elsass, P. Fini, S. P. DenBaars, J. S. Speck, *Dislocation mediated surface morphology of GaN*, Journal of Applied Physics **85**, 6470 (1999).
- [82] J. Mickevičius, G. Tamulaitis, M. Shur, M. Shatalov, J. Yang, R. Gaska, *Internal quantum efficiency in AlGa_N with strong carrier localization*, Applied Physics Letters **101**, 211902 (2012).
- [83] M. Shatalov, W. Sun, A. Lunev, X. Hu, A. Dobrinsky, Y. Bilenko, J. Yang, M. Shur, R. Gaska, C. Moe, G. Garrett, M. Wraback, *AlGa_N Deep-Ultraviolet Light-Emitting Diodes with External Quantum Efficiency above 10%*, Applied Physics Express **5**, 082101 (2012).
- [84] R. G. Banal, M. Funato, Y. Kawakami, *Extremely high internal quantum efficiencies from AlGa_N/AlN quantum wells emitting in the deep ultraviolet spectral region*, Applied Physics Letters **99**, 011902 (2011).

-
- [85] Y. Iwata, R. G. Banal, S. Ichikawa, M. Funato, Y. Kawakami, *Emission mechanisms in Al-rich AlGa_N/AlN quantum wells assessed by excitation power dependent photoluminescence spectroscopy*, Journal of Applied Physics **117**, 075701 (2015).
- [86] F. Nippert, M. Tollabi Mazraehno, M. J. Davies, M. P. Hoffmann, H.-J. Lugauer, T. Kure, M. Kneissl, A. Hoffmann, M. R. Wagner, *Auger recombination in AlGa_N quantum wells for UV light-emitting diodes*, Applied Physics Letters **113**, 071107 (2018).
- [87] T. Kohno, Y. Sudo, M. Yamauchi, K. Mitsui, H. Kudo, H. Okagawa, Y. Yamada, *Internal Quantum Efficiency and Nonradiative Recombination Rate in InGa_N-Based Near-Ultraviolet Light-Emitting Diodes*, Japanese Journal of Applied Physics **51**, 072102 (2012).
- [88] T. Lu, Z. Ma, C. Du, Y. Fang, H. Wu, Y. Jiang, L. Wang, L. Dai, H. Jia, W. Liu, H. Chen, *Temperature-dependent photoluminescence in light-emitting diodes*, Scientific reports **4**, 1 (2014).
- [89] Y.-J. Lee, J. Hwang, T. Hsu, M. Hsieh, M. Jou, B. Lee, T. Lu, H. Kuo, S. Wang, *Enhancing the output power of Ga_N-based LEDs grown on wet-etched patterned sapphire substrates*, IEEE Photonics Technology Letters **18**, 1152 (2006).
- [90] M. Yamada, T. Mitani, Y. Narukawa, S. Shioji, I. Niki, S. Sonobe, K. Deguchi, M. Sano, T. Mukai, *InGa_N-based near-ultraviolet and blue-light-emitting diodes with high external quantum efficiency using a patterned sapphire substrate and a mesh electrode*, Japanese Journal of Applied Physics **41**, L1431 (2002).
- [91] M. Guttman, F. Mehnke, B. Belde, F. Wolf, C. Reich, L. Sulmoni, T. Wernicke, M. Kneissl, *Optical light polarization and light extraction efficiency of AlGa_N-based LEDs emitting between 264 and 220 nm*, Japanese Journal of Applied Physics **58**, SCCB20 (2019).
- [92] C. Reich, M. Guttman, M. Feneberg, T. Wernicke, F. Mehnke, C. Kuhn, J. Rass, M. Lapeyrade, S. Einfeldt, A. Knauer, V. Kueller, M. Weyers, R. Goldhahn, M. Kneissl, *Strongly transverse-electric-polarized emission from deep ultraviolet AlGa_N quantum well light emitting diodes*, Applied Physics Letters **107**, 142101 (2015).

-
- [93] R. Yoshizawa, H. Miyake, K. Hiramatsu, *Effect of thermal annealing on AlN films grown on sputtered AlN templates by metalorganic vapor phase epitaxy*, Japanese Journal of Applied Physics **57**, 01AD05 (2017).
- [94] J. Northrup, C. Chua, Z. Yang, T. Wunderer, M. Kneissl, N. Johnson, T. Kolbe, *Effect of strain and barrier composition on the polarization of light emission from AlGa_N/AlN quantum wells*, Applied Physics Letters **100**, 021101 (2012).
- [95] M. Funato, K. Matsuda, R. G. Banal, R. Ishii, Y. Kawakami, *Strong optical polarization in nonpolar (1 $\bar{1}$ 00) Al_xGa_{1-x}N/AlN quantum wells*, Physical Review B **87**, 041306 (2013).
- [96] A. Mogilatenko, V. Küller, A. Knauer, J. Jeschke, U. Zeimer, M. Weyers, G. Tränkle, *Defect analysis in AlGa_N layers on AlN templates obtained by epitaxial lateral overgrowth*, Journal of Crystal Growth **402**, 222 (2014).
- [97] V. Voronkov, *Formation of voids and oxide particles in silicon crystals*, Materials Science and Engineering: B **73**, 69 (2000).
- [98] Y. Taniyasu, M. Kasu, T. Makimoto, *Increased electron mobility in n-type Si-doped AlN by reducing dislocation density*, Applied Physics Letters **89**, 182112 (2006).
- [99] R. Collazo, S. Mita, J. Xie, A. Rice, J. Tweedie, R. Dalmau, Z. Sitar, *Progress on n-type doping of AlGa_N alloys on AlN single crystal substrates for UV optoelectronic applications*, Physica Status Solidi C **8**, 2031 (2011).
- [100] N. Susilo, E. Ziffer, S. Hagedorn, L. Cancellara, C. Netzel, N. L. Ploch, S. Wu, J. Rass, S. Walde, L. Sulmoni, M. Guttmann, T. Wernicke, M. Albrecht, M. Weyers, M. Kneissl, *Improved performance of UVC-LEDs by combination of high-temperature annealing and epitaxially laterally overgrown AlN/sapphire*, Photonics Research **8**, 589 (2020).
- [101] E. F. Schubert, J. K. Kim, J.-Q. Xi, *Low-refractive-index materials: A new class of optical thin-film materials*, Physica Status Solidi B **244**, 3002 (2007).
- [102] C. F. Shen, S. J. Chang, W. S. Chen, T. K. Ko, C. T. Kuo, S. C. Shei, *Nitride-Based High-Power Flip-Chip LED With Double-Side Patterned Sapphire Substrate*, IEEE Photonics Technology Letters **19**, 780 (2007).

-
- [103] S. Nagai, K. Yamada, A. Hirano, M. Ippommatsu, M. Ito, N. Morishima, K. Aosaki, Y. Honda, H. Amano, I. Akasaki, *Development of highly durable deep-ultraviolet AlGa_N-based LED multichip array with hemispherical encapsulated structures using a selected resin through a detailed feasibility study*, Japanese Journal of Applied Physics **55**, 082101 (2016).
- [104] C. Pernot, M. Kim, S. Fukahori, T. Inazu, T. Fujita, Y. Nagasawa, A. Hirano, M. Ippommatsu, M. Iwaya, S. Kamiyama, I. Akasaki, H. Amano, *Improved Efficiency of 255–280 nm AlGa_N-Based Light-Emitting Diodes*, Applied Physics Express **3**, 061004 (2010).
- [105] C. Pernot, S. Fukahori, T. Inazu, T. Fujita, M. Kim, Y. Nagasawa, A. Hirano, M. Ippommatsu, M. Iwaya, S. Kamiyama, I. Akasaki, H. Amano, *Development of high efficiency 255–355 nm AlGa_N-based light-emitting diodes*, Physica Status Solidi A **208**, 1594 (2011).
- [106] J. Glaab, J. Haefke, J. Ruschel, M. Brendel, J. Rass, T. Kolbe, A. Knauer, M. Weyers, S. Einfeldt, M. Guttmann, C. Kuhn, J. Enslin, T. Wernicke, M. Kneissl, *Degradation effects of the active region in UV-C light-emitting diodes*, Journal of Applied Physics **123**, 104502 (2018).
- [107] J. Ruschel, J. Glaab, M. Brendel, J. Rass, C. Stölmacker, N. Lobo-Ploch, T. Kolbe, T. Wernicke, F. Mehnke, J. Enslin, S. Einfeldt, M. Weyers, M. Kneissl, *Localization of current-induced degradation effects in (InAlGa)_N-based UV-B LEDs*, Journal of Applied Physics **124**, 084504 (2018).
- [108] M. Meneghini, D. Barbisan, L. Rodighiero, G. Meneghesso, E. Zanoni, *Analysis of the physical processes responsible for the degradation of deep-ultraviolet light emitting diodes*, Applied Physics Letters **97**, 143506 (2010).
- [109] J. Glaab, C. Ploch, R. Kelz, C. Stölmacker, M. Lapeyrade, N. Lobo-Ploch, J. Rass, T. Kolbe, S. Einfeldt, F. Mehnke, C. Kuhn, T. Wernicke, M. Weyers, M. Kneissl, *Degradation of (InAlGa)_N-based UV-B light emitting diodes stressed by current and temperature*, Journal of Applied Physics **118**, 094504 (2015).
- [110] C. G. Moe, M. L. Reed, G. A. Garrett, A. V. Sampath, T. Alexander, H. Shen, M. Wraback, Y. Bilenko, M. Shatalov, J. Yang, W. Sun, J. Deng, R. Gaska, *Current-induced degradation of high performance deep ultraviolet light emitting diodes*, Applied Physics Letters **96**, 213512 (2010).

-
- [111] A. Pinos, S. Marcinkevičius, M. S. Shur, *High current-induced degradation of AlGa_N ultraviolet light emitting diodes*, Journal of Applied Physics **109**, 103108 (2011).
- [112] S. Sawyer, S. Rumyantsev, M. Shur, *Degradation of AlGa_N-based ultraviolet light emitting diodes*, Solid-State Electronics **52**, 968 (2008).
- [113] F. Manyakhin, A. Kovalev, A. E. Yunovich, *Aging Mechanisms of In-GaN/AlGa_N/Ga_N Light-Emitting Diodes Operating at High Currents*, MRS Internet Journal of Nitride Semiconductor Research **3**, e53 (1998).
- [114] M. Meneghini, L. Rigutti, L. R. Trevisanello, A. Cavallini, G. Meneghesso, E. Zanoni, *A model for the thermal degradation of metal/(p-GaN) interface in Ga_N-based light emitting diodes*, Journal of Applied Physics **103**, 063703 (2008).
- [115] J. Glaab, J. Ruschel, T. Kolbe, A. Knauer, J. Rass, H. K. Cho, N. Lobo-Ploch, S. Kreuzmann, S. Einfeldt, M. Weyers, M. Kneissl, *Degradation of (In)AlGa_N-Based UVB LEDs and Migration of Hydrogen*, IEEE Photonics Technology Letters **31**, 529 (2019).
- [116] J. Ruschel, J. Glaab, B. Beidoun, N. Lobo-Ploch, J. Rass, T. Kolbe, A. Knauer, M. Weyers, S. Einfeldt, M. Kneissl, *Current-induced degradation and lifetime prediction of 310 nm ultraviolet light-emitting diodes*, Photonics Research **7**, B36 (2019).
- [117] F. Mehnke, T. Wernicke, H. Pingel, C. Kuhn, C. Reich, V. Kueller, A. Knauer, M. Lapeyrade, M. Weyers, M. Kneissl, *Highly conductive n-Al_xGa_{1-x}N layers with aluminum mole fractions above 80%*, Applied Physics Letters **103**, 212109 (2013).
- [118] C. Kuhn, T. Simoneit, M. Martens, T. Markurt, J. Enslin, F. Mehnke, K. Bellmann, T. Schulz, M. Albrecht, T. Wernicke, M. Kneissl, *MOVPE Growth of Smooth and Homogeneous Al_{0.8}Ga_{0.2}N:Si Superlattices as UVC Laser Cladding Layers*, Physica Status Solidi A **215**, 1800005 (2018).
- [119] J. Enslin, F. Mehnke, A. Mogilatenko, K. Bellmann, M. Guttman, C. Kuhn, J. Rass, N. Lobo-Ploch, T. Wernicke, M. Weyers, M. Kneissl, *Metamorphic Al_{0.5}Ga_{0.5}N:Si on AlN/sapphire for the growth of UVB LEDs*, Journal of Crystal Growth **464**, 185 (2017).

-
- [120] H.-M. Wang, J.-P. Zhang, C.-Q. Chen, Q. Fareed, J.-W. Yang, M. A. Khan, *AlN/AlGaN superlattices as dislocation filter for low-threading-dislocation thick AlGaN layers on sapphire*, Applied Physics Letters **81**, 604 (2002).
- [121] A. Mogilatenko, J. Enslin, A. Knauer, F. Mehnke, K. Bellmann, T. Wernicke, M. Weyers, M. Kneissl, *V-pit to truncated pyramid transition in AlGaN-based heterostructures*, Semiconductor Science and Technology **30**, 114010 (2015).
- [122] R. France, T. Xu, P. Chen, R. Chandrasekaran, T. Moustakas, *Vanadium-based Ohmic contacts to n-AlGaN in the entire alloy composition*, Applied Physics Letters **90**, 062115 (2007).
- [123] T. Wernicke, L. Sulmoni, C. Kuhn, G. Tränkle, M. Weyers, M. Kneissl, *Group III-Nitride-Based UV Laser Diodes*, in *Semiconductor Nanophotonics*, pages 505–548 (Springer, 2020).
- [124] L. Sulmoni, F. Mehnke, A. Mogilatenko, M. Guttman, T. Wernicke, M. Kneissl, *Electrical properties and microstructure formation of Vanadium-based n-contacts on high Al mole fraction n-AlGaN layers*, To be published.
- [125] S. Grabowski, M. Schneider, H. Nienhaus, W. Mönch, R. Dimitrov, O. Ambacher, M. Stutzmann, *Electron affinity of $Al_xGa_{1-x}N$ (0001) surfaces*, Applied Physics Letters **78**, 2503 (2001).
- [126] B. Van Daele, G. Van Tendeloo, W. Ruythooren, J. Derluyn, M. Leys, M. Germain, *The role of Al on Ohmic contact formation on n-type GaN and AlGaN/GaN*, Applied Physics Letters **87**, 061905 (2005).
- [127] A. Motayed, R. Bathe, M. C. Wood, O. S. Diouf, R. D. Vispute, S. N. Mohammad, *Electrical, thermal, and microstructural characteristics of Ti/Al/Ti/Au multilayer Ohmic contacts to n-type GaN*, Journal of Applied Physics **93**, 1087 (2003).
- [128] B. P. Luther, J. M. DeLucca, S. E. Mohny, R. F. Karlicek, *Analysis of a thin AlN interfacial layer in Ti/Al and Pd/Al ohmic contacts to n-type GaN*, Applied Physics Letters **71**, 3859 (1997).
- [129] S. Ruvimov, Z. Liliental-Weber, J. Washburn, D. Qiao, S. S. Lau, P. K. Chu, *Microstructure of Ti/Al ohmic contacts for n-AlGaN*, Applied Physics Letters **73**, 2582 (1998).

-
- [130] L. Wang, F. M. Mohammed, I. Adesida, *Differences in the reaction kinetics and contact formation mechanisms of annealed Ti/Al/Mo/Au Ohmic contacts on n-GaN and AlGaN/GaN epilayers*, Journal of Applied Physics **101**, 013702 (2007).
- [131] F. Mehnke, L. Sulmoni, M. Guttmann, T. Wernicke, M. Kneissl, *Influence of light absorption on the performance characteristics of UV LEDs with emission between 239 and 217 nm*, Applied Physics Express **12**, 012008 (2019).
- [132] I. Bryan, Z. Bryan, S. Washiyama, P. Reddy, B. Gaddy, B. Sarkar, M. H. Breckenridge, Q. Guo, M. Bobea, J. Tweedie, S. Mita, D. Irving, R. Collazo, Z. Sitar, *Doping and compensation in Al-rich AlGaN grown on single crystal AlN and sapphire by MOCVD*, Applied Physics Letters **112**, 062102 (2018).
- [133] T. Kolbe, A. Knauer, J. Enslin, S. Hagedorn, A. Mogilatenko, T. Wernicke, M. Kneissl, M. Weyers, *Influence of substrate off-cut angle on the performance of 310 nm light emitting diodes*, Journal of Crystal Growth **526**, 125241 (2019).
- [134] U. Zeimer, A. Mogilatenko, V. Kueller, A. Knauer, M. Weyers, *Cathodoluminescence and TEM investigations of structural and optical properties of AlGaN on epitaxial laterally overgrown AlN/sapphire templates*, Journal of Physics: Conference Series **471**, 012021 (2013).
- [135] G. Kusch, H. Li, P. R. Edwards, J. Bruckbauer, T. C. Sadler, P. J. Parbrook, R. W. Martin, *Influence of substrate miscut angle on surface morphology and luminescence properties of AlGaN*, Applied Physics Letters **104**, 092114 (2014).
- [136] I. Bryan, Z. Bryan, S. Mita, A. Rice, L. Hussey, C. Shelton, J. Tweedie, J.-P. Maria, R. Collazo, Z. Sitar, *The role of surface kinetics on composition and quality of AlGaN*, Journal of Crystal Growth **451**, 65 (2016).
- [137] I. Bryan, Z. Bryan, S. Mita, A. Rice, J. Tweedie, R. Collazo, Z. Sitar, *Surface kinetics in AlN growth: A universal model for the control of surface morphology in III-nitrides*, Journal of Crystal Growth **438**, 81 (2016).

-
- [138] S. Mita, R. Collazo, A. Rice, R. Dalmau, Z. Sitar, *Influence of gallium supersaturation on the properties of GaN grown by metalorganic chemical vapor deposition*, Journal of Applied Physics **104**, 013521 (2008).
- [139] W. Burton, N. Cabrera, F. Frank, *The growth of crystals and the equilibrium structure of their surfaces*, Philosophical Transactions of the Royal Society of London, Series A: Mathematical, Physical and Engineering Sciences **243**, 299 (1951).
- [140] M. A. Laurent, S. Keller, U. K. Mishra, *Comprehensive Analysis of Surface Morphology and Growth Mode of AlInGaN Films*, Physica Status Solidi A **216**, 1800523 (2019).
- [141] T. Zywietz, J. Neugebauer, M. Scheffler, *Adatom diffusion at GaN (0001) and (000 $\bar{1}$) surfaces*, Applied Physics Letters **73**, 487 (1998).
- [142] E. J. Tarsa, B. Heying, X. H. Wu, P. Fini, S. P. DenBaars, J. S. Speck, *Homoepitaxial growth of GaN under Ga-stable and N-stable conditions by plasma-assisted molecular beam epitaxy*, Journal of Applied Physics **82**, 5472 (1997).
- [143] F. Brunner, A. Mogilatenko, V. Kueller, A. Knauer, M. Weyers, *Stress evolution during $Al_xGa_{1-x}N/AlN$ growth on sapphire*, Journal of Crystal Growth **376**, 54 (2013).
- [144] S. F. Chichibu, A. Uedono, T. Onuma, B. A. Haskell, A. Chakraborty, T. Koyama, P. T. Fini, S. Keller, S. P. DenBaars, J. S. Speck, U. K. Mishra, S. Nakamura, S. Yamaguchi, S. Kamiyama, H. Amano, I. Akasaki, J. Han, T. Sota, *Origin of defect-insensitive emission probability in In-containing (Al,In,Ga)N alloy semiconductors*, Nature Materials **5**, 810 (2006).
- [145] D. M. Follstaedt, S. R. Lee, A. A. Allerman, J. A. Floro, *Strain relaxation in AlGa N multilayer structures by inclined dislocations*, Journal of Applied Physics **105**, 083507 (2009).
- [146] D. M. Follstaedt, S. R. Lee, P. P. Provencio, A. A. Allerman, J. A. Floro, M. H. Crawford, *Relaxation of compressively-strained AlGa N by inclined threading dislocations*, Applied Physics Letters **87**, 121112 (2005).
- [147] P. Cantu, F. Wu, P. Waltereit, S. Keller, A. E. Romanov, U. K. Mishra, S. P. DenBaars, J. S. Speck, *Si doping effect on strain reduction in compressively strained $Al_{0.49}Ga_{0.51}N$ thin films*, Applied Physics Letters **83**, 674 (2003).

-
- [148] A. E. Romanov, J. S. Speck, *Stress relaxation in mismatched layers due to threading dislocation inclination*, Applied Physics Letters **83**, 2569 (2003).
- [149] Y. Huang, K. W. Sun, A. M. Fischer, Q. Y. Wei, R. Juday, F. A. Ponce, R. Kato, T. Yokogawa, *Effect of misfit dislocations on luminescence in m-plane InGaN quantum wells*, Applied Physics Letters **98**, 261914 (2011).
- [150] Y. Kashima, N. Maeda, E. Matsuura, M. Jo, T. Iwai, T. Morita, M. Kokubo, T. Tashiro, R. Kamimura, Y. Osada, H. Takagi, H. Hirayama, *High external quantum efficiency (10%) AlGaIn-based deep-ultraviolet light-emitting diodes achieved by using highly reflective photonic crystal on p-AlGaIn contact layer*, Applied Physics Express **11**, 012101 (2017).
- [151] Evans Analytical Group, 4747 Executive Drive, Suite 700 San Diego, CA 92121, United States of America, www.eag.com.
- [152] F. Römer, B. Witzigmann, *Acceptor activation model for III-nitride LEDs*, Journal of Computational Electronics **14**, 456 (2015).
- [153] F. Bechstedt, U. Grossner, J. Furthmüller, *Dynamics and polarization of group-III nitride lattices: A first-principles study*, Physical Review B **62**, 8003 (2000).
- [154] M. Feneberg, M. F. Romero, M. Röppischer, C. Cobet, N. Esser, B. Neuschl, K. Thonke, M. Bickermann, R. Goldhahn, *Anisotropic absorption and emission of bulk (1 $\bar{1}$ 00) AlN*, Physical Review B **87**, 235209 (2013).
- [155] M. Feneberg, S. Osterburg, K. Lange, C. Lidig, B. Garke, R. Goldhahn, E. Richter, C. Netzel, M. D. Neumann, N. Esser, S. Fritze, H. Witte, J. Bläsing, A. Dadgar, A. Krost, *Band gap renormalization and Burstein-Moss effect in silicon- and germanium-doped wurtzite GaN up to 10^{20} cm $^{-3}$* , Physical Review B **90**, 075203 (2014).
- [156] T. Detchprohm, K. Hiramatsu, K. Itoh, I. Akasaki, *Relaxation Process of the Thermal Strain in the GaN/ α -Al $_2$ O $_3$ Heterostructure and Determination of the Intrinsic Lattice Constants of GaN Free from the Strain*, Japanese Journal of Applied Physics **31**, L1454 (1992).
- [157] A. Shikanai, T. Azuhata, T. Sota, S. Chichibu, A. Kuramata, K. Horino, S. Nakamura, *Biaxial strain dependence of exciton resonance energies in wurtzite GaN*, Journal of Applied Physics **81**, 417 (1997).

-
- [158] W. Shan, R. J. Hauenstein, A. J. Fischer, J. J. Song, W. G. Perry, M. D. Bremser, R. F. Davis, B. Goldenberg, *Strain effects on excitonic transitions in GaN: Deformation potentials*, Physical Review B **54**, 13460 (1996).
- [159] M. Frentrop, N. Hatui, T. Wernicke, J. Stellmach, A. Bhattacharya, M. Kneissl, *Determination of lattice parameters, strain state and composition in semipolar III-nitrides using high resolution X-ray diffraction*, Journal of Applied Physics **114**, 213509 (2013).
- [160] J.-F. Carlin, M. Ilegems, *High-quality AlInN for high index contrast Bragg mirrors lattice matched to GaN*, Applied Physics Letters **83**, 668 (2003).
- [161] K. Lorenz, N. Franco, E. Alves, I. Watson, R. Martin, K. O'Donnell, *Anomalous ion channeling in AlInN/GaN bilayers: determination of the strain state*, Physical Review Letters **97**, 085501 (2006).
- [162] Y. Taniyasu, J.-F. Carlin, A. Castiglia, R. Butté, N. Grandjean, *Mg doping for p-type AlInN lattice-matched to GaN*, Applied Physics Letters **101**, 082113 (2012).
- [163] L. Semra, A. Telia, M. Kaddeche, A. Soltani, *Effects of spontaneous and piezoelectric polarization on AlInN/GaN heterostructure*, IEEE International Conference on Engineering and Technology **1**, 1 (2012).
- [164] R. Butté, E. Feltn, J. Dorsaz, G. Christmann, J.-F. Carlin, N. Grandjean, M. Ilegems, *Recent Progress in the Growth of Highly Reflective Nitride-Based Distributed Bragg Reflectors and Their Use in Microcavities*, Japanese Journal of Applied Physics **44**, 7207 (2005).
- [165] P. Pampili, V. Z. Zubialevich, P. Maaskant, M. Akhter, B. Corbett, P. J. Parbrook, *InAlN-based LEDs emitting in the near-UV region*, Japanese Journal of Applied Physics **58**, SCCB33 (2019).
- [166] C. Hums, A. Gadanecz, A. Dadgar, J. Bläsing, P. Lorenz, S. Krischok, F. Bertram, A. Franke, J. Schaefer, J. Christen, A. Krost, *AlInN/GaN based multi quantum well structures—growth and optical properties*, Physica Status Solidi C **6**, S451 (2009).
- [167] V. Chin, T. Tansley, T. Osotchan, *Electron mobilities in gallium, indium, and aluminum nitrides*, Journal of Applied Physics **75**, 7365 (1994).

-
- [168] A. Zoroddu, F. Bernardini, P. Ruggerone, V. Fiorentini, *First-principles prediction of structure, energetics, formation enthalpy, elastic constants, polarization, and piezoelectric constants of AlN, GaN, and InN: Comparison of local and gradient-corrected density-functional theory*, Physical Review B **64**, 045208 (2001).
- [169] S. Nicolay, J.-F. Carlin, E. Feltin, R. Butté, M. Mosca, N. Grandjean, M. Illegems, M. Tchernycheva, L. Nevou, F. Julien, *Midinfrared intersub-band absorption in lattice-matched AlInN/GaN multiple quantum wells*, Applied Physics Letters **87**, 111106 (2005).
- [170] V. Hoffmann, A. Knauer, C. Brunner, S. Einfeldt, M. Weyers, G. Tränkle, K. Haberland, J.-T. Zettler, M. Kneissl, *Uniformity of the wafer surface temperature during MOVPE growth of GaN-based laser diode structures on GaN and sapphire substrate*, Journal of Crystal Growth **315**, 5 (2011).
- [171] T. Takeuchi, C. Wetzel, S. Yamaguchi, H. Sakai, H. Amano, I. Akasaki, Y. Kaneko, S. Nakagawa, Y. Yamaoka, N. Yamada, *Determination of piezoelectric fields in strained GaInN quantum wells using the quantum-confined Stark effect*, Applied Physics Letters **73**, 1691 (1998).
- [172] L. Houben, M. Luysberg, T. Brammer, *Illumination effects in holographic imaging of the electrostatic potential of defects and pn junctions in transmission electron microscopy*, Physical Review B **70**, 165313 (2004).
- [173] C. McAleese, P. M. F. J. Costa, D. M. Graham, H. Xiu, J. S. Barnard, M. J. Kappers, P. Dawson, M. J. Godfrey, C. J. Humphreys, *Electric fields in AlGaIn/GaN quantum well structures*, Physica Status Solidi B **243**, 1551 (2006).
- [174] C. Y. Lai, T. M. Hsu, W.-H. Chang, K.-U. Tseng, C.-M. Lee, C.-C. Chuo, J.-I. Chyi, *Direct measurement of piezoelectric field in $In_{0.23}Ga_{0.77}N/GaN$ multiple quantum wells by electrotransmission spectroscopy*, Journal of Applied Physics **91**, 531 (2002).
- [175] E. T. Yu, G. J. Sullivan, P. M. Asbeck, C. D. Wang, D. Qiao, S. S. Lau, *Measurement of piezoelectrically induced charge in GaN/AlGaIn heterostructure field-effect transistors*, Applied Physics Letters **71**, 2794 (1997).

-
- [176] O. Ambacher, B. Foutz, J. Smart, J. R. Shealy, N. G. Weimann, K. Chu, M. Murphy, A. J. Sierakowski, W. J. Schaff, L. F. Eastman, R. Dimitrov, A. Mitchell, M. Stutzmann, *Two dimensional electron gases induced by spontaneous and piezoelectric polarization in undoped and doped AlGa_N/Ga_N heterostructures*, Journal of Applied Physics **87**, 334 (2000).
- [177] S. L. Chuang, C. S. Chang, *k-p method for strained wurtzite semiconductors*, Physical Review B **54**, 2491 (1996).
- [178] M. Guttmann, J. Höpfner, C. Reich, L. Sulmoni, C. Kuhn, P. Röder, T. Wernicke, M. Kneissl, *Effect of quantum barrier composition on electro-optical properties of AlGa_N-based UVC light emitting diodes*, Semiconductor Science and Technology **34**, 085007 (2019).
- [179] H. Hirayama, N. Noguchi, T. Yatabe, N. Kamata, *227 nm AlGa_N Light-Emitting Diode with 0.15 mW Output Power Realized using a Thin Quantum Well and AlN Buffer with Reduced Threading Dislocation Density*, Applied Physics Express **1**, 051101 (2008).
- [180] H. Hirayama, S. Fujikawa, N. Noguchi, J. Norimatsu, T. Takano, K. Tsubaki, N. Kamata, *222–282 nm AlGa_N and InAlGa_N-based deep-UV LEDs fabricated on high-quality AlN on sapphire*, Physica Status Solidi A **206**, 1176 (2009).
- [181] A. Roble, S. Patra, F. Massabuau, M. Frentrup, M. Leontiadou, P. Dawson, M. Kappers, R. Oliver, D. Graham, S. Schulz, *Impact of alloy fluctuations and Coulomb effects on the electronic and optical properties of c-plane Ga_N/AlGa_N quantum wells*, Scientific Reports **9**, 1 (2019).
- [182] D. A. B. Miller, D. S. Chemla, S. Schmitt-Rink, *Relation between electroabsorption in bulk semiconductors and in quantum wells: The quantum-confined Franz-Keldysh effect*, Physical Review B **33**, 6976 (1986).
- [183] L. C. de Carvalho, A. Schleife, F. Bechstedt, *Influence of exchange and correlation on structural and electronic properties of AlN, GaN, and InN polytypes*, Physical Review B **84**, 195105 (2011).
- [184] H. Hirayama, T. Kyono, K. Akita, T. Nakamura, K. Ishibashi, *High-efficiency UV LEDs using quaternary InAlGa_N*, Electrical Engineering in Japan **157**, 43 (2006).

-
- [185] T. Kolbe, T. Sembdner, A. Knauer, V. Kueller, H. Rodriguez, S. Einfeldt, P. Vogt, M. Weyers, M. Kneissl, *(In)AlGaN deep ultraviolet light emitting diodes with optimized quantum well width*, Physica Status Solidi A **207**, 2198 (2010).
- [186] N. Susilo, J. Enslin, L. Sulmoni, M. Guttman, U. Zeimer, T. Wernicke, M. Weyers, M. Kneissl, *Effect of the GaN:Mg Contact Layer on the Light-Output and Current-Voltage Characteristic of UVB LEDs*, Physica Status Solidi A **215**, 1700643 (2018).
- [187] C. Kuhn, L. Sulmoni, M. Guttman, J. Glaab, N. Susilo, T. Wernicke, M. Weyers, M. Kneissl, *MOVPE-grown AlGa_N-based tunnel heterojunctions enabling fully transparent UVC LEDs*, Photonics Research **7**, B7 (2019).
- [188] M. Martens, C. Kuhn, E. Ziffer, T. Simoneit, V. Kueller, A. Knauer, J. Rass, T. Wernicke, S. Einfeldt, M. Weyers, M. Kneissl, *Low absorption loss p-AlGa_N superlattice cladding layer for current-injection deep ultraviolet laser diodes*, Applied Physics Letters **108**, 151108 (2016).
- [189] M. Martens, C. Kuhn, T. Simoneit, S. Hagedorn, A. Knauer, T. Wernicke, M. Weyers, M. Kneissl, *The effects of magnesium doping on the modal loss in AlGa_N-based deep UV lasers*, Applied Physics Letters **110**, 081103 (2017).
- [190] J. F. Muth, J. D. Brown, M. A. L. Johnson, Z. Yu, R. M. Kolbas, J. W. Cook, J. F. Schetzina, *Absorption Coefficient and Refractive Index of Ga_N, Al_N and AlGa_N Alloys*, MRS Internet Journal of Nitride Semiconductor Research **4**, 502 (1999).
- [191] K. Osamura, K. Nakajima, Y. Murakami, P. H. Shingu, A. Ohtsuki, *Fundamental absorption edge in Ga_N, In_N and their alloys*, Solid State Communications **11**, 617 (1972).
- [192] D. A. B. Miller, *Quantum mechanics for scientists and engineers* (Cambridge University Press, 2008).
- [193] H. K. Hughes, *Beer's Law and the Optimum Transmittance in Absorption Measurements*, Applied Optics **2**, 937 (1963).

-
- [194] M. Guttman, A. Susilo, L. Sulmoni, N. Susilo, Z. Eviathar, T. Wernicke, M. Kneissl, *Enhanced light extraction and internal quantum efficiency for fully-transparent AlGa_N-based UVC LEDs on patterned-AlN/sapphire substrate*, To be published.
- [195] J. Frenkel, *On Pre-Breakdown Phenomena in Insulators and Electronic Semi-Conductors*, Physical Review **54**, 647 (1938).
- [196] J. Hartke, *The three-dimensional Poole-Frenkel effect*, Journal of Applied Physics **39**, 4871 (1968).
- [197] M. Ieda, G. Sawa, S. Kato, *A Consideration of Poole-Frenkel Effect on Electric Conduction in Insulators*, Journal of Applied Physics **42**, 3737 (1971).
- [198] R. Gross, A. Marx, *Festkörperphysik* (Walter de Gruyter GmbH, 2014).
- [199] H. K. Cho, I. Ostermay, U. Zeimer, J. Enslin, T. Wernicke, S. Einfeldt, M. Weyers, M. Kneissl, *Highly Reflective p-Contacts Made of Pd-Al on Deep Ultraviolet Light-Emitting Diodes*, IEEE Photonics Technology Letters **29**, 2222 (2017).
- [200] M. Jo, N. Maeda, H. Hirayama, *Enhanced light extraction in 260 nm light-emitting diode with a highly transparent p-AlGa_N layer*, Applied Physics Express **9**, 012102 (2015).
- [201] H. K. Cho, N. Susilo, M. Guttman, J. Rass, I. Ostermay, S. Hagedorn, Z. Eviathar, T. Wernicke, S. Einfeldt, M. Weyers, M. Kneissl, *Enhanced light extraction efficiency and wall plug efficiency of AlGa_N-based deep-UV LEDs using Mo/Al as p-contact*, To be published.

List of Figures

1.1	Reported values of the EQE	2
1.2	Schematic of the UVC-LED heterostructures	7
1.3	Calculated profile of the conduction and valence band edges	8
1.4	c/a -ratio and bond length as a function of the Al mole fraction	10
1.5	Strained growth leading to a deformation of the tetrahedron	12
2.1	Face-to-face configuration during HTA	15
2.2	Schematic of the template fabrication process	16
2.3	Schematic of the MQW and UVC-LED heterostructure	17
2.4	AFM of SP AlN, before HTA, after HTA and after overgrowth	19
2.5	RC-FWHM of SP AlN before HTA and after HTA	20
2.6	Illustration of the SP AlN before and after HTA	21
2.7	AFM of the MQWs on ELO AlN and SP-HTA AlN	22
2.8	CL of the MQWs on ELO AlN and SP-HTA AlN	23
2.9	PL spectra and RRE of the MQWs on ELO AlN and SP-HTA AlN	25
2.10	LIV of the UVC-LED on ELO AlN and SP-HTA AlN	27
2.11	Schematic of the MQW and UVC-LED heterostructure	29
2.12	AFM of the MQWs HTA ELO AlN	31
2.13	CL of the MQWs on HTA ELO AlN	32
2.14	TEM of the MQWs on HTA ELO AlN	33
2.15	Depth distribution of the TDD of MQWs	34
2.16	RRE of the MQWs on HTA ELO AlN	35
2.17	LIV of UVC-LEDs on HTA ELO AlN	36
2.18	TDD determined by HRXRD, TEM and CL	38
2.19	LI of UVC-LED chips on ELO and HTA ELO	39
2.20	Degradation of UVC-LEDs on ELO AlN and HTA ELO	41
3.1	Schematic of the n -side and UVC-LED heterostructure	44
3.2	Surface morphology of the $\text{Al}_x\text{Ga}_{1-x}\text{N}:\text{Si}$ n -side samples	45
3.3	Transmission of the $\text{Al}_x\text{Ga}_{1-x}\text{N}:\text{Si}$ n -side samples	46
3.4	RSMs of the $\text{Al}_x\text{Ga}_{1-x}\text{N}:\text{Si}$ n -side samples	47
3.5	Emission power of UVC-LEDs with $\text{Al}_x\text{Ga}_{1-x}\text{N}:\text{Si}$ with varying x	48
3.6	TEM of UVC-LEDs with an $\text{Al}_{0.60}\text{Ga}_{0.40}\text{N}:\text{Si}$ and an $\text{Al}_{0.76}\text{Ga}_{0.24}\text{N}:\text{Si}$ layer	49
3.7	Scheme of the two-stage heterostructure approach for the n -side	50

3.8	ADF STEM images of the UVC-LED using a contact layer	51
3.9	Emission power of UVC-LEDs using a contact layer	52
3.10	LIV characteristics of UVC-LEDs with and without contact layer . . .	53
4.1	Charge density distribution within the depletion region	56
4.2	Relative error of the polarization field	61
4.3	Deviation of the determined capacitance	63
4.4	Schematic of the <i>pin</i> -diodes	66
4.5	TEM images of the InAlN layers	68
4.6	C^{-2} as a function of the bias voltage	69
4.7	Polarization fields determined with the CVM-based approaches (InAlN)	71
4.8	TEM images of the $\text{Al}_x\text{Ga}_{1-x}\text{N}$ double heterostructures	72
4.9	Polarization fields as a function of the position on a quarter wafer . .	74
4.10	Polarization fields determined by the CVM-based approaches (AlGaIn)	75
4.11	Polarization fields in an AlGaIn-based quantum well	77
4.12	STEM-HAADF images of an MQW heterostructure sample	78
4.13	Simulations of the emission wavelength and the wave function overlap	79
5.1	UVC-LED heterostructures with varying GaN:Mg thickness	84
5.2	AFM topograms of UVC-LEDs with varying GaN:Mg thickness	86
5.3	Transmissions of UVC-LED with different GaN:Mg thickness	87
5.4	Emission power as a function of the GaN:Mg contact layer thickness .	88
5.5	EQE and LEE as a function of the GaN:Mg thickness	90
5.6	IV characteristics of UVC-LEDs with different GaN:Mg thicknesses . .	91
5.7	UVC-LED chips results using a semi- and a non-transparent <i>p</i> -side . .	92

List of Abbreviations

ADF	annular dark-field
AFM	atomic force microscopy
Al	aluminium
AlGaN	aluminium gallium nitride
AlN	aluminium nitride
ArF	argon fluoride
Au	gold
CCS	close coupled showerhead
CIE	current injection efficiency
CL	cathodoluminescence
Cp ₂ Mg	cyclopentadienylmagnesium
CV	capacitance–voltage characteristics
CVM	capacitance-voltage measurements
cw	continuous wave
DFT	density-functional theory
EBL	electron blocking layer
EL	electroluminescence
ELO	epitaxial lateral overgrowth
EQE	external quantum efficiency
FBH	Ferdinand-Braun-Institut
FWHM	full width at half maximum
Ga	gallium
GaN	gallium nitride
H ₂	hydrogen gas
HAADF	high-angle annular dark-field
HRXRD	high-resolution X-ray diffraction
HTA	high temperature annealing
I-EQE	current-external quantum efficiency characteristics
I-WPE	current-wall plug efficiency characteristics
IKZ	Leibniz-Institut für Kristallzüchtung
InAlN	indium aluminium nitride
InGaN	indium gallium nitride
InN	indium nitride
IQE	internal quantum efficiency

IV	current–voltage characteristics
LED	light emitting diode
LEE	light extraction efficiency
LI	output power–current characteristics
LIV	output power–current–voltage characteristics
Mg	magnesium
MO	Molybdenum
MOVPE	metalorganic vapour phase epitaxy
MQW	multi quantum well
N	nitrogen
N ₂	nitrogen gas
NH ₃	ammonia
Ni	nickel
Pd	palladium
PL	photoluminescence
Pt	platinum
QCSE	quantum confined Stark effect
RC-FWHM	rocking curve full width at half maximum
Rh	rhodium
RMS	root-mean-square
RRE	radiative recombination efficiency
RSM	reciprocal space map
SEM	scanning electron microscopy
Si	silicon
SiH ₄	silane
SIMS	secondary ion mass spectroscopy
SP	sputtered
SP-HTA	sputtered and high temperature annealed
SPSL	short period superlattice
STEM	scanning transmission electron microscopy
TDD	treading dislocation density
TE	transverse–electric
TEM	transmission electron microscopy
TLM	transmission line method
TM	transverse–magnetic
TMAI	trimethylaluminium
TMGa	trimethylgallium
TU	Technische Univerität Berlin
UV	ultraviolet

UVC	ultraviolet-C
V/III	group V to group III partial pressure ratio
WPE	wall plug efficiency
XRD	X-ray diffraction

List of Samples

2 UVC-LEDs on low defect AlN/sapphire templates

Figure 2.7	TS4598-2V, TS4598-2H, TS4598-2Z
Figure 2.8	TS4598-2V, TS4598-2H, TS4598-2Z
Figure 2.9	TS4598-2V, TS4598-2H, TS4598-2Z
Figure 2.10	TS4634-2V, TS4634-2H, TS4634-2Z
Figure 2.12	TS5180-2V, TS5180-2H, TS5180-1H
Figure 2.13	TS5180-2V, TS5180-2H, TS5180-1H
Figure 2.14	TS5180-2V, TS5180-2H, TS5180-1H
Figure 2.15	TS5180-2V, TS5180-2H, TS5180-1H
Figure 2.16	TS5180-2V, TS5180-2H, TS5180-1H
Figure 2.17	TS5194-2V, TS5194-2H, TS5194-1H
Figure 2.18	TS5180-2V, TS5180-2H, TS5180-1H, TS5194-2V, TS5194-2H, TS5194-1H
Figure 2.19	TS5166-1, TS5166-3
Figure 2.20	TS5308-1, TS5316-3

3 Strain-induced defect generation in pseudomorphic AlGaIn:Si

Figure 3.2	TS4359, TS4373, TS4378, TS4379, TS4381 TS4389, TS4391
Figure 3.3	TS4359, TS4373, TS4378, TS4379, TS4381 TS4389, TS4391
Figure 3.4	TS4359, TS4373, TS4378, TS4379, TS4381 TS4389, TS4391
Figure 3.5	TS4442, TS4444, TS4447, TS4450, TS4456, TS4517
Figure 3.6	TS4442, TS4447
Figure 3.8	TS4679
Figure 3.9	TS4442, TS4444, TS4447, TS4450, TS4456, TS4517, TS4634, TS4638, TS4666, TS4679
Figure 3.10	TS4634, TS4704, TS5316

4 Determination of the polarization fields in the active region

Figure 4.5	MD9330, MD9331, MD9332
Figure 4.6	MD9328, MD9330, MD9331, MD9332
Figure 4.7	MD9328, MD9330, MD9331, MD9332
Figure 4.8	B6221, B6224, B6228, B6234, B6237

Figure 4.9	B6221, B6224, B6226, B6228, B6234, B6237
Figure 4.10	B6221, B6224, B6226, B6228, B6234, B6237
Figure 4.12	TS5180
Figure 4.13	TS4617, TS4619, TS4621, TS4629, TS4630, TS4648

5 Enhanced light extraction using a semi-transparent p-side

Figure 5.2	TS4817, TS5007, TS5167, TS5169, TS5171, TS5173, TS5174, TS5177, TS5183, TS5188
Figure 5.3	TS4817, TS5007, TS5167, TS5169, TS5171, TS5173, TS5174, TS5177, TS5183, TS5188
Figure 5.4	TS5007, TS5159, TS5169, TS5173, TS5174, TS5177, TS5183, TS5188
Figure 5.5	TS5007, TS5159, TS5169, TS5173, TS5174, TS5177, TS5183, TS5188
Figure 5.6	TS5169, TS5171, TS5173, TS5174, TS5183
Figure 5.7	TS5166, TS5188

Acknowledgments

First of all, I would like to thank Prof. Dr. Michael Kneissl for giving me the opportunity to work on this important topic in his group and for believing in me. I enjoyed giving several presentations at international conferences and project meetings.

I am grateful to the whole committee, Prof. Dr. Matthias Bickermann, Prof. Dr. Michael Kneissl, Prof. Dr. Udo W. Pohl and Dr. Hans-Juergen Lugauer.

I would also like to thank Dr. Tim Wernicke for his guidance, support and for his open-door policy to have a discussion at any time.

I am deeply grateful to all my Master's students Georgios G. Roumeliotis, Marcel Schilling, Daniel Hauer Vidal and Eviathar Ziffer as well as my Bachelor's students Marcel Schilling and Kay Töpfer for their contributions, numerous engaging discussions and their help in honing my scientific expertise.

It gives me great pleasure to acknowledge the support and help of my colleagues working in the epitaxy laboratory Matthias Dreier, Johannes Enslin, Dr. Humberto Foronda, Christian Kuhn, Dr. Frank Mehnke, Kathrin Schatke and Praphat Sonka.

This thesis would not be possible without the availability of excellent and novel templates from Dr. Sylvia Hagedorn, Sebastian Walde and Prof. Dr. Markus Weyers.

I am thankful to the entire process technology department at the TUB and FBH, namely Dr. Luca Sulmoni, Dr. Hyun K. Cho, Dr. Neysha Lobo-Ploch, Dr. Jens Rass and Dr. Sven Einfeldt.

For various simulations and measurements I want to thank Bettina Belde, Leonardo Cancellara, Dr. Johannes Glaab, Martin Guttmann, Dr. Anna Mogilatenko, Anton Muhin, Michael Narodovitch, Dr. Carsten Netzel, Christoph Reich, Jan Ruschel, Jonas Weinrich and Dr. Ute Zeimer.

I would also like to thank the entire group for the pleasant atmosphere, in particular my office colleagues Dr. Priti Gupta and Shaojun Wu.

Last but not least, I would like to extend my sincere thanks to my family. I am forever indebted to my mother Bettina Bellé-Susilo and my father Rolf Susilo for giving me the opportunity to follow my aspirations. I wish to express my deepest gratitude to my wife Anna Susilo, who was always there to support me and enrich my life every single day.